eXPRESS Polymer Letters Vol.5, No.1 (2011) 1
Available online at www.expresspolymlett.com
DOI: 10.3144/expresspolymlett.2011.1

Preface

T. Czigány[*]*, J. Karger-Kocsis*

Department of Polymer Engineering, Faculty of Mechanical Engineering, Budapest University of Technology and Economics, Műegyetem rkp. 3., H-1111, Budapest, Hungary

Dear Readers,

This is already the fifth volume of ***eXPRESS Polymer Letters***, which received its first impact factor, related to the year 2009, in June 2010. This impact factor of 1.452 is due to the consequent and high quality professional work done for the journal. As a result, today already 75% of the submitted papers are rejected. Our aim is, as before, a fast publication of original research works. A new service 'citation alert' was launched, wherein we inform the authors if their articles are cited in the freshly published issues of ***eXPRESS Polymer Letters***. As a further novelty, we record and display the 'most cited' and 'most downloaded' articles of the previous years on our website, thus helping our readers to monitor the actual trends and directions. The visit of K'2010 in Düsseldorf confirmed that for the plastics industry the crisis is over, the level of production reached, in certain segments exceeded the 2008 level, and the proportion of new materials and technologies presented was high. The third volume of ***eXPRESS Polymer Letters*** started when the crisis hit the plastics industry and the only possibility of recovery seemed to be the intensification of research and development. The vivid R&D work was reflected by the articles published in the last two years in our journal, and also in the novelties presented at the K'2010 exhibition. Major development goals and directions are: application of nanocomposites in products, widespread use of light construction materials (foams), development of heat resistant materials, optical use of polymers (improved transparency, exploitation of birefringence), application of biodegradable materials. In case of polymer processing saving of energy and material is still the main trend. This coupled with shorter production cycles and reduced downtimes due to product change, reduced cycle times, lower unit prices, integrated quality management, widespread use of special integrated technologies and automatization.

Based on the above trends and R&D results we have good reasons for hope and rejoicing. We are optimistic when looking forward to the future of ***eXPRESS Polymer Letters***. However, a further leap in the quality of eXPRESS Polymer Letters depends on the conscientious and hard work of our authors and referees, which is sincerely asked for also in the future.

In the name of International Advisory Board and the local Editorial Team, the editor and editor-in-chief wish you a lot of success in the coming year 2011. Sincerely yours,

Prof. Dr. T. Czigány
editor

Prof. Dr.-Ing. Dr.hc. J. Karger-Kocsis
editor-in-chief

[*]Corresponding author, e-mail: czigany@eik.bme.hu

eXPRESS Polymer Letters Vol.5, No.1 (2011) 2–11
Available online at www.expresspolymlett.com
DOI: 10.3144/expresspolymlett.2011.2

Hybrid thermosets from vinyl ester resin and acrylated epoxidized soybean oil (AESO)

S. Grishchuk[1], *J. Karger-Kocsis*[2,3*]

[1]Institut für Verbundwerkstoffe GmbH (Institute for Composite Materials), Kaiserslautern University of Technology, POBox 3049, D-67653 Kaiserslautern, Germany
[2]Department of Polymer Engineering, Faculty of Mechanical Engineering, Budapest University of Technology and Economics, H-1111 Budapest, Hungary
[3]Department of Polymer Technology, Faculty of Mechanical Engineering and Built Environment, Tshwane University of Technology, Pretoria, 0001, South Africa

Received 24 June 2010; accepted in revised form 1 September 2010

Abstract. A series of hybrids composed of styrene crosslinkable vinyl ester (VE) and acrylated epoxidized soybean oil (AESO) were produced via free radical-induced crosslinking. The VE/AESO ratio was changed between 75/25 and 25/75 wt%. Moreover, to support phase grafting the VE/AESO = 50/50 wt% hybrid was modified with phthalic anhydride in various amounts (1, 5 and 10 wt%). The structure of the hybrid systems was investigated by dynamic mechanical thermal analysis (DMTA), differential scanning calorimetry (DSC), and atomic force microscopy (AFM). The properties of the systems were assessed by static flexural and fracture mechanical tests. The resistance to thermal degradation was inspected by thermogravimetric analysis (TGA). The results suggested that the hybrids have an interpenetrating network (IPN) structure. With increasing AESO content the stiffness (modulus), strength and glass transition temperature (T_g) of the hybrids decreased, whereas their ductility increased. Phthalic anhydride caused an adverse trend. Both the fracture toughness and fracture energy increased with increasing AESO content. They were less affected by adding phthalic anhydride phase couplant. Interestingly, the hybrids outperformed the parent VE and AESO in respect to resistance to thermal degradation.

Keywords: *thermosetting resin, acrylated epoxidized soybean oil (AESO), fracture toughness, vinyl ester, interpenetrating network (IPN)*

1. Introduction

The synthesis of polymers from renewable resources is a preferred research topic nowadays. This is due to the eco-friendly classification of the related polymers which contribute to environment sustainability and to diminution of global warming by replacement of petroleum-based resins.

Plant oils, being unsaturated triglycerides, are very promising raw materials for the 'greening' of thermosets. This note especially holds for soybean oil which may be 'genetically engineered' for such polymer-related application. However, the double bonds along the fatty acid chain in the triglycerides, even if the unsaturation level in the compounds is high enough, are less reactive towards free radical-induced crosslinking than those in terminal positions. This is the reason why a large body of works addressed the 'functionalization' of plant (vegetable) oils to support the free radical-caused crosslinking and co-crosslinking (with other comonomers) reactions (e.g. [1, 2]). The related synthetic route starts usually with the epoxidation of the double bonds. Afterwards, these epoxy groups react with the carboxyl groups of selected acrylic acids. The resulting

*Corresponding author, e-mail: karger@pt.bme.hu

epoxidized and acrylated epoxidized vegetable oils can be cured alone and also used in epoxy formulations (e.g. [3–5]) and unsaturated polyester resins, as well (e.g. [6, 7]). It is worth noting that different strategies exist for both the functionalization and the co-curing of plant oils (e.g. [1, 2]). The role of the functionalized plant oils in the corresponding recipes may be different: reduction of styrene content and thus its emission (e.g. [6]), toughening agent (e.g. [8, 9]), plasticizer, etc. The use of oils from renewable resources offers also other benefits, such as low toxicity and inherent biodegradability. Beside of the use of functionalized plant oils as additives, several attempts were made to fully replace petroleum-based resins, especially unsaturated polyesters and epoxies in the related composites (e.g. [1, 2, 10–12]). Interestingly, less attention was paid to hybrid thermosets with interpenetrating network (IPN) structure. Under hybrid systems those composed of petroleum-based resins and functionalized plant oils are meant in this paper. By contrast, IPN-structured plant oils have been in focus of investigations since end of 1970s (e.g. [13]). It is noteworthy that IPN-structured thermosets can be produced also in one-pot synthesis. Major advantage of the resulting simultaneous IPNs is that their properties, including the glass transition temperature (T_g) can be set in-between those of the parent resins.

However, it is difficult to fully replace petroleum-based polymeric materials by those from renewable resources. The problems with biobased polymers are mainly due to their inferior mechanical and thermo-physical properties in comparison with conventional petroleum-based polymers that are intended to be replaced. Considering the fact that functionalized plant oils, when cured alone or even with styrene as reactive comonomer, yield rubber-like materials [1, 2, 14, 15], they have to be combined with such petroleum-based resins which show high stiffness, strength and T_g owing to their chemical build-up and tightly crosslinked structure. For that purpose vinyl ester resin (VE) is especially well suited as it contains stiff aromatic units. Accordingly, the aim of this study was to determine the structure-related mechanical and thermal performances of VE/acrylated epoxidized soybean oil (AESO) hybrids with possible IPN structure. To support the formation of the latter the VE/AESO ratio was varied between 25/75 and 75/25 wt%. A further aim was to check whether the creation of a more grafted IPN structure is accompanied with additional property improvements. Grafted IPN means that the intermingled phases (i.e. IPN) are chemically linked to each other via suitable chemical reactions [16]. For additional grafting phthalic anhydride has been selected that may react with both VE (hydroxyl groups) and AESO (epoxy and hydroxyl groups), and its effect was investigated in the system VE/AESO = 50/50 wt%. Phthalic anhydride already proved to be a promising curing agent for epoxidized plant oils (e.g. [17]). Further, its aromatic structure should promote the 'stiffening' of the phase structure of the hybrids on molecular level.

2. Experimental

2.1. Materials

The styrene diluted (~30 wt%) bisphenol-A type vinyl ester (VE; Daron-XP-45-A2 from DSM Composite Resins, Zwolle, The Netherlands) had the following characteristics: Hydroxyl value ~158 mg (KOH)/g, acid value < 4 mg (KOH)/g, viscosity 175–225 mPa·s at 23°C, and density 1.08 g/ml at 23°C. Acrylated epoxidized soybean oil (AESO), containing ca. 3500 ppm (by liquid chromatography) monomethyl ether hydroquinone as inhibitor, was purchased from Sigma-Aldrich Chemie GmbH (Taufkirchen, Germany). The characteristics of AESO are: viscosity 29.1 Pa·s at 25°C, acid value 8.08 mg (KOH)/g, epoxy value = 8.50 mg (KOH)/g, density 1.04 g/ml at 25°C. Phthalic anhydride (melting point = 129–133°C; grade: purum, containing ~2% phthalic acid) was also purchased from Sigma-Aldrich Chemie GmbH. Anti-foaming agent BYK-A 555 was received from BYK Chemie GmbH (Wesel, Germany). Dibenzoyl peroxide (BPO; Perkadox CH50L – peroxide content 50 wt%) and N,N-diethyl aniline (DEA) accelerator were purchased from Akzo Nobel (Düren, Germany).

The following VE/AESO combinations were made: 75/25, 50/50 and 25/75 wt%. For reference purpose VE and AESO were produced separately. Curing of the resins occurred by adding BPO and DEA in 1.5 and 0.15 wt%, respectively. 1, 5 and 10 wt% of phthalic anhydride (A) was used for additional crosslinking for the VE/AESO = 50/50 wt% sys-

tem. To avoid foaming all formulations contained 0.4 wt% BYK-A 555.

2.2. Specimens preparation

The resins were prepared as given below. VE and AESO were mixed together at room temperature (RT) for 4 min with a cogged-wheel mixer at 800 revolutions per minute [rpm]. Then, in the same procedure 1.5 wt% of BPO was dissolved and the obtained mixtures were degassed *in vacuo*. Afterwards 0.15 wt% of accelerator was introduced. The resin formulations were mixed for additional 3 min by 800 rpm, degassed again and poured in open moulds fabricated from polytetrafluoro ethylene. Plates (100×10×4 mm^3, length × width × thickness) and compact tension (CT) specimens (35×35×4 mm^3, length × width × thickness) were produced in the cavities of the moulds. For crosslinking of the resin systems the following regime was set: RT for 1 hour [h], 50°C for 15 min, 80°C for 30 min, 140°C for 30 min, and finally 180°C for 1 h. The moulds were then cooled to ambient temperature over night and the specimens removed.

2.3. Materials characterization

The phase structure of the cured samples was studied by dynamic-mechanical thermal analysis (DMTA) and differential scanning calorimetry (DSC), respectively. DMTA traces (storage modulus, E'; and the mechanical loss factor, tanδ *vs*. temperature) were determined by a DMA Q800 device of TA Instruments (New Castle, DE, USA) on rectangular specimens (60×10×3 mm^3; length × width × thickness) in 3-point bending configuration (span length: 50 mm) at 1 Hz with an oscillation amplitude of 50 μm. The scan rate in the selected temperature range (T = –100…+250°C) was 1°C/min.

DSC traces were recorded by a DSC821 device of Mettler Toledo (Gießen, Germany) at 10°C/min heating rate in the temperature range of –100 to +250°C. The aluminum pans used were filled with ca. 10 mg resin sample. For the T_g determination of the resins the mid point of the glass transition step was considered.

Further information on the morphology was from atomic force microscopic (AFM) studies. They were carried out on polished samples of the VE/AESO = 50/50 wt% system. The surface profile was scanned by AFM (Veeco/Digital Instruments GmbH, Mannheim, Germany) in tapping mode, and the related height- and phase-contrast images captured. Commercial silicon cantilever (Pointprobe®NCH) with a nominal tip radius of less than 10 nm (120 μm cantilever length, 4 μm thickness, 30 μm width and spring constant at 42 Nm^{-1} (Nanosensors, Neuchatel, Switzerland)) was employed under its fundamental resonance frequency of about 330 kHz. The scan rates were set at 0.5 Hz for all images.

The flexural properties, namely, modulus, strength and strain of the hybrid resins, were determined on rectangular specimens (60×10×3×mm^3; length × width × thickness; 5 specimens for each composition) in three point bending at RT on a Zwick 1474 machine (Zwick GmbH, Ulm, Germany) according to EN63. The span length of the specimens was 50 mm and their loading occurred with deformation rate of v = 1 mm/min.

Fracture energy (G_c) and fracture toughness (K_c) were determined on CT specimens (min. 5 specimens for each composition) according to ISO 13586-1 standard. The CT specimens were initially notched by sawing. Their notch root was sharpened by a fresh razor blade prior to their tensile loading (mode I) at room temperature on a Zwick 1445 machine (Zwick GmbH, Ulm, Germany) with a crosshead speed of v = 1 mm/min. Surfaces of the broken CT specimens were inspected in a scanning electron microscope (SEM, JSM-5400 of Jeol, Tokyo, Japan). To avoid electric charging the fracture surface was sputter coated with an Au/Pd alloy.

The resins were subjected to thermogravimetric analysis (TGA) in a DTG-60 device of Shimadzu Deutschland GmbH (Duisburg, Germany). The TGA experiments were conducted under nitrogen atmosphere in the temperature range T = +25°C…+600°C with heating rate 20°C/min.

3. Results and discussion

3.1. Phase structure

Figure 1 depicts the storage modulus (E') and mechanical loss factor (tanδ) as a function of temperature (T) for the VE and for the VE/AESO hybrids. The glass transition temperatures (T_g) and maximal values of tanδ are presented in Table 1 for the systems studied. Unfortunately, the DMTA curve of reference AESO could not be captured in three-point bending mode due to premature failure.

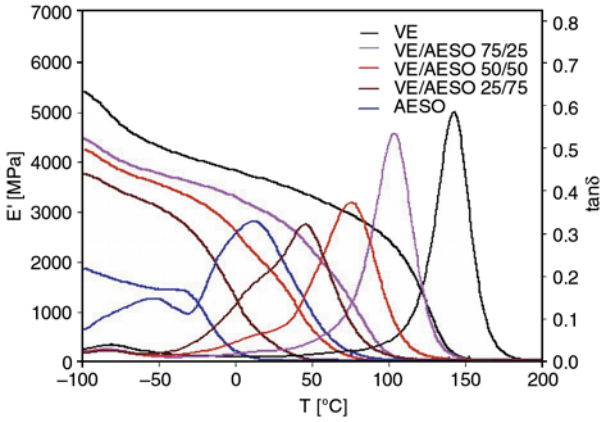

Figure 1. *E′* and tand as a function of *T* for crosslinked VE, AESO and VE/AESO hybrids of different compositions

Therefore the crosslinked AESO was characterized by DMTA in tension mode. Two broad T_g relaxations, viz. at $T \sim -50$°C and $T \approx 15$°C, respectively, were detected for the polymerized AESO. It is due to the multi-functionality and high unsaturation level of the AESO: network sections of different crosslink densities (including hyperbranched structures as demonstrated later) are formed owing to homo- and copolymerization reactions of the double bonds of different acrylated triglycerides, present in the soybean oil. Additionally, homopolymerization of the residual epoxy groups of AESO and their reaction with the secondary hydroxyl groups of AESO at elevated temperatures might have also influenced the crosslinking. The parent VE shows two relaxations: the α-peak or T_g is at $T \approx 140$°C, while the β-one is at $T \approx -80$°C. All VE/AESO hybrids display the β-relaxation in the same temperature region as VE. However, the change in the shape of the α-peaks of the VE/AESO hybrids suggests that the morphology becomes more complex with the AESO content (see also the onset of a shoulder at the lower temperature flank of the T_g peak). It is clearly seen that with increasing AESO content the stiffness (E') in the glassy state is monotonously decreasing. This is accompanied by a similar change in the T_g (read as the peak temperature of the α-transition in this case). Moreover, the T_g peak becomes less intensive and more broad with increasing AESO content of the hybrids. On the other hand, no peak doubling can be observed indicating the good compatibility between AESO and VE. The appearance of a shoulder (α'-relaxation) in the tanδ *vs*. *T* trace of the hybrids with 50 wt% AESO and more, can be attributed AESO-related homo- and copolymerization reactions. This is supported by the fact that the position of the shoulder agrees well with that of the α-relaxation of the polymerized AESO – cf. Figure 1. The slight shift towards higher temperatures in the position of the shoulder of the AESO-rich VE/AESO hybrids compared to the crosslinked AESO hints for grafting, which manifests itself in the reduced segmental mobility. Moreover, peak broadening is a usual feature in graft-IPN structured thermosets. On the other hand, the great amount of possible relaxations modes acting in triglyceride-based polymers results *per se* in a broad T_g peak [14]. Based on the above results one can conclude that AESO works as a reactive plasticizer in VE. Note that a reduction in T_g is usually due to less tight crosslinking (co-network) which covers also the formation of IPN. According to the opinion of the authors the intensity reduction of the T_g peak can be ascribed to some constraint effects on supramolecular level which supports the presence of IPN. It is noteworthy that two T_g steps were resolved in DSC (cf. Table 1 and Figure 3a) the possible reason of which was disclosed above.

Table 1. Glass transition temperatures (T_g) of the VE and VE/EASO hybrids
Designation: (P)AESO – crosslinked AESO

Material	Properties				
	DSC	DMA			
	T_g [°C]	$T_g(\alpha)$ [°C]	$T_g(\alpha')$ [°C]	max tanδ at $T_g(\alpha)$	max tanδ at $T_g(\alpha')$
VE	114	143	–	0.59	–
VE/AESO 75/25	93	105	~20	0.53	0.03
VE/AESO 50/50	45	78	~15	0.37	0.07
VE/AESO 50/50 A1%	46	78	~15	0.38	0.06
VE/AESO 50/50 A5%	47	79	~15	0.39	0.05
VE/AESO 50/50 A10%	48	79	~15	0.41	0.05
VE/AESO 25/75	26	48	~15	0.32	0.19
(P)AESO	–26 (–4)	14	–52	0.33	0.15

Note: α' corresponds to the shoulder on tanδ *vs*. *T* trace

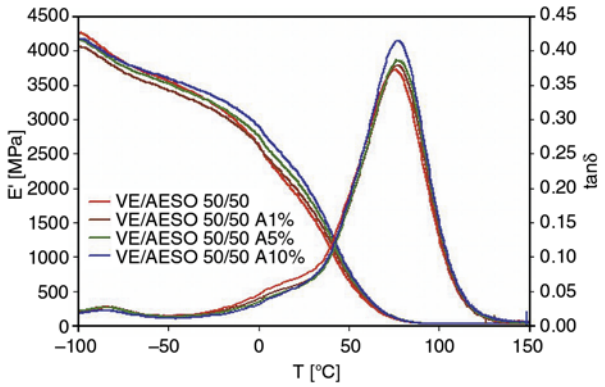

Figure 2. E' and tanδ as a function of T for VE/AESO = 50/50 wt% hybrid with and without phthalic anhydride (A) in different amounts

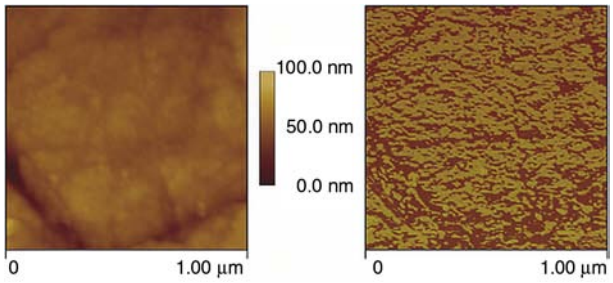

Figure 4. Height (left) and phase contrast (right) AFM images taken from the polished surface of VE/AESO = 50/50 wt% hybrid

Additional incorporation of phthalic anhydride (A) improved the glassy storage modulus of the corresponding hybrid via the supposed grafting (cf. Figure 2). With increasing A content the E' values were monotonously, but only marginally enhanced above RT. Similarly, no change could be resolved in the tanδ *vs*. T traces as a function of added A. This finding is in contrast to the expectation and requires further investigations.

The DSC results are in harmony with the DMTA ones: the T_g step is shifted to lower temperatures with increasing AESO content of the hybrids (cf. Figure 3a), and modification with A did not change much the position of T_g of the VE/AESO = 50/50 wt% (cf. Figure 3b). The difference in the T_g values based on DSC and DMTA can be explained by the different measuring principles and heating rates selected. The fact that the crosslinked AESO shows two T_g steps already suggests how complex its structure is. This is linked with the peroxy-induced various crosslinking reactions in AESO.

A deeper insight in the morphology was expected from AFM investigations. The related height and phase AFM images are shown in Figure 4. By contrast to VE, which exhibits a clear nodular structure (nodules is in the range of 50–70 nm [18]), the structure of VE/AESO = 50/50 wt% hybrid is likely an IPN. This is substantiated by the AFM phase image in Figure 4, in which the AESO-rich phase is dark (being 'soft'), whereas the VE-rich one is white (being 'hard'). Note that both phases are likely intermingled, continuous. In order to deliver direct evidence for the formation of IPN, transmission electron microscopic (TEM) inspection should be carried out on suitably stained samples. Nonetheless, the IPN structuring with nanoscale-entities (cf. Figure 4) should be favored by the styrene acting as reactive comonomer for the crosslinking of both VE and AESO.

3.2. Flexural mechanical properties

The static flexural properties (modulus (E_f), strength (σ_f) and strain (ε_f) – the two latter taken at the maximum load) of the systems studied are listed in Table 2. As expected according to the DMTA

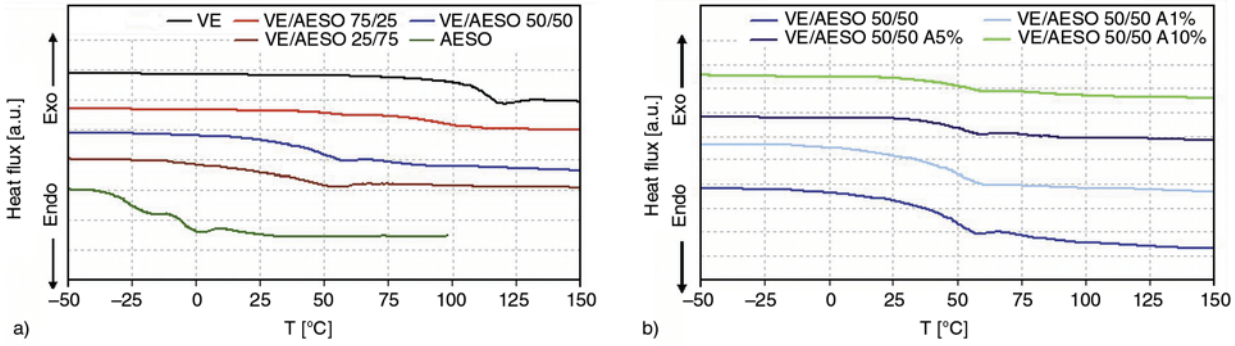

Figure 3. a) DSC traces showing the T_g steps for VE and VE/AESO hybrids of different compositions, b) DSC traces showing the T_g steps for VE/AESO = 50/50 wt% hybrid with and without phthalic anhydride (A) in different amounts

Table 2. Flexural (modulus, E_f, strength, σ_f, and strain, ε_f, at maximal load) and fracture mechanical (K_c and G_c) properties of VE and VE/AESO hybrids

Material	Properties				
	Flexure			Fracture mechanics	
	E_f [MPa]	σ_f [MPa]	ε_f [%]	K_c [MPa·m$^{1/2}$]	G_c [kJ·m^2]
VE	3212±137	123±24	4.3±0.8	0.55±0.05	0.20±0.01
VE/AESO 75/25	2778±140	112±8	5.1±1.0	0.59±0.04	0.22±0.02
VE/AESO 50/50	1516±120	61±3	5.9±0.7	0.70±0.03	0.37±0.04
VE/AESO 50/50 A1%	1654±148	65±3	5.8±0.4	0.63±0.05	0.33±0.05
VE/AESO 50/50 A5%	1683±119	66±8	5.6±0.3	0.73±0.06	0.39±0.05
VE/AESO 50/50 A10%	1803±144	72±8	5.5±0.3	0.55±0.03	0.28±0.04
VE/AESO 25/75	234±33	15±2	16.3±1.5	0.36±0.01*	0.68±0.03*

*Designation: computed by considering the load maximum as the prerequisites of the linear elastic fracture mechanics did not hold anymore

results, E_f decreased with increasing AESO content. A similar tendency was detected for the flexural strength. On the other hand, the flexural strain slightly increased with increasing AESO content until its content reached 50 wt%. By contrast, the VE/AESO = 25/75 wt% hybrid exhibited very high ductility, reflected by the related high ε_f value (cf. Table 1). Incorporation of A in more and more amount yielded the opposite tendency. This suggests that the proposed grafting between VE and AESO took place, in fact.

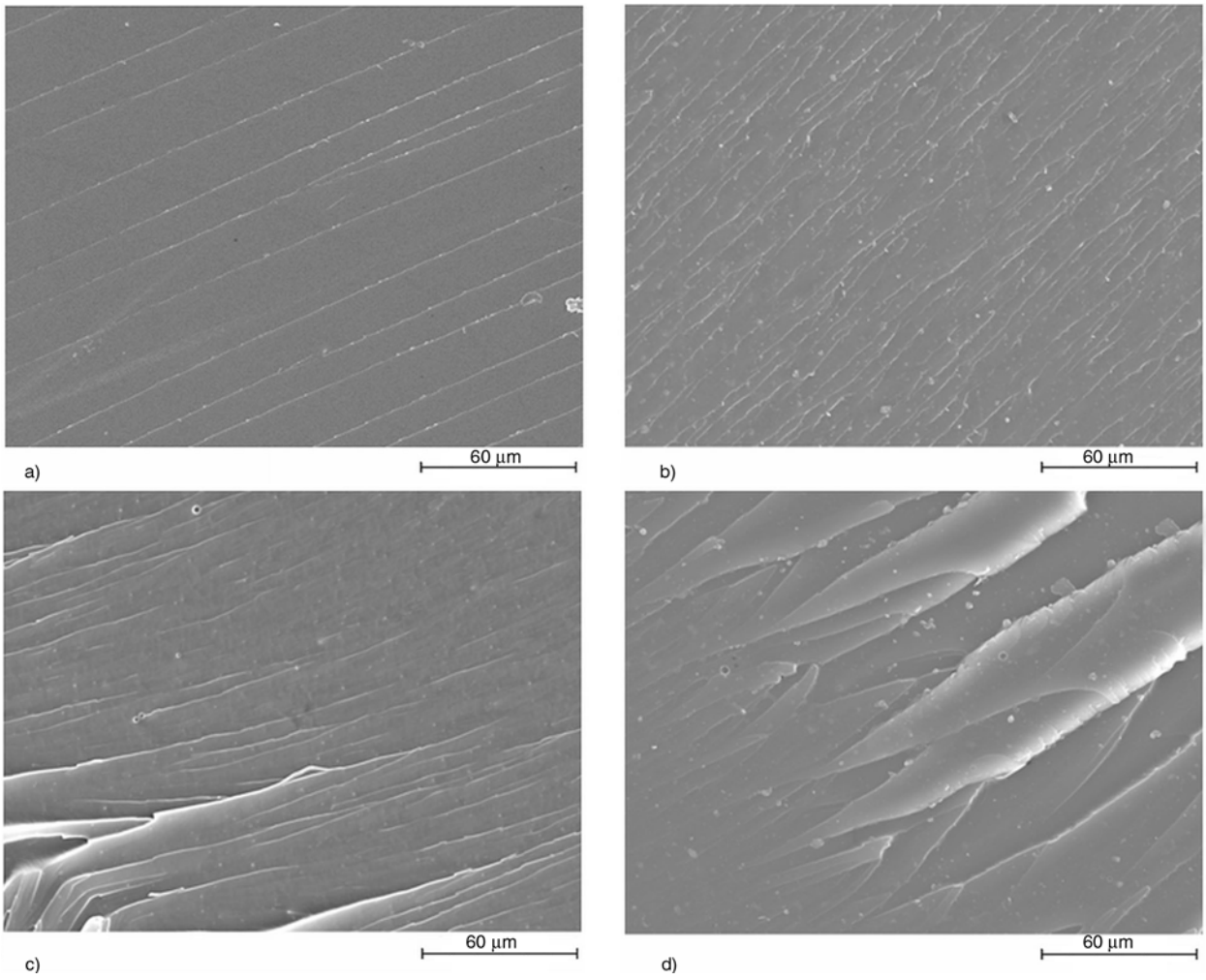

Figure 5. SEM pictures taken from the fracture surfaces of VE (a), VE/AESO = 75/25 wt% (b), VE/AESO = 50/50 wt% (c), and VE/AESO = 25/75 wt% (d)

3.3. Fracture mechanical properties and failure mode

The fracture toughness and energy data (K_c and G_c, respectively) for the systems studied are also summarized in Table 2. Note that both the K_c and G_c parameters increased with increasing AESO content. This tendency is seldom because increasing K_c is usually accompanied with decreasing G_c if the modulus (and Poisson ratio) of the related systems does not change much. However, the modulus of the hybrids changed markedly (cf. Table 2) which is the major reason for the enhanced G_c. The simplest explanation for increasing K_c is that with increasing AESO content the related hybrids, due to their peculiar phase structure, become less notch-sensitive.

Figure 5 displays characteristic SEM pictures taken from the fracture surface of VE and VE/AESO hybrids. One can see that the fracture surface becomes rougher with increasing AESO content of the hybrids. This is a clear indication for the enhancement of the fracture energy. The shear-steps, termed 'river like' pattern, in the fracture surfaces of the hybrids suggest that they failed by shear deformation. It is noteworthy that the shear deformation is strongly supported by the IPN structure as argued by Karger-Kocsis [16].

Inspection of the fracture surfaces of the hybrids yielded some further insight in their morphology. Especially in case of the hybrids VE/AESO = 75/25 and 25/75 wt% dendritic inclusions could be found – cf. Figure 6. The reason for the appearance of such inclusions is unknown by the authors. Similar dendritic formations were reported for VE-based systems toughened by polymerizable hyperbranched and star-shaped polymers [19], and for IPNs composed of polymethyl methacrylate and polyurethane that contained unsaturated plant oils [20]. In the former case the authors [19] claimed that the dendritic inclusions were formed mostly by

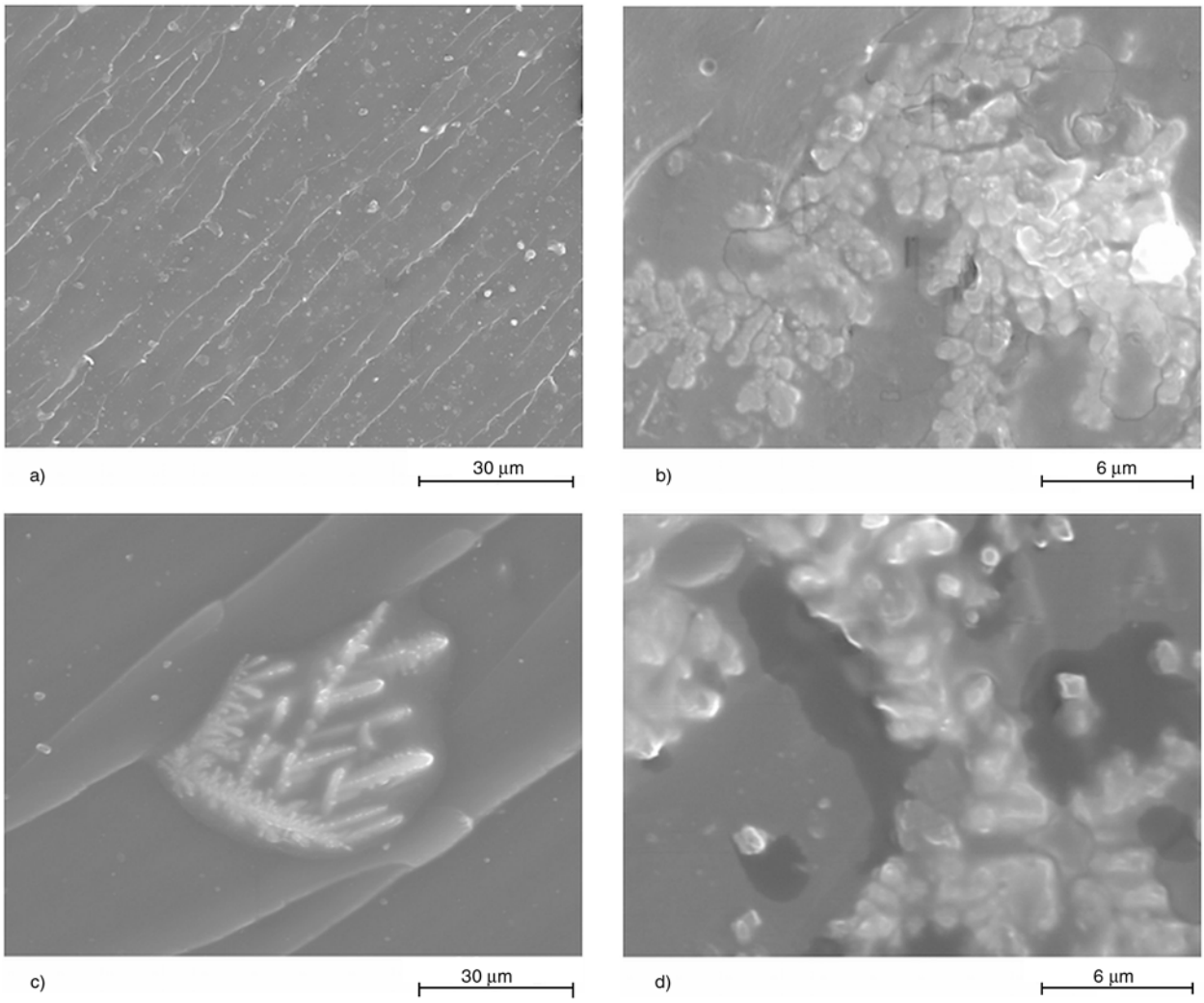

Figure 6. SEM pictures taken from the fracture surfaces of VE/AESO = 75/25 wt% (a, b), and VE/AESO = 25/75 wt% (c, d)

homopolymerization of the toughening additive. We think that in the VE/AESO hybrids the onset of these dendritic inclusions is due to AESO homo- and AESO/styrene copolymerization reactions.

This is the right place to give some further notes on the IPN-structure proposed. As it was mentioned in manuscript, the coexistence of two continuous phases was detected on nano-level by AFM. Additionally, the two-phase structure of VE/AESO systems was confirmed by DMTA (α- and α'-relaxations, respectively). Finally, hyperbranched structures were detected by SEM in the case of hybrids with 'unbalanced' compositions (i.e. VE/AESO 25/75 and 75/25 wt%). In our opinion, the difference in the reactivity of components, bearing different functional groups and functionality (this was discussed for AESO and styrene in Ref. [21], recently), is the main reason for the formation of the hybrid networks having IPN-like structure.

Moreover, the influence of steric hindrances on the (co)polymerization of the components (AESO-styrene, VE-styrene, AESO-VE) caused by the long alkyl chains of AESO is markedly stronger in comparison to the aromatic structured VE. This results in the simultaneous formation of separate VE-styrene and AESO-styrene networks having relatively low inter-grafting degree. Note that gelation of the systems already occurred at ambient temperature. The high functionality and unsaturation level of AESO triggered the formation of hyperbranched structures on micron-scale. This indicates the high homopolymerization ability of AESO, yielding a multiphase structure. The latter was confirmed by DMTA and DSC results. By contrast, VE molecules having only two acrylic and two secondary hydroxyl groups are not able to form such dendritic structures. The fact that hyperbranched structures were only detected in the VE/AESO 25/75 and 75/25 wt% systems can be ascribed to the effect of the major component of the composition. The major component will be crosslinked, whereas the minor one pre-gelated, and its further crosslinking occurs in presence of the crosslinked network of the major component. In case of the 'balanced' composition (VE/AESO 50/50 wt%) the gelation and crosslinking of both components (no concentration influ-

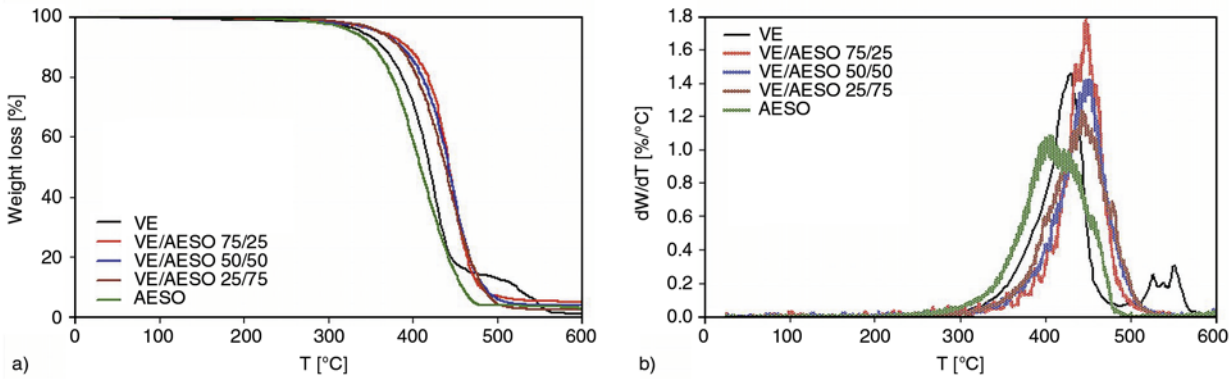

Figure 7. a) TGA traces for VE and VE/AESO hybrids of different compositions, b) Derivative TGA traces for VE and VE/AESO hybrids of different compositions

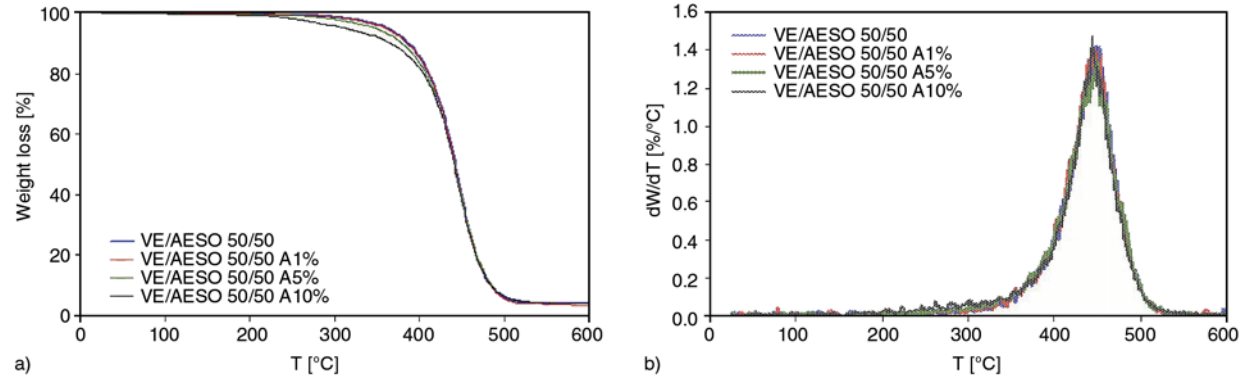

Figure 8. a) TGA traces for VE/AESO = 50/50 wt% hybrid with and without phthalic anhydride (A) in different amounts, b) Derivative TGA traces for VE/AESO = 50/50 wt% hybrid with and without phthalic anhydride (A) in different amounts

ence) occurred parallel excluding the appearance of dendritic structures.

3.4. Thermogravimetric analysis (TGA)

The TGA yielded some unexpected results. The TGA curves in Figure 7 show that the resistance to thermal degradation of the hybrids is higher than that of either VE or AESO. The most straightforward explanation for such synergistic effect is that the confined molecular structure within the IPN hampers the decomposition and the subsequent diffusion/volatilization of the decomposition products. If this explanation holds, then incorporation of phthalic anhydride should give even better results as the onset of grafted IPN is accompanied with even higher molecular 'confinement'. This was, however, not the case as one can observe in Figure 8. Increasing amount of A did not result in a further shift in the TGA traces towards higher temperature. The observed effect may also be linked with the A itself because it might have been in surplus (i.e. without coupling the phases) in the recipe or working as initiation site during thermal decomposition.

4. Conclusions

Based on this work devoted to study the structure, (fracture) mechanical and thermal behaviors of hybrid resins, composed of styrene crosslinkable vinyl ester (VE) and acrylated epoxidized soybean oil (AESO), crosslinked in the presence and absence of phthalic anhydride as phase coupling agent and additional crosslinker, the following conclusions can be drawn:

- The structure of the hybrids VE/AESO = 75/25…25/75 wt% is likely IPN type. This was deduced from results achieved by different techniques giving direct (AFM) and indirect hints (DMTA, SEM, TGA), respectively. Nevertheless, the presence of IPN structure should be confirmed, possibly by TEM.
- With increasing AESO amount, beside of T_g, also the flexural modulus and strength of the hybrids were reduced, whereas their ductility (flexural strain) enhanced. Additional use of phthalic anhydride in the recipe yielded mostly an adverse trend in the above-mentioned properties. Both K_c and G_c were improved by increasing AESO hybridization. Incorporation of phthalic anhydride did not cause a pronounced change in the above fracture mechanical parameters.
- The hybrids showed improved resistance to thermal decomposition compared to the parent VE and AESO. This was attributed to the presence of IPN structure owing to the related confined molecular structure hindering the decomposition and follow-up processes.

We can sum up that hybridization of AESO with VE is a promising strategy to develop hybrid resins with tailored thermal and mechanical properties, which are suited for engineering applications.

Acknowledgements

This work was performed in the framework of a bilateral cooperation program between Germany (DAAD) and Hungary (MöB). It is also connected to the scientific program of the 'Development of quality-oriented and harmonized R+D+I strategy and functional model at BME', supported by the New Hungary Development Plan (Project ID: TÁMOP-4.2.1/B-09/1/KMR-2010-0002).

References

[1] Khot S. N., Lascala J. J., Can E., Morye S. S., Williams G. I., Palmese G. R., Kusefoglu S. H., Wool R. P.: Development and application of triglyceride-based polymers and composites. Journal of Applied Polymer Science, **82**, 703-723 (2001). DOI: 10.1002/app.1897

[2] Raquez J-M., Deléglise M., Lacrampe M-F., Krawczak P.: Thermosetting (bio)materials derived from renewable resources: A critical review. Progress in Polymer Science, **35**, 487–509 (2010). DOI: 10.1016/j.progpolymsci.2010.01.001

[3] Zhu J., Chanrashekhara K., Flanigan V., Kapila S.: Curing and mechanical characterization of a soy-based epoxy resin system. Journal of Applied Polymer Science, **91**, 3513–3518 (2004). DOI: 10.1002/app.13571

[4] Miyagawa H., Jurek R. J., Mohanty A. K., Misra M., Drzal L. T.: Biobased epoxy/clay nanocomposites as a new matrix for CFRP. Composites Part A: Applied Science and Manufacturing, **37**, 54–62 (2006). DOI: 10.1016/j.compositesa.2005.05.014

[5] Miyagawa H., Misra M., Drzal L. T., Mohanty A. K.: Fracture toughness and impact strength of anhydride-cured biobased epoxy. Polymer Engineering and Science, **45**, 487–495 (2005). DOI: 10.1002/pen.20290

[6] Boyd S. E., La Scala J. J., Palmese G. R.: Molecular relaxation behavior of fatty acid-based vinyl ester resin. Journal of Applied Polymer Science, **108**, 3495–3506 (2008).
DOI: 10.1002/app.27957

[7] Haq M., Burgueño R., Mohanty A. K., Misra M.: Bio-based unsaturated polyester/layered silicate nanocomposites: Characterization and thermo-physical properties. Composites Part A: Applied Science and Manufacturing, **40**, 540–547 (2009).
DOI: 10.1016/j.compositesa.2009.02.008

[8] Raghavachar R., Letasi R. J., Kola P. V., Chen Z., Massingill J. L.: Rubber-toughening epoxy thermosets with epoxidized crambe oil. Journal of the American Oil Chemists' Society, **76**, 511–516 (1999).
DOI: 10.1007/s11746-999-0033-3

[9] Lu J., Wool R. P.: Additive toughening effects on new bio-based thermosetting resins from plant oils. Composites Science and Technology, **68**, 1025–1033 (2008).
DOI: 10.1016/j.compscitech.2007.07.009

[10] Meier M. A. R., Metzger J. O., Schubert U. S.: Plant oil renewable resources as green alternatives in polymer science. Chemical Society Reviews, **36**, 1788–1802 (2007).
DOI: 10.1039/b703294c

[11] Lu J., Khot S., Wool R. P.: New sheet molding compound resins from soybean oil. I. Synthesis and characterization. Polymer, **46**, 71–80 (2005).
DOI: 10.1016/j.polymer.2004.10.060

[12] Lu J., Wool R. P.: Novel thermosetting resins for SMC applications from linseed oil: Synthesis, characterization, and properties. Journal of Applied Polymer Science, **99**, 2481–2488 (2006).
DOI: 10.1002/app.22843

[13] Barrett L. W., Sperling R. H., Murphy C. J.: Naturally functionalized triglyceride oils in interpenetrating polymer networks. Journal of the American Oil Chemists' Society, **70**, 523–534 (1993).
DOI: 10.1007/BF02542588

[14] La Scala J., Wool R. P.: Property analysis of triglyceride-based thermosets. Polymer, **46**, 61–69 (2005).
DOI: 10.1016/j.polymer.2004.11.002

[15] Fu L., Yang L., Dai C., Zhao C., Ma L.: Thermal and mechanical properties of acrylated expoxidized-soybean oil-based thermosets. Journal of Applied Polymer Science, **117**, 2220–2225 (2010).
DOI: 10.1002/app.32126

[16] Karger-Kocsis J.: Simultaneous interpenetrating network structured vinylester/epoxy hybrids and their use in composites. in 'Micro- and nanostructured multiphase polymer blend systems: Phase morphology and interfaces' (eds.: Harrats C., Thomas S., Groeninckx G.) CRC Press, Boca Raton, 273–293 (2006).

[17] Dos Santos Martini D., Aguiar Braga B., Samios D.: On the curing of linseed oil epoxidized methyl esters with different cyclic dicarboxylic anhydrides. Polymer, **50**, 2919–2925 (2009).
DOI: 10.1016/j.polymer.2009.03.058

[18] Karger-Kocsis J., Gryshchuk O., Schmitt S.: Vinylester/epoxy-based thermosets of interpenetrating network structure: An atomic force microscopic study. Journal of Materials Sciences, **38**, 413–420 (2003).
DOI: 10.1023/A:1021855228253

[19] Karger-Kocsis J., Fröhlich J., Gryshchuk O., Kautz H., Frey H., Mülhaupt R.: Synthesis of reactive hyperbranched and star-like polyethers and their use for toughening of vinylester-urethane hybrid resins. Polymer, **45**, 1185–1195 (2004).
DOI: 10.1016/j.polymer.2003.12.050

[20] Kong X., Narine S. S.: Sequential interpenetrating polymer networks produced from vegetable oil based polyurethane and poly(methyl methacrylate). Biomacromolecules, **9**, 2221–2229 (2008).
DOI: 10.1021/bm800335x

[21] Şen S., Çayli G.: Synthesis of bio-based polymeric nanocomposites from acrylated epoxidized soybean oil and montmorillonite clay in the presence of a bio-based intercalant. Polymer International, **59**, 1122–1129 (2010).
DOI: 10.1002/pi.2838

eXPRESS Polymer Letters Vol.5, No.1 (2011) 12–22
Available online at www.expresspolymlett.com
DOI: 10.3144/expresspolymlett.2011.3

Biodegradable conductive composites of poly(3-hydroxybutyrate) and polyaniline nanofibers: Preparation, characterization and radiolytic effects

P. L. B. Araujo[1,2], C. R. P. C. Ferreira[2], E. S. Araujo[2]*

[1]Laboratório de Química de Produtos Naturais Bioativos, Departamento de Química, Universidade Federal Rural de Pernambuco, Av. D. Manoel de Medeiros, s/n., 52171-900, Dois Irmãos, Recife, Brazil
[2]Laboratório de Polímeros e Nanoestruturas, Departamento de Energia Nuclear, Universidade Federal de Pernambuco, Av Prof. Luis Freire, n. 1000, 50740-540, Cidade Universitária, Recife, Brazil

Received 19 August 2010; accepted in revised form 3 September 2010

Abstract. Poly(3-hydroxybutyrate) is a biodegradable polyester produced by microorganisms under nutrient limitation conditions. We obtained a biodegradable poly(3-hydroxybutyrate) composite having 8 to 55% of chemically *in situ* polymerized hydrochloric acid-doped polyaniline nanofibers (70–100 nm in diameter). Fourier transform infrared spectroscopy and X-rays diffractometry data did not show evidence of significant interaction between the two components of the nanocomposite, and polyaniline semiconductivity was preserved in all studied compositions. Gamma-irradiation at 25 kGy absorbed dose on the semiconductive composite presenting 28% of doped polyaniline increased its conductivity from $4.6 \cdot 10^{-2}$ to 1.1 S/m, while slightly decreasing its biodegradability. PANI-HCl biodegradation is negligible when compared to PHB biodegradability in an 80 day timeframe. Thus, this unprecedented all-polymer nanocomposite presents, at the same time, semiconductivity and biodegradability and was proven to maintain these properties after gamma irradiation. This new material has many potential applications in biological science, engineering, and medicine.

Keywords: *nanocomposites, gamma-irradiation, biodegradable polymers, polyaniline, poly(hydroxybutyrate)*

1. Introduction

Biodegradable polymers are defined as macromolecules in which the primary degradation mechanism is through the action and metabolism of microorganisms [1]. In general, biodegradable polymer materials are degraded into biomass, carbon dioxide, and/or methane. Thus, the macromolecular backbone suffers breakdown and is used as a source of carbon and energy.

A major forefront for the application of biodegradable polymers is in medical science and technology. They are used as temporary substitutes for natural tissues and degrade *in vivo* over a predetermined period of time generating safe end products. Among these materials, polyhydroxyalkanoates (PHAs) [2] along with poly(α-hydroxy acids) [3] are the most used biodegradable polymers.

PHAs are polyesters produced by microorganisms under nutrient limitation conditions [4]. Poly(3-hydroxybutyrate) (PHB) and copolymers of 3-hydroxybutyrate and 3-hydroxyvalerate (PHB-*co*-HV) can be considered as the most known PHAs. They present biodegradability and good biocompatibility and are frequently used, as neat substances or composites, for fabrication of medical supplies, including: sutures, screws, bone plates, orthopedic pins, guided tissue repair/regeneration devices, nerve guides, vein valves, bone marrow scaffolds,

*Corresponding author: elmo@pq.cnpq.br

ocular cell implants, substitutes for skin and dura tissue, wound dressing, and hemostats [2]. PHB-*co*-HV can also be used as biodegradable drug carriers in implants loaded with therapeutic substances such as antibiotics [5] or anticancer drugs [6]. Among all PHAs, PHB appears to have a broader range of applications due to its good combination of mechanical, biological, and surface properties [7].

The previously-cited PHB characteristics turn this polymer into a very interesting matrix for the fabrication of multifunctional materials, namely polymer nanocomposites. In spite of their innumerous potential applications, scientific information on nanocomposites based on PHB and other PHAs are rather limited. Reports on the fabrication of PHB [8] or PHB-*co*-HV [8, 9] composites through melting intercalation showed that improved thermal tensile properties could be achieved in composites presenting nanodispersions of organoclay on PHB-*co*-HV matrix, although, thermal degradation of PHB after melting process might have counterbalanced the improving effect of this filler on the nanocomposite [9]. Nanocomposites of PHB-*co*-HV/multiwalled carbon nanotubes are reported to exhibit higher thermal stability than PHB-*co*-HV itself [10].

In the present work, we report the development of a simple, straightforward method to fabricate PHB/polyaniline (PANI) nanocomposites. PANI is an intrinsically conductive polymer (ICP) which has been extensively studied over the last twenty years, in both theoretical [11, 12] and practical points-of-view [13, 14]. This polymer combines striking properties such as metal-like characteristics [15], reversible doping level [16], and good biocompatibility [17]. PANI presents four oxidation states, which can arranged in crescent order of oxidation level as leucoemeraldine, emeraldine, nigraniline and pernigraniline. Each one of these substances presents a base and a salt form [18]. The electrically conductive form of PANI is the emeraldine salt, shown in Figure 1. Such versatile polymer attracts researchers from a number of areas, leading to frequent reports on PANI practical uses. In recent years, our research group reported a new application of PANI as a radiostabilizing agent in nanocomposites of poly(methyl methacrylate) (PMMA) and PANI nanofibers submitted to radiosterilization [19, 20].

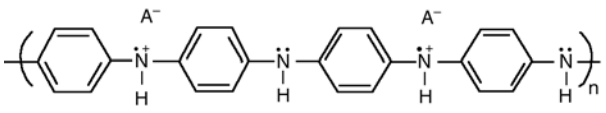

Figure 1. Polyaniline emeraldine salt, an electrically conducting form of polyaniline. A^- is a counter-ion.

The composites presented in this work have, at the same time, biodegradability and semiconductivity and are made of *in situ* chemically polymerized HCl-doped polyaniline (PANI) nanofibers as fillers and the bacterially-produced Brazilian commercial PHB as the matrix.

Our methodology of choice for the preparation of nanofibers embedded into PHB matrix is based on the rapid mixing of the oxidant agent with an initial short period of stirring, an approach firstly presented by Huang and Kaner, in 2006 [21], to produce bulky quantities of PANI nanofibers in water and other solvents. Following the addition of the agent, fast consumption of the oxidant occurs, and polymer chain overgrowth is prevented. In such conditions, PANI nanofibers are allowed to form, as nanostructures of this particular morphology appear to be intrinsic to PANI and other ICPs [21, 22]. Previous publications on *in situ* polymerization of PANI in polymer matrix emulsion were based on traditional slow, dropwise addition of reagents and continuous stirring [23, 24], which frequently results in irregular PANI agglomerates. [21, 25]. In order to produce PHB/PANI nanofiber composites, we performed aniline (Ani) polymerization reaction in the presence of emulsion of PHB in water/chloroform/SDS. In 2007, Ali and co-workers [26] prepared semiconducting PANI/polyvinyl alcohol (PVA) composites containing fibrous nanoclusters and aggregates of PANI, by irradiating a solution of HCl, Ani and PVA with gamma rays up to 50 kGy. Recently, some nanofiber composites of PHB and PANI were fabricated by electrospinning method [27]. However, to our best knowledge, *in situ* chemical polymerization of PANI resulting in nanofibers embedded into polymer matrix was not reported, so far. In this work, we obtained good quality HCl-doped PANI nanofibers/PHB composites presenting semiconductivity and biodegradability. Thus, a new methodology is suggested for the manufacturing of a polymer matrix nanocomposite.

PHB/PANI nanocomposites were gamma-irradiated at 25 kGy dose, the standard sterilization absorbed

dose for medical supplies, in order to assess the effects of such procedure on its electrical conductivity and biodegradability. Our results demonstrate that gamma-irradiation improved electrical conductivity while presenting little influence on the biodegradability of the nanocomposite.

Many uses of this new material can be possible, e.g., as supports for electrically stimulated/guided cell growth, similarly to what is proposed for other PANI/biodegradable polymer nanocomposites [28, 29].

2. Experimental

Aniline monomer (Ani), ammonium peroxydisulfate (APS) and ammonium hydroxyde (NH_4OH) (Vetec, Rio de Janeiro, Brazil), methanol, chloroform and hydrochloric acid (HCl) (Dinâmica, Londrina, Brazil), and sodium dodecylsulfate 99% (SDS) (Sigma-Aldrich, Saint Louis, USA) were of analytical grade. Ani was treated with stannous chloride for 24 h and vacuum distilled prior to use. Chloroform was dried and distilled. Commercial PHB (BIOCYCLE®, M_w 530 kg/mol, PHB Industrial S. A., Usina da Pedra, Brazil) was purified by extraction with methanol in a Soxhlet apparatus for 48 h and air dried before use. Other chemicals were used as received.

A typical procedure for the preparation of PHB/PANI nanocomposites was based on Ruckestein and Yang [23]: a solution of 0.2 g of SDS in 2 ml of distilled deionized water was placed in a 50 ml Becker flask. To a 5 ml chloroform solution containing 0.4 g of PHB, previously dissolved under reflux for 24 hours, was added 0.12 g of Ani, thus Ani to PHB ratio in mass (Ani:PHB) equaled 0.3. The resulting mixture was added to the aqueous solution under intense magnetic stirring, until forming an emulsion. A solution of 0.19 g of the oxidant agent, APS, in 10 ml of HCl 1 mol·dm^{-3} was then placed at once in the emulsion and the stirring was kept working just long enough to allow an homogeneous mixing of the solutions and until an initial changing in the color of the system was perceptible (approximately 40 s). The reaction was left to proceed for 3 hours at room temperature, then quenched with methanol. The precipitate formed was filtered in an Hirsch funnel, washed with methanol followed by water and HCl 1 mol·dm^{-3}. The green coarse powder obtained was dried at room temperature in a desiccator until constant weight and named as composite I. Similar procedure was followed to produce composites having initial Ani:PHB of 0.75, 1.0 and 1.5, keeping all components but Ani in the same proportion (composites I, III and IV, respectively). For comparison, PANI was synthesized in the absence of PHB in the above-described conditions. For the same reason, the PHB chloroform solution was submitted to the emulsification process in the presence of APS and SDS and left to stand for 3 hours before precipitation of the polymer with methanol. Yields were calculated considering 100% as the sum of Ani, PHB and SDS weights in the reactional media [23, 24]. Samples were prepared in duplicate. PANI content in each polymer was determined gravimetrically by extraction of the soluble PHB matrix in a Soxhlet extractor with chloroform. Residual insoluble doped PANI was dried in desiccator until constant weight.

Gamma irradiation of powder samples were done in air, at room temperature, in a Gammacell irradiator (220 SN 65R Source Model Number: C-198 MDS Nordion Inc, Kanata, Canada) at 25 kGy dose and 2.61 Gy·s^{-1} dose rate.

Room temperature electrical conductivity measurements were performed in an eletrometer Keithley (model 617 Keitley Instruments Inc. Cleveland, USA) by the two-probe method on pellets of power samples pressed at 3 MPa for 30 s. Samples were left to rest for 72 h before the readings. The morphologies of the composites were investigated by scanning electron microscopy (SEM) (JEOL JSM-5900, Tokyo, Japan) on gold-coated samples. Fourier Transform Infrared spectrometry (FTIR) experiments were performed on KBr pellets (Bruker IFS66, Ettlinger, Germany). The X-ray diffractograms (Rigaku D/max-2200, Texas, USA) were taken with CuK_α radiation, 1.54 Å, 40 kV, 20 mA, in the range of diffraction angle $2\theta = 5–35°$ in a continuous scanning type at 1.2° per min. The background and the amorphous halo were subtracted according to the methodology established by Ruland [30]. Biodegradability determination followed modified Sturm's test conditions [31], according to ASTM D5338-98 [32]. 0.8 g of the samples and 100 g of inoculant medium (worm humus, Gnumus, Vitória de Santo Antão, Brazil, 50% of dry solids) mixed in 200 ml of distilled water were used in each experiment. Measurements were interrupted

when CO_2 production remained approximately the same as the control sample for at least ten days.
The accumulation of CO_2 (P) was calculated according to the Equation (1):

$$P = \sum_{n=1}^{i} \frac{m_{ai} - m_{ci}}{m_{ci}} \quad (1)$$

where n – number of days, m_{ai} – mass of CO_2 produced by a sample in the i day, m_{ci} – mass of CO_2 produced by the control sample in the i day.
Values were corrected to take in account only PHB percentage in the total sample mass.

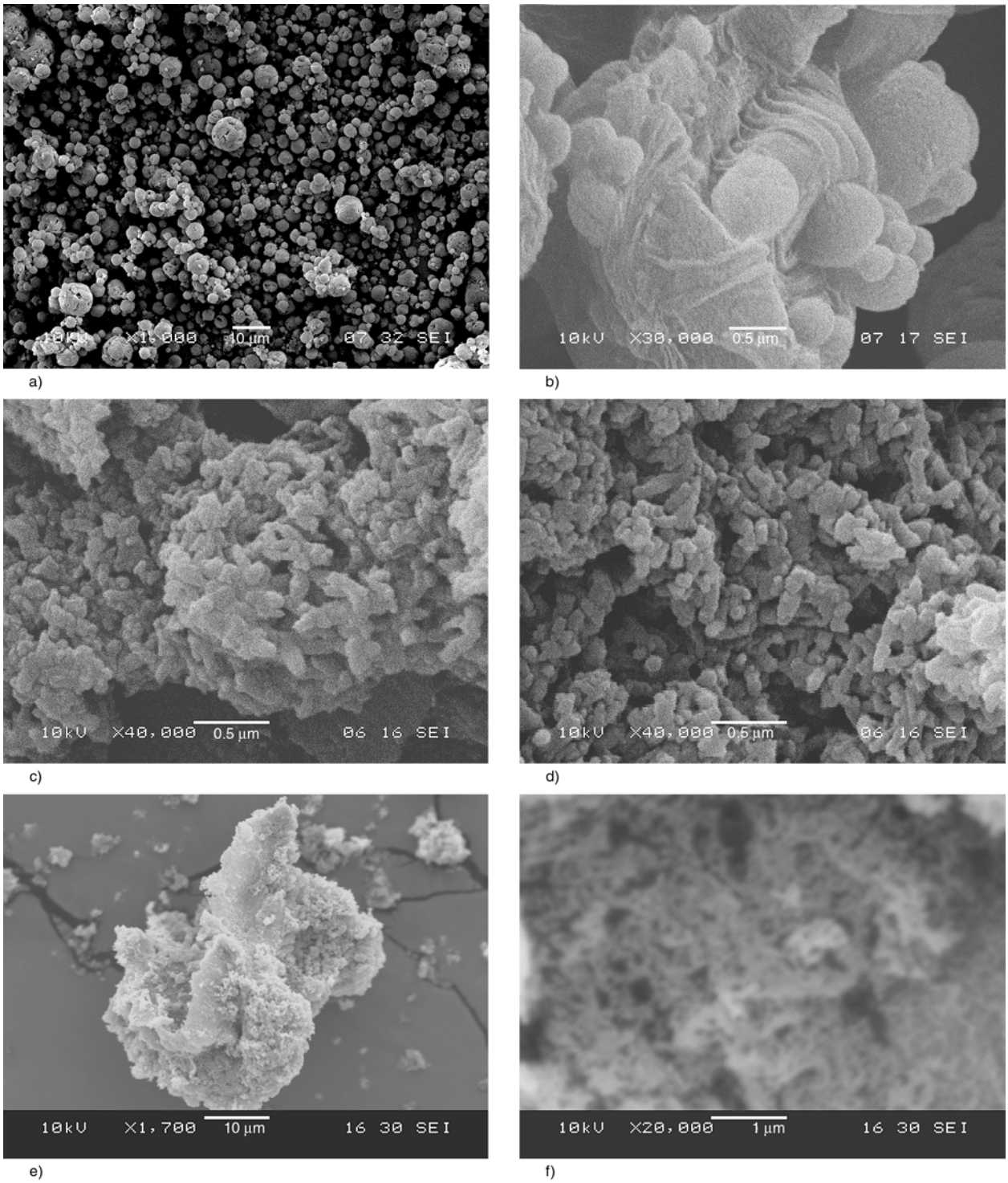

Figure 2. SEM images of neat PHB (a) ×1000, (b) ×30000; PHB/PANI-HCl (c) nanocomposite II, nanocomposite IV. Residual PANI-HCl salt after extraction of PHB fraction with chloroform (e) ×1700 and (f) ×20000.

3. Results and discussion

3.1. Morphology of PHB and PHB/PANI composites

Scanning electron micrographs of treated PHB samples exhibited spherical granules ranging from 10 μm (Figure 2a) to 260 nm (Figure 2b) in diameter. Granules of PHB found in the cytoplasm of the bacteria *Alcaligenes eutrophus*, the microorganism used in the production of Brazilian PHB, presented diameters from 200 to 500 nm [33]. Larger granular structures may be formed during extraction process. Composites of PHB and HCl-doped PANI (PHB/PANI-HCl) presented distinct morphologies from the neat PHB. Figures 2c and 2d show electron micrograph images from composites II and IV where fibers or rods with diameters around 70–100 nm are visualized. After extraction of PHB with chloroform, residual PANI-HCl has a sponge-like appearance (Figure 2e). A network of fibrils can be identified from a higher magnification image (Figure 2f). Images of composite I did not allow a clear visualization of PANI nanostructures. These results characterize formation and good dispersion of PANI-HCl nanofibers into the PHB matrix when polymerized *in situ* with rapid mixing of APS.

Previous works on PANI composites fabricated by *in situ* emulsion polymerization with polystyrene [23] and PMMA [24] used traditional slow addition of reagents during PANI synthesis. Information on the morphology of PANI structures and the methodology for calculating its content in the composite were not given at that time. At the present it is difficult to infer about the role of each emulsion component on the final morphology of PANI when rapid mixing is performed. In one hand, intrinsic fibrillar morphology is reported to be prevalent in both aqueous and organic media [21]. Moreover, nanofibrillar morphology is also observed when PANI synthesis occurs at the interface of water/immiscible organic solvent biphasic systems [21, 34]. Hence, it is arguable the formation of such structures regardless the existence of two solutions of immiscible solvents in an emulsionated media, which is the environment found in our experiment. On the other hand, we used SDS, a surfactant agent to promote emulsification. Since surfactant agents are known to act as soft templates for PANI nanofibers fabrication [35, 36], the SDS influence on nanofiber formation cannot be ruled out.

Our present approach appears to be very promising for the fabrication of fibrilar PANI nanocomposites, because it precludes the use of hard templates, electrospinning apparatus, or ionizing radiation sources in order to obtain nanofibers, and, at the same time, makes possible to embed inexpensive, insoluble, self-assembled HCl-doped PANI nanofibers directly into host polymer matrix.

3.2. Yields, PANI content and electrical conductivity of the PHB/PANI-HCl nanocomposites

Composites obtained as described in the previous section were analyzed for yields, PANI content, and conductivity. Results are shown in Table 1. Nanocomposite I presented the highest yield among the studied materials, followed by nanocomposite IV.

Neat PHB conductivity was in the range of 10^{-12} S/m, while all nanocomposite materials obtained were above the electrical percolation threshold and presented semiconductivity. Since PHB is an electrical insulator, conductivity presented by the composites is due to PANI-HCl. For nanocomposites I–III, conductivities were situated in the same order of magnitude, around $1.0 \cdot 10^{-2}$ S/m. PANI pristine polymerized in the emulsion water/chloroform had a conductivity of 1.2 S/m which is close to the conductivity reached by composite IV, $7.0 \cdot 10^{-1}$ S/m. Fluctuations in conductivity of PANI and its composites prepared under controlled conditions may be attributed to a large number of factors, including the presence of humidity [16], morphology and the dispersion of the filler in the composite [37]. Thus, all the samples presented comparable conductivities and are suitable candidates for applications as semiconducting biomaterials.

Table 1. Yields, PANI-HCl contents, and conductivity of PHB/PANI-HCl composites

Composite PHB/PANI	Ani/PHB ratio	Yield of PHB/PANI [%]	PANI-HCl [%]	PANI-HCl/Ani [%]	Conductivity [S/m]
I	0.30	93	8	43	$2.1 \cdot 10^{-2}$
II	0.75	51	28	45	$4.6 \cdot 10^{-2}$
III	1.00	46	55	64	$1.8 \cdot 10^{-2}$
IV	1.50	71	48	68	$7.0 \cdot 10^{-1}$

As composite II presents good conductivity and the lower PANI-HCl content in which nanofibers could be visualized, it was chosen for experiments of gamma irradiation and biodegradation. After exposed to a 25 kGy absorbed dose, conductivity of nanocomposite II increased in two orders of magnitude and reached 1.1 S/m. Hence, nanocomposite semiconductivity was maintained after irradiation procedure. This result opens up an opportunity for the fabrication of gamma rays-sterilizable, biodegradable, electroactive supports for a number of biotechnology applications.

Very little information is available on conductivity behavior of chemically synthesized PANI exposed to gamma-rays. A direct comparison with previous published results is rather difficult, since most reports are based on conductivity onset observed when gamma radiation induces doping process in insulator PANI emeraldine base, resulting in semiconducting PANI forms, either in composites [38–41] or pristine PANI films [42]. Thus, conductivity increases observed were of several orders of magnitude.

Our material presented semiconducting filler content above the electrical percolation limit, hence radiation-induced conductivity enhancements were smaller than those evidenced in the previously-cited works. Conversely, in a report on conducting PANI pellets subjected to up to 400 kGy dose, no increase in conductivity was detected in the 0–200 kGy dose range, with a less than 25% increase in the 300–400 kGy range [43]. The increase in conductivity was consistent with the increase in spin or radical concentration detected by Electron Paramagnetic Resonance (EPR) measurements. These and other defects are capable of acting as charge carriers throughout ICPs polymer chains [44–46], thus, explaining the higher conductivity observed.

3.3. FTIR analysis

FTIR characterization of PHB and PANI-HCl, nanocomposites II (before and after irradiation at 25 kGy) and nanocomposite IV are presented in Figure 3. PHB spectrum (Figure 3a) exhibits C=O stretching at 1724 cm^{-1} and C–O stretching at 1283 cm^{-1}. These results are in good agreement with previous reports on FTIR data of PHB [47]. PANI-HCl spectrum (Figure 3b) exhibits band at ~1573 cm^{-1} attributed to C=N stretching of the quinoid diimine unit (N=Q=N). C–C aromatic ring stretching of the benzenoid diamine unit (N–B–N) appears at 1481 cm^{-1} [48]. Based on previous reports, the very close intensities presented by these two bands identify the emeraldine oxidation state of PANI [49]. The ~1140 cm^{-1} band is a vibrational mode of B–NH^+=Q or B–NH^+=B. Both bands are related to the doping level of PANI-HCl and can be used as a comparison of PANI doping process when formed *in situ* in the PHB matrix. Nanocomposites II and IV spectra (Figures 3c–3e) exhibit the same major bands present in PHB and PANI-HCl spectrum. Only marginal shifts were detected in these nanocomposites, thus intermolecular interactions between the two components are negligible, e.g., n-π interactions of the unshared pair of electron of the carbonyl group in PHB and the π-electrons of the aromatic ring of PANI-HCl are not as perceptible in these composites, as they are in blends of other carbonyl/aromatic polymers [50, 51]. Comparison between the changing in intensity of ~1303 and ~1140 cm^{-1} bands shows that doping level of PANI HCl in these nanocomposites are similar to the doping level of the product obtained in the absence of PHB, even in the gamma-irradiated nanocomposite II (Figure 3e).

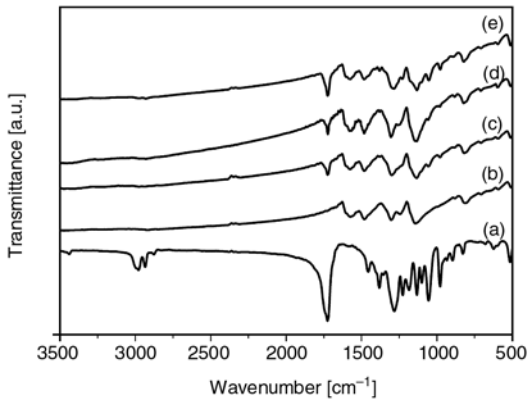

Figure 3. FTIR spectra of (a) PHB, (b) PANI HCl, (c) nanocomposite IV, (d) non-irradiated nanocomposite II and (e) nanocomposite II irradiated at 25 kGy

3.4. XRD analysis

X-ray diffractogram of PHB is shown in Figure 4a. Diffraction peaks in 2θ = 13.4, 16.8, 20, 22.2 and 25.5° have a similar pattern when compared with previous crystallographic data for this material [52]. The degree of crystallinity calculated through Ruland's method considers the total area of the diffracted peaks subtracted of the amorphous halo

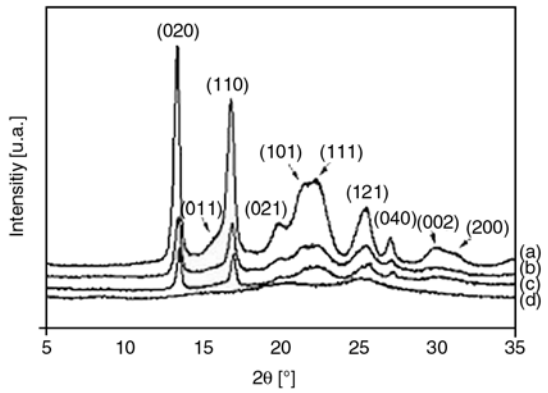

Figure 4. X-ray diffractograms of (a) PHB, (b) nanocomposite II (28% of PANI), (c) nanocomposite IV (45% of PANI) and (d) PANI-HCl

[30]. Our results indicated a degree of crystallinity of 53%. This method was previously used to assess the crystalline fraction of as-supplied Brazilian PHB with similar results [53]. PHB/PANI-HCl nanocomposites II and IV diffraction patterns are very close to those exhibited by neat PHB (Figures 4b and 4c). Nevertheless, it is possible to notice a slight shift to higher angles with the increase of PANI-HCl content, indicating a decrease in the interplanar distance of PHB crystals. In neat PANI-HCl diffractogram, two broad, relatively intense peaks at 20.3 and 25.1° can be seen, along with two less intense 8.5 and 15.0° (Figure 4d). This pattern is related to amorphous polyanilines synthesized in the presence of surfactant agents such as SDS and dodecylbenzenesulfonate (SDBS) [54]. When prepared in the absence of such agents or secondary dopants, PANI diffractograms tend to exhibit a single broad weak peak at $2\theta = 24.7°$ [54, 55]. This evidence may indicate a direct inclusion of SDS surfactant used in the emulsion polymerization. Nevertheless, the absence of new crystalline orders corroborates the assumption of poor interaction between PHB and PANI. Since some characteristic diffraction peaks of PANI-HCl partially overlapped those of PHB, crystalline fraction calculations for the nanocomposites did not present consistent results.

3.5. Biodegradability of PHB/PANI-HCl nanocomposite

Sturm's test was applied to powders of PHB, PANI-HCl and nanocomposite II. Attempts to promote biodegradation of neat non-irradiated and irradiated PANI-HCl under the tested conditions did not result in any appreciable CO_2 production. Changes in PHB biodegradation could be perceived after 10 days. Non-irradiated PHB began to biodegrade releasing lower amounts of CO_2 than the other samples and remained this way until the 50th day. Similarly, irradiated PHB started to evolve lower quantities of CO_2 than non-irradiated and irradiated nanocomposite II around the 15th day. Nanocomposite II presented similar behavior in non-irradiated and irradiated samples until the 22th day, when the irradiated samples started to exhibit a small decrease in CO_2 production. Non-irradiated nanocomposite II maintained higher rates of CO_2 release until the 35th, when biodegradation of both nanocomposites subsided. Neat PHB samples, in turn, showed rampant increase in CO_2 production after the 45th to approximately the 70th day, when both sample media started to show signs of exhaustion. Figure 5a shows *P versus* time (in days). Figure 5b shows the first derivate of *P* as a function of time (d*P*/d*T*) and reveals the differences in biodegradation behavior of the studied samples. Nanocomposite samples have a markedly higher biodegradation around the first month of testing (region I) while neat PHB samples showed increased activity starting in the second month of observations (region II), when practically no activity is detected for nanocomposites biodegradation. CO_2 accumulated values in region II are higher for irradiated neat PHB as evidenced by higher peaks heights for this sample.

Gamma irradiations affected the studied materials in opposite ways: while irradiated neat PHB reached higher values of accumulated CO_2 production than non-irradiated neat PHB samples, irradiated nanocomposite materials showed lower CO_2 accumulation values. Irradiation with gamma rays provokes main chain scissions in PHB structure. In the range of 0–50 kGy, the *G* value (number of scissions per 100 eV of absorbed energy) for BIOCYCLE® is 15.7 [53]. This number of scissions is large enough to reduce the initial molar mass in one order of magnitude after a 25 kGy absorbed dose. Such damage might ease the biodegradation process in neat samples and explain higher CO_2 production of these materials. In nanocomposites, radiolysis may not be as remarkable because of a putative radiostabilization of PANI-HCl on PHB matrix, in the same fashion reported for PMMA [19, 20]. Moreover,

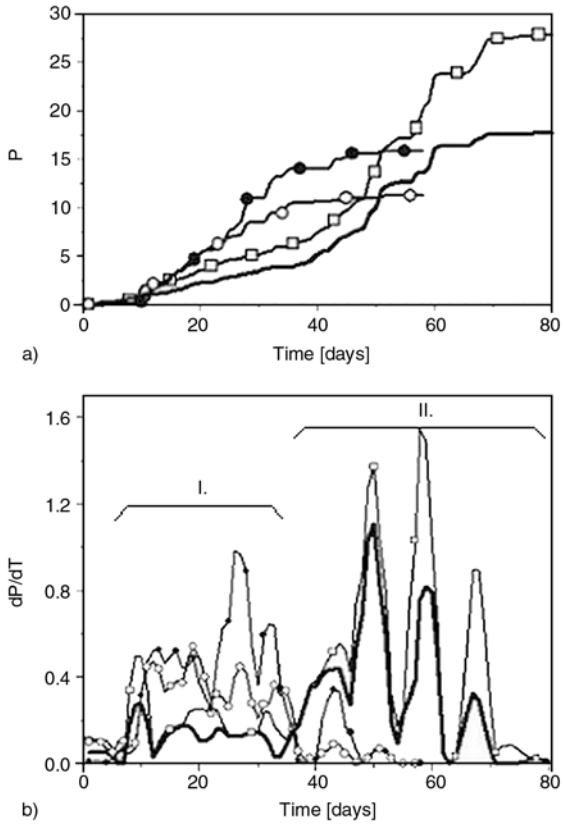

Figure 5. a) Accumulation of CO_2 (P) of powder samples of PHB: non-irradiated (—) and irradiated at 25 kGy (–□–); PHB/PANI-HCl (28% of PANI-HCl) non-irradiated (–●–) and irradiated 25 kGy (–o–). Results are normalized by the P value of the control (inoculant media). Results for the nanocomposite II were also corrected by the percentage of PHB present (72%). b) First derivative of P in time. Region I shows roughly the first month of observations, when intense peaks associated with nanocomposite biodegradation are present, while neat PHB samples show relatively low CO_2 accumulation. Region II delimits approximately the final 40 days of observation, when most of the neat PHB biodegradation occurs.

differences in biodegradation of irradiated neat PHB matrix and PANI nanocomposite may be governed by other factors, as minor alterations caused by irradiation on the surface of the nanocomposite.

PANI presents good biocompatibility, either in its emeraldine, nigraniline or leucoemeraldine oxidation states [17]. Moreover, the presence of electrically conducting PANI in polymer nanocomposites with biodegradable polymers allows the fabrication of suitable substrates for tissue engineering, in which electrical stimulation is important to promote cell proliferation and tissue regeneration [28, 29]. PHB/PANI nanocomposites presented in this work have the basic requirements to become one of these multifunctional nanotechnology materials, as they are composed of biocompatible polymers and possess electrical semiconductivity.

Many factors, besides materials biocompatibility may also interfere in substrate performance, e.g. minor synthesis residues such as oligoanilines and toxic unreacted aniline monomers. Thus, further investigations are needed in order to assess the viability of cell attachment and proliferation on the surface of the nanocomposites presented in this work, as well as the influence of electrical stimulation on these and other cytological processes.

4. Conclusions

PHB/PANI-HCl nanocomposites were obtained by *in situ* emulsion polymerization of HCl-doped PANI, with rapid mixing of oxidant, in the presence of dissolved PHB. The nanofiller presented fibrillar or rod-like shape and 70–100 nm in diameter. Conductivity of the nanocomposites were in the range of 10^{-4} to 10^{-2} S/cm. FTIR analysis revealed similar doping levels in PANI-HCl when embedded into the PHB matrix or in the pristine form. XRD patterns of the semicrystalline PHB were present in nanocomposites and PHB diffractograms. PANI-HCl peaks suggested some degree of association with a surfactant agent, SDS, used to promote emulsification. Nevertheless, FTIR and XRD data did not show evidence of significant interactions between PHB and PANI-HCl nanofibers in the composite. Biodegradation experiments showed that PHB biodegradability is enhanced after irradiation at 25 kGy. Biodegradation of non-irradiated and irradiated PHB occur more intensely after 30 days, but with a larger accumulated production of CO_2 detected for the irradiated samples. PHB/PANI-HCl nanocomposites present a faster biodegradation than PHB in the first month of measurements. After this period, nanocomposite biodegradation subsided. Irradiated samples exhibited a decrease in the biodegradation process of the nanocomposite after the 22th day of testing. Therefore, accumulated CO_2 production is higher in the non-irradiated samples. Neat PANI-HCl biodegradation is negligible when compared to PHB biodegradability in an 80 day timeframe.

Acknowledgements

The authors acknowledge The Brazilian Research Council (CNPq) for financial support and PHB Industrial S. A. for kindly supplying BIOCYCLE® samples.

References

[1] Jayasekara R., Harding I., Bowater I., Lonergan G.: Biodegradability of a selected range of polymers and polymer blends and standard methods for assessment of biodegradation. Journal of Polymers and the Environment, **13**, 231–251 (2005).
DOI: 10.1007/s10924-005-4758-2

[2] Chen G-Q., Wu Q.: The application of polyhydroxyalkanoates as tissue engineering materials. Biomaterials, **26**, 6565–6578 (2005).
DOI: 10.1016/j.biomaterials.2005.04.036

[3] Piskin E., Bölgen N., Egri S., Isoglu I. A.: Electrospun matrices made of poly(α-hydroxy acids) for medical use. Nanomedicine, **2**, 441–457 (2007).
DOI: 10.2217/17435889.2.4.441

[4] Müller H-M., Seebach D.: Poly(hydroxyalkanoates): A fifth class of physiologically important organic biopolymers? Angewandte Chemie International Edition, **32**, 477–502 (1993).
DOI: 10.1002/anie.199304771

[5] Gursel I., Yagmurlu F., Korkusuz F., Hasirci V.: In vitro antibiotic release from poly(3-hydroxybutyrate-*co*-3-hydroxyvalerate) rods. Journal of Microencapsulation, **19**, 153–164 (2002).
DOI: 10.1080/02652040110065413

[6] Khang G., Kim S. W., Cho J. C., Rhee J. M., Yoon S. C., Lee H. B.: Preparation and characterization of poly(3-hydroxybutyrate-*co*-3-hydroxyvalerate) microspheres for the sustained release of 5-fluorouracil. Bio-Medical Materials and Engineering, **11**, 89–103 (2001).

[7] Sudesh K., Abe H., Doi Y.: Synthesis, structure and properties of polyhydroxyalkanoates: Biological polyesters. Progress in Polymer Science, **25**, 1503–1555 (2000).
DOI: 10.1016/S0079-6700(00)00035-6

[8] Bordes P., Pollet E., Bourbigot S., Avérous L.: Structure and properties of PHA/clay nano-biocomposites prepared by melt intercalation. Macromolecular Chemistry and Physics, **209**, 1473–1484 (2008).
DOI: 10.1002/macp.200800022

[9] Choi W. M., Kim T. W., Park O. O., Chang Y. K., Lee J.W.: Preparation and characterization of poly(hydroxybutyrate-*co*-hydroxyvalerate)–organoclay nanocomposites. Journal of the Applied Polymer Science, **90**, 525–529 (2003).
DOI: 10.1002/app.12702

[10] Lai M., Li J., Yang J., Liu J., Tong X., Cheng H.: The morphology and thermal properties of multi-walled carbon nanotube and poly(hydroxybutyrate-*co*-hydroxyvalerate) composite. Polymer International, **53**, 1479–1484 (2004).
DOI: 10.1002/pi.1566

[11] Stafström S., Brédas J. L., Epstein A. J., Woo H. S., Tanner D. B., Huang W. S. MacDiarmid A. G.: Polaron lattice in highly conducting polyaniline: Theoretical and optical studies. Physical Review Letters, **59**, 1464–1467 (1987).
DOI: 10.1103/PhysRevLett.59.1464

[12] Lee M. H., Speyer G., Sankey O. F.: Theory of electron transport through single molecules of polyaniline. Journal of Physics: Condensed Matter, **19**, 215204/1–215204/16 (2007).
DOI: 10.1088/0953-8984/19/21/215204

[13] Cottevieille D., Le Méhauté A., Challioui C., Mirebeau P., Demay J. N.: Industrial applications of polyaniline. Synthetic Metals, **101**, 703–704 (1999).
DOI: 10.1016/S0379-6779(98)01093-5

[14] Dutta D., Sarma T. K., Chowdhury D., Chattopadhyay A.: A polyaniline-containing filter paper that acts as a sensor, acid, base, and endpoint indicator and also filters acids and bases. Journal of Colloid and Interface Science, **283**, 153–159 (2005).
DOI: 10.1016/j.jcis.2004.08.051

[15] Pron A., Rannou P.: Processible conjugated polymers: From organic semiconductors to organic metals and superconductors. Progress in Polymer Science, **27**, 135–190 (2002).
DOI: 10.1016/S0079-6700(01)00043-0

[16] Chiang J. C., MacDiarmid A. G.: 'Polyaniline': Protonic acid doping of the emeraldine form to the metallic regime. Synthetic Metals, **13**, 193–205 (1986).
DOI: 10.1016/0379-6779(86)90070-6

[17] Wang C. H., Dong Y. Q., Sengothi K., Tan K. L., Kang E. T.: *In-vivo* tissue response to polyaniline. Synthetic Metals, **102**, 1313–1314 (1999).
DOI: 10.1016/S0379-6779(98)01006-6

[18] Kang E. T., Neoh K. G., Tan K. L.: Polyaniline: A polymer with many interesting intrinsic redox states. Progress in Polymer Science, **23**, 277–324 (1998).
DOI: 10.1016/S0079-6700(97)00030-0

[19] Araujo P. L. B., Santos R. F. S., Araujo E. S.: Polyaniline nanofibers as a new gamma radiation stabilizer agent for PMMA. Express Polymer Letters, **1**, 385–390 (2007).
DOI: 10.3144/expresspolymlett.2007.54

[20] Araujo P. L. B., Aquino K. A. S., Araujo E. S.: Effects of gamma irradiation on PMMA/polyaniline nanofibre composites. International Journal of Low Radiation, **4**, 149–160 (2007).
DOI: 10.1504/IJLR.2007.015439

[21] Huang J., Kaner R. B.: The intrinsic nanofibrillar morphology of polyaniline. Chemical Communications, 367–376 (2006).
DOI: 10.1039/b510956f

[22] Chien J. C. W., Yamashita Y., Hirsch J. A., Fan J. L., Schen M. A., Karasz F. E.: Resolution of controversy concerning the morphology of polyacetylene. Nature, **299**, 608–611 (1982).
DOI: 10.1038/299608a0

[23] Ruckenstein E., Yang S.: An emulsion pathway to electrically conductive polyaniline-polystyrene composites. Synthetic Metals, **53**, 283–292 (1993).
DOI: 10.1016/0379-6779(93)91097-L

[24] Yang S., Ruckenstein E.: Processable conductive composites of polyaniline/poly(alkyl methacrylate) prepared via an emulsion method. Synthetic Metals, **59**, 1–12 (1993).
DOI: 10.1016/0379-6779(93)91152-R

[25] Huang J., Kaner R. B.: Nanofiber formation in the chemical polymerization of aniline: A mechanistic study. Angewandte Chemie, **113**, 5941–5945 (2004).
DOI: 10.1002/ange.200460616

[26] Ali M. A., Saion E., Yahya N., Kassim A., Dahlan K. M., Hashim S.: Synthesis of conducting polyaniline nanocomposites by radiation doping. Journal of Engineering Science and Technology, **2**, 111–118 (2007).

[27] Fryczkowski R., Kowalczyk T.: Nanofibres from polyaniline/polyhydroxybutyrate blends. Synthetic Metals, **159**, 21–22 (2009).
DOI: 10.1016/j.synthmet.2009.09.008

[28] Ghasemi-Mobarakeh L., Prabhakaran M. P., Morshed M., Nasr-Esfahani M. H., Ramakrishna S.: Electrical stimulation of nerve cells using conductive nanofibrous scaffolds for nerve tissue engineering. Tissue Engineering Part A, **15**, 3605–3619 (2009).
DOI: 10.1089/ten.tea.2008.0689

[29] McKeon K. D., Lewis A., Freeman J. W.: Electrospun poly(D,L-lactide) and polyaniline scaffold characterization. Journal of Applied Polymer Science, **115**, 1566–1572 (2009).
DOI: 10.1002/app.31296

[30] Ruland W.: X-ray determination of crystallinity and diffuse disorder scattering. Acta Crystallographica, **14**, 1180–1185 (1961).
DOI: 10.1107/S0365110X61003429

[31] Calil M. R., Gaboardi F., Guedes C. G. F., Rosa D. S.: Comparison of the biodegradation of poly(ε-caprolactone), cellulose acetate and their blends by the Sturm test and selected cultured fungi. Polymer Testing, **25**, 597–604 (2006).
DOI: 10.1016/j.polymertesting.2006.01.019

[32] ASTM D5338-98.: Standard test method for determining aerobic biodegradation of plastic materials under controlled composting conditions (2003).

[33] Anderson A. J., Dawes, E. A.: Occurrence, metabolism, metabolic role, and industrial uses of bacterial polyhydroxyalkanoates. Microbiological Reviews, **54**, 450–472 (1990).

[34] Huang J. X., Virji S., Weiller B. H., Kaner R. B.: Polyaniline nanofibers: Facile synthesis and chemical sensors. Journal of the American Chemical Society, **125**, 314–315 (2003).
DOI: 10.1021/ja028371y

[35] Hopkins A. R., Lipeles R. A., Kao W. H.: Electrically conducting polyaniline microtube blends. Thin Solid Films, **447–448**, 474–480 (2004).
DOI: 10.1016/j.tsf.2003.07.010

[36] Carswell A. D. W., O'Rear E. A., Grady B. P.: Adsorbed surfactants as templates for the synthesis of morphologically controlled polyaniline and polypyrrole nanostructures on flat surfaces: From spheres to wires to flat films. Journal of the American Chemical Society, **125**, 14793–14800 (2003).
DOI: 10.1021/ja0365983

[37] Pan W., Yang S. L., Li G., Jiang J. M.: Electrical and structural analysis of conductive polyaniline/polyacrylonitrile composites. European Polymer Journal, **41**, 2127–2133 (2005).
DOI: 10.1016/j.eurpolymj.2005.04.003

[38] Sevil U. A., Güven O., Süzer S.: Spectroscopic investigation of onset and enhancement of electrical conductivity in PVC/PANI composites and blends by γ-ray or UV irradiation. Journal of Physical Chemistry B, **102**, 3902–3905 (1998).
DOI: 10.1021/jp980369z

[39] Sevil U. A., Güven O., Birer O., Şüzer S.: Doping of 2-Cl-PANI/PVC films by exposure to UV, γ-rays and e-beams. Synthetic Metals, **110**, 175–179 (2000).
DOI: 10.1016/S0379-6779(99)00266-0

[40] Sevil U. A., Güven O., Kovács A., Slezsák I.: Gamma and electron dose response of the electrical conductivity of polyaniline based polymer composites. Radiation Physics and Chemistry, **67**, 575–580 (2003).
DOI: 10.1016/S0969-806X(03)00108-7

[41] Bodugöz H., Güven O.: Radiation induced dehydrochlorination as an in-situ doping technique for enhancement of the conductivity of polyaniline blends. Nuclear Instruments and Methods in Physics Research Section B: Beam Interactions with Materials and Atoms, **236**, 153–159 (2005).
DOI: 10.1016/j.nimb.2005.04.009

[42] Azevedo W. M., de Costa Lima A. P., Araujo E. S.: Radiation induced effects on electrical properties of polyaniline. Radiation Protection Dosimetry, **84**, 77–81 (1999).

[43] Yao Q., Liu L., Li C.: Radiation induced variations of electrical conductivity in polyaniline. Chinese Physics Letters, **11**, 113–115 (1994).
DOI: 10.1088/0256-307X/11/2/014

[44] Fesser K.: Interchain coupling in *trans*-polyacetylene. Physical Review B, **40**, 1962–1965 (1989).
DOI: 10.1103/PhysRevB.40.1962

[45] Krinichnyi V. I., Chemerisov S. D., Lebedev Ya. S.: EPR and charge-transport studies on polyaniline. Physical Review B, **55**, 16233–16244 (1997).
DOI: 10.1103/PhysRevB.55.16233

[46] Kivelson S.: Frustration, fractional charge, and soliton mobilities: The effect of interchain coupling on solitons in charge-density waves. Physical Review B, **26**, 7093–7096 (1982).
DOI: 10.1103/PhysRevB.26.7093

[47] Xu J., Guo B-H., Yang R., Wu Q., Chen G. Q., Zhang Z-M.: In situ FTIR study on melting and crystallization of polyhydroxyalkanoates. Polymer, **43**, 6893–6899 (2002).
DOI: 10.1016/S0032-3861(02)00615-8

[48] Tang J., Jing X., Wang B., Wang F.: Infrared spectra of soluble polyaniline. Synthetic Metals, **24**, 231–238 (1988).
DOI: 10.1016/0379-6779(88)90261-5

[49] Abdiryim T., Zhang X-G., Jamal R.: Comparative studies of solid-state synthesized polyaniline doped with inorganic acids. Materials Chemistry and Physics, **90**, 367–372 (2005).
DOI: 10.1016/j.matchemphys.2004.10.036

[50] Koenig J. L.: Spectroscopy of polymers. Elsevier, Amsterdam (1999).

[51] Mohamed A., Gordon S. H., Biresaw G.: Polycaprolactone/polystyrene bioblends characterized by thermogravimetry, modulated differential scanning calorimetry and infrared photoacoustic spectroscopy. Polymer Degradation and Stability, **92**, 1177–1185 (2007).
DOI: 10.1016/j.polymdegradstab.2007.04.012

[52] Ikejima T., Inoue Y.: Crystallization behavior and environmental biodegradability of the blend films of poly(3-hydroxybutyric acid) with chitin and chitosan. Carbohydrate Polymers, **41**, 351–356 (2000).
DOI: 10.1016/S0144-8617(99)00105-8

[53] Oliveira L. M., Araujo E. S., Guedes S. M. L.: Gamma irradiation effects on poly(hydroxybutyrate). Polymer Degradation and Stability, **91**, 2157–2162 (2006).
DOI: 10.1016/j.polymdegradstab.2006.01.008

[54] Cai L-T., Yao S-B., Zhou S-M.: Improved conductivity and electrical properties of polyaniline in the presence of rare-earth cations and magnetic field. Synthetic Metals, **88**, 205–212 (1997).
DOI: 10.1016/S0379-6779(97)03851-4

[55] MacDiarmid A. G., Epstein A. J.: The concept of secondary doping as applied to polyaniline. Synthetic Metals, **65**, 103–116 (1994).
DOI: 10.1016/0379-6779(94)90171-6

eXPRESS Polymer Letters Vol.5, No.1 (2011) 23–37
Available online at www.expresspolymlett.com
DOI: 10.3144/expresspolymlett.2011.4

Linear low density polyethylene/cycloolefin copolymer blends

A. Dorigato[1], A. Pegoretti[1], L. Fambri[1], C. Lonardi[1], M. Šlouf[2], J. Kolařik[2]*

[1]University of Trento, Department of Materials Engineering and Industrial Technologies, via Mesiano 77, 38123 Trento, Italy
[2]Institute of Macromolecular Chemistry, Academy of Sciences of the Czech Republic, v.v.i., Heyrovskeho namesti 2, 162 06 Prague 6, Czech Republic

Received 28 June 2010; accepted in revised form 10 September 2010

Abstract. Linear low density polyethylene (LLDPE) was melt compounded with various amounts of a cycloolefin copolymer (COC). Scanning and transmission electron microscopy evidenced, at qualitative level, some interfacial adhesion between LLDPE and COC. Another indication of interactions between the components was the increase of crystallinity degree with rising COC content and the enhancement of COC glass transition temperature with the LLDPE fraction. In order to explain this behaviour, the incorporation of ethylene segments of COC into the LLDPE crystalline phase, leading to an increased number of norbornene units in the remaining COC component undergoing the glass transition, was hypothesized. The thermo-oxidative degradation stability of LLDPE was substantially enhanced by COC introduction for filler contents higher than 20 wt%, especially when an oxidative atmosphere was considered. An increasing fraction of COC in the blends was responsible for an enhancement of the elastic modulus and of a decrease in the strain at break, while tensile strength passed through a minimum, in agreement with the model predictions based on the equivalent box model and equations provided by the percolation theory. The introduction of a rising COC amount in the blends increased the maximum load sustained by the samples in impact tests, but decreased the blend ductility. Concurrently, a significant reduction of the creep compliance of LLDPE was observed for COC fractions higher than 20 wt%.

Keywords: *polymer blends and alloys, polyethylene, cycloolefin copolymer, mechanical properties*

1. Introduction

In the last years a rising scientific and technological interest emerged towards the possibility of mixing two or more polymers, in order to produce new materials, with properties different from those of the parent components [1–4]. Thermoplastic polymers recently synthesized by means of metallocene-based catalysts have attracted the attention of many researchers and producers. Particular interest has been focused on the synthesis and characterization of cycloolefin copolymers (COCs) [5–13], which are amorphous thermoplastics obtained by copolymerization of norbornene and ethylene. COCs show remarkable properties, such as stiffness, high chemical resistance, good moisture barrier, low moisture absorption and low density. Because of this unique combination of properties, COCs are suitable for the production of transparent mouldings (optical data storage, lenses and sensors), packaging of drugs, medical and diagnostic devices, food containers, etc. As the glass transition temperature (T_g) of COCs can be adjusted by the percentage of norbornene [14–16], various COC grades suitable for specific applications are available on the market. In order to improve dimensional stability, polyolefinic materials have recently been

*Corresponding author: andrea.dorigato@ing.unitn.it

blended with COC. Kolařik *et al*. prepared and characterized polypropylene (PP)/COC blends [17, 18] and high-density polyethylene (HDPE)/COC blends [19, 20], showing how the COC minority component in form of short fibers or microdomains markedly affects the mechanical properties of the resulting materials. PP/COC blends were also prepared by Pimbert [21], finding that the crystallization and nucleation modes of PP seem to be largely influenced by the characteristics of the micro-dispersed phase. Also Šlouf *et al*. [22] studied PP/COC blends, observing uncommon formation of a fibrous morphology of the minority COC component. Similarly to other thermoplastic brittle polymers, it is also possible to improve the fracture toughness of the pristine COC by adding small quantities of elastomers. For instance, Stricker *et al*. [23] studied the influence of polystyrene-block-poly(ethene-co-but-1-ene)-block-polystyrene (SEBS) on the mechanical properties of COCs, finding that the notched impact strength of COC was noticeably improved by the addition of SEBS. Furthermore, Khanarian [24] presented a study in which the toughness of COCs was remarkably improved by the addition of small quantities of styrene-butadiene-styrene rubber (SBS), while the original optical transparency was preserved.

Polyethylene is the most widely used commercial thermoplastic, because of its combination of low cost, high chemical resistance and relatively good mechanical properties [25–28]. HDPE is utilized for commodities but also in a variety of high demanding applications such as the production of pipes and fittings for the transportation of water or gas under pressure. On the other hand, low-density polyethylene (LDPE) and linear low-density polyethylene (LLDPE) are mostly used in film production for the packaging industry, because of their high tear and impact strength. LLDPE is a copolymer of ethylene and an α-olefin or diene, such as butene, hexene and octene [27], constituted by a linear backbone with little chain branching. Despite all its attributes, LLDPE is not an ideal material for films, where it is most commonly used. In fact LLDPEs polymerized by means of the Ziegler-Natta catalysts (*z*LLDPE) contain a low-molecular-weight extractable component (n-hexane) which accounts for low clarity and low gloss of produced films. LLDPEs synthesized by metallocene catalysis (*m*LLDPE) show several advantages over *z*LLDPE, such as higher strength, better optical properties, narrow molecular weight distribution and low extractable fraction. On the other hand, *m*LLDPE is more difficult to be processed into films [29]. Furthermore, relatively poor creep resistance is considered as one of the main deficiencies of LLDPEs. In fact, in many intended applications, these polymers are often required to sustain long lasting constant loads with limited deformation [30]. In general, the incorporation of fillers in LLDPE increases the elastic modulus of the material and its tensile strength, but often decreases the elongation at break [31]. Thus, mixing LLDPE with a yield- and/or creep-resistant polymer is still an interesting area of materials research. Handge *et al*. [32] and Liu *et al*. [33] prepared polystyrene (PS)/LLDPE blends, while Zhang and coworkers [34, 35] utilized different kinds of organic compatibilizers to enhance the interface adhesion in polyethylene terephthalate (PET)/LLDPE blends. Ismail *et al*. [36] investigated the processability and miscibility of LLDPE/ polyvinylalcohol (PVA) systems at different blend ratios, finding that the difference in polarity caused very low miscibility of the two components. Su *et al*. [37] prepared blends of polylactic acid (PLA) and LLDPE in order to investigate the role of the glycidyl methacrylate (GMA)-grafted polyethylene-octene copolymer as potential compatibilizer in these systems. Some papers can also be found in literature on the morphology and thermo-mechanical behavior of the LLDPE/rubber blends [38–41]. In general, preparation of such LLDPE based blends may be rather difficult because the compatibility of the polymers will probably be limited [1, 4, 42–44]. Attainment of satisfactory mechanical properties of blends frequently depends on finding a suitable compatibilizer that allows for sufficient interfacial adhesion, finer phase structure, lower tendency to phase structure coarsening, etc [19, 20, 45]. For these reasons, search for 'reinforcing' components imparting better mechanical properties to LLDPE matrices remains a problem to resolve.

Because of a high fraction of ethylene units, COC is likely to be compatible with polyethylene and other polyolefins without addition of special compatibilizers [2, 17, 18, 22, 46, 47]. Very recently, Lamnawar *et al*. [48] has investigated the rheological

and morphological behavior of the LLDPE/COC blends, with particular attention to their peel seal characteristics to films of either PE or PET. Dynamic rheological measurements and scanning electron microscopy techniques confirmed good compatibility of LLDPE and COC with important consequences for the industrial potential of these systems in the production of thin films for packaging applications. To the best of our knowledge, no papers can be found on the correlation between phase structure and the thermo-mechanical properties of the LLDPE/COC blends.

The objective of this work is to prepare LLDPE/COC blends by melt mixing and to elucidate the effect of morphology and of the physical interactions between the components on the thermo-mechanical properties of the resulting blends, with particular attention to their creep behavior.

2. Experimental part

2.1. Materials and sample preparation

Cycloolefin copolymer supplied by Ticona (Kelsterbach, Germany), known under the trade name of Topas® 8007 (MFI at 190°C and 2.16 kg = 1.7 g·(10 min)$^{-1}$, density = 1.02 g·cm^{-3}), was melt compounded with a Clearflex® CL106 linear low density polyethylene (density = 0.92 g·cm^{-3}, MFI at 190°C and 2.16 kg = 3.2 g·(10 min)$^{-1}$), kindly provided by Polimeri Europa (Mantova, Italy). Both polymer chips were utilized as received. The samples were prepared through a melt compounding process, by using a Haake Rheomix® 600 (Karlsruhe, Germany) internal mixer at 190°C for 15 minutes at 90 rpm, followed by hot pressing at the same temperature in a Carver® (Wabash, IN, USA) laboratory press. In this way, square samples 20 cm and 0.7 mm thick were produced. Neat polyethylene and cycloolefin copolymer matrices were denoted respectively as PE and COC, while the blends were designated with the weight fractions of PE and COC. For instance, PE80COC20 indicates a sample constituted by 80 wt% of PE and 20 wt% of COC (Table 1).

Table 1. Composition of the prepared PE/COC blends

Sample	COC weight fraction	COC volume fraction
PE	0	0
PE80COC20	0.2	0.18
PE60COC40	0.4	0.38
PE50COC50	0.5	0.47
PE40COC60	0.6	0.58
PE20COC80	0.8	0.78
COC	1.0	1.00

2.2. Experimental techniques

The morphology of the prepared samples was investigated by electron microscopy techniques. SEM images of the fracture surfaces of the blends were taken by using a Jeol JSM 6400 (Tokyo, Japan) microscope. The samples were fractured in liquid nitrogen and observed after a sputtering process with platinum. STEM images were collected by a Vega TS 5130 (Brno, Czech Republic) microscope. Thin sections of the samples were ultramicrotomed at –130°C and stained with RuO_4 vapors before the observations.

DSC tests were conducted by using a Mettler DSC30 (Schwerzenbach, Switzerland) calorimeter, under a nitrogen flow of 100 ml·min^{-1}. The samples were heated from 0 to 200°C at 10°C·min^{-1} and then cooled down to 0°C at the same rate. A second heating run up to 200°C was then carried out under the same conditions as the first run. In this way it was possible to evaluate the melting temperature of PE in the blends and its crystallinity (X_{PE}), computed as the ratio of the melting enthalpy (ΔH_m), normalized for the effective weight fraction of LLDPE in the blends (f), and the reference value of the fully crystalline polyethylene (ΔH_0), taken as 293.6 J·g^{-1} [49], as reported in Equation (1):

$$X_{PE} = 100 \cdot \frac{\Delta H_m}{\Delta H_0 \cdot f} \quad (1)$$

Thermogravimetric analysis (TGA) was conducted by using a Mettler TG50 (Schwerzenbach, Switzerland) thermobalance from 30 to 600°C at a heating rate of 10°C·min^{-1}. Various atmospheres were used (nitrogen, air, oxygen), keeping a constant flow of 150 ml·min^{-1}. The temperatures associated to a mass loss of 2% ($T_{2\%}$) and of 5% ($T_{5\%}$), and the maximum mass loss rate temperature (T_d) were determined on the TGA plots. Dynamic mechanical thermal analysis (DMTA) test was carried out under tensile configuration with a MkII Polymer Laboratories (Loughborough, UK) analyzer, in the temperature range from –135 to 130°C at a heating rate of 3°C·min^{-1}. A sinusoidal displacement with a peak-

to-peak amplitude of 64 μm and a frequency of 1 Hz was imposed to the samples.

Quasi-static uniaxial tensile tests were performed with an Instron 4502 (Norwood, MA, USA) testing machine, equipped with a 1 kN load cell, on ISO 527-1BA samples, having a gage length of 30 mm and a width of 5 mm. Tensile tests up to break were performed at a crosshead speed of 50 mm·min^{-1} (strain rate = 167%·min^{-1}). At least five specimens for each blend sample were tested. In order to evaluate more accurately the deformation of the samples, tensile tests for the determination of the elastic modulus were conducted at a lower speed (0.25 mm·min^{-1}), and the strain was monitored by an Instron 2620-601 (Norwood, MA, USA) clip-on resistance extensometer, with a gage length of 12.5 mm (strain rate = 2%·min^{-1}). According to ISO 527 standard, the elastic modulus of the blends (E_b) was determined on at least five specimens as a secant value between the strain levels of 0.05 and of 0.25%.

Tensile impact tests were conducted on ISO 527-1BA specimens with a CEAST (Turin, Italy) instrumented impact pendulum using a striker mass of 3.65 kg and an impact speed of 1.25 m·s^{-1} (with an overall impact energy of about 2.85 J). Also in this case five specimens were tested for each sample.

Isothermal creep tests were carried out at 30°C by an Instron 4502 (Norwood, MA, USA) testing machine. In order to avoid problems related to the precise determination of the effective gage length and to measure with more accuracy the creep strain, rectangular samples, 100 mm long, 5 mm wide and 0.7 mm thick, with a gage length of 60 mm, were utilized. Each sample was tested imposing different stress levels (σ_0), ranging from 20 to 60% of the yield strength, for a total duration of 1 hour. Tensile creep compliance $D(t)$ was computed by dividing the time dependent strain $\varepsilon(t)$ by the constant stress (σ). Isochronous stress-strain curves were then constructed considering the strain of the specimens at different creep stresses at selected times between 600 and 3600 s.

2.3. Theoretical background

The equivalent box model (EBM) combined with the percolation approach to the phase continuity was utilized to predict the modulus and the stress at break of the polymer blends under investigation.

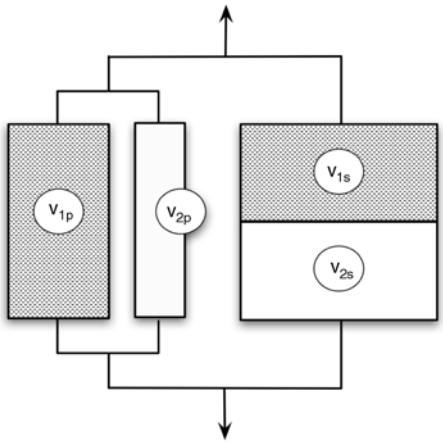

Figure 1. Schematic representation of the equivalent box model (EBM)

Generally speaking, polymer blends are heterogeneous isotropic materials with three-dimensional continuity of one or more components. For this reason, simple parallel or series models or the models for orthotropic or quasi-isotropic materials are not applicable [50]. In our previous paper [18], the predictive capacity of the modified EBM was successfully verified.

The EBM (Figure 1) operates with partly parallel (subscript *p*) and partly series (subscript *s*) couplings of two components. This EBM is a two-parameter model as of four volume fractions (v_{ij}) only two are independent variables. The volume fractions are interrelated as reported in Equation (2a) and Equation (2b):

$$v_1 = v_{1p} + v_{1s} \tag{2a}$$

$$v_2 = v_{2p} + v_{2s} \tag{2b}$$

where $v_1 + v_2 = v_p + v_s = 1$. The blocks in the EBM are presumed to have physical properties of the neat components. For this reason the EBM is likely to fail if the mixing process produces significant changes in the structure and properties of the blend components. As the EBM is not a self-consistent model, the predictive format requires two steps: the derivation of the equations for the properties under consideration and the calculation of the volume fractions (v_{ij}) by using equations rendered by the percolation theory [51–53]. Elastic moduli of the parallel (E_p) and series (E_s) branches of the EBM can be computed as indicated in Equation (3a) and in Equation (3b):

$$E_p = \frac{E_1 v_{1p} + E_2 v_{2p}}{v_p} \tag{3a}$$

$$E_s = \frac{v_s}{\frac{v_{1s}}{E_1} + \frac{v_{2s}}{E_2}} \quad (3b)$$

The resulting tensile modulus of two-component systems (E_b) is then given as reported in Equation (4):

$$E_b = E_p v_p + E_s v_s = E_1 v_{1p} + E_2 v_{2p} + \frac{v_s^2}{\frac{v_{1s}}{E_1} + \frac{v_{2s}}{E_2}} \quad (4)$$

The tensile stress at break (σ_b) of blends obeys the following expression (Equation (5)), derived in terms of the EBM [50, 54]:

$$\sigma_b = \sigma_{b1} \cdot v_{1p} + \sigma_{b2} \cdot v_{2p} + A \cdot \sigma_{b1} \cdot v_s \quad (5)$$

where σ_{b1} or σ_{b2} denotes the tensile stress at break of the components, while A is a parameter correlated to the extent of interfacial debonding ($0 \leq A \leq 1$). Two limiting values of σ_b can be distinguished by means of Equation (5). If $A = 0$, the interfacial adhesion is so weak that complete debonding occurs before the fracture of the component fractions coupled in series. Consequently, as a function of blend composition, σ_b passes through a minimum. If $A = 1$, interfacial adhesion is strong enough to transmit the acting stress between constituents so that no debonding appears during the fracture process, and the contribution of the series branch in the EBM is added to that of the parallel branch. In this case σ_b is a monotonic function of the blend composition. Employing the universal formula provided by the percolation theory for the elastic modulus of binary systems, Kolařik and coworkers derived Equation (6a) and Equation (6b) for v_{ij} [55–59]:

$$v_{1p} = \left(\frac{v_1 - v_{1cr}}{1 - v_{1cr}} \right)^q \quad (6a)$$

$$v_{2p} = \left(\frac{v_2 - v_{2cr}}{1 - v_{2cr}} \right)^q \quad (6b)$$

where v_{1cr} or v_{2cr} is the critical volume fraction (the percolation threshold) at which the component 1 or 2 becomes partially continuous and q is the critical exponent. In the marginal zone ($0 < v_1 < v_{1cr}$ or $0 < v_2 < v_{2cr}$), where only one component is continuous, the proposed format cannot be utilized. For approximate calculations, simplified relations can be used for the minority component, i.e. $v_{1p} = 0$ and $v_{1s} = v_1$ (or $v_{2p} = 0$ and $v_{2s} = v_2$). Most ascertained values of q are located in an interval between 1.6 and 2.0, so that $q = 1.8$ can be used as an average value. For the three-dimensional cubic lattice, the percolation threshold $v_{cr} = 0.156$ was determined [51–53].

As tested materials displayed nonlinear viscoelastic behavior, the effect of rising strain on the creep compliance of the samples was accounted for through a modification of the original time-strain superposition principle [60, 61]. Starting from the fact that higher stresses accelerate creep of nonlinear viscoelastic materials, the time – stress superposition principle has been proposed to analyze the isothermal creep behavior of the prepared blends in a wider time scale [62–65]. In other words, creep compliance curves computed at different stress levels (σ) can be shifted along the time scale to construct a creep compliance master curve in a wider time scale at a constant temperature (T_0) and at a reference stress level (σ_0), through the introduction of a stress-dependent shift factor (a_σ), as reported in Equation (7):

$$D(\sigma, \log t) = D(\sigma_0, \log t - \log a_\sigma) \quad (7)$$

Stress-dependent shift factor values can be determined as indicated in Equation (8):

$$\log a_\sigma = -\frac{C_1(\sigma - \sigma_0)}{C_2 + (\sigma - \sigma_0)} \quad (8)$$

where the constants C_1 and C_2, related to the fractional free volume, can be determined *a posteriori* by fitting shift factor data determined at different stress levels.

3. Results and discussion

3.1. Microstructure characterization

It is well known that physical properties of polymer blends are closely related to their phase structure. In STEM micrographs (Figure 2), the dark component corresponds to COC, while the bright one represents PE. From a general point of view, at volume fractions lower than 0.15–0.20 the minority component in immiscible blends forms spherical particles (in studied blends the mean diameter is smaller than 5 μm) uniformly dispersed in the majority component. Considering PE20COC80 sample, it is evident that LLDPE is well dispersed in COC in form of microspheres having a mean diameter of about

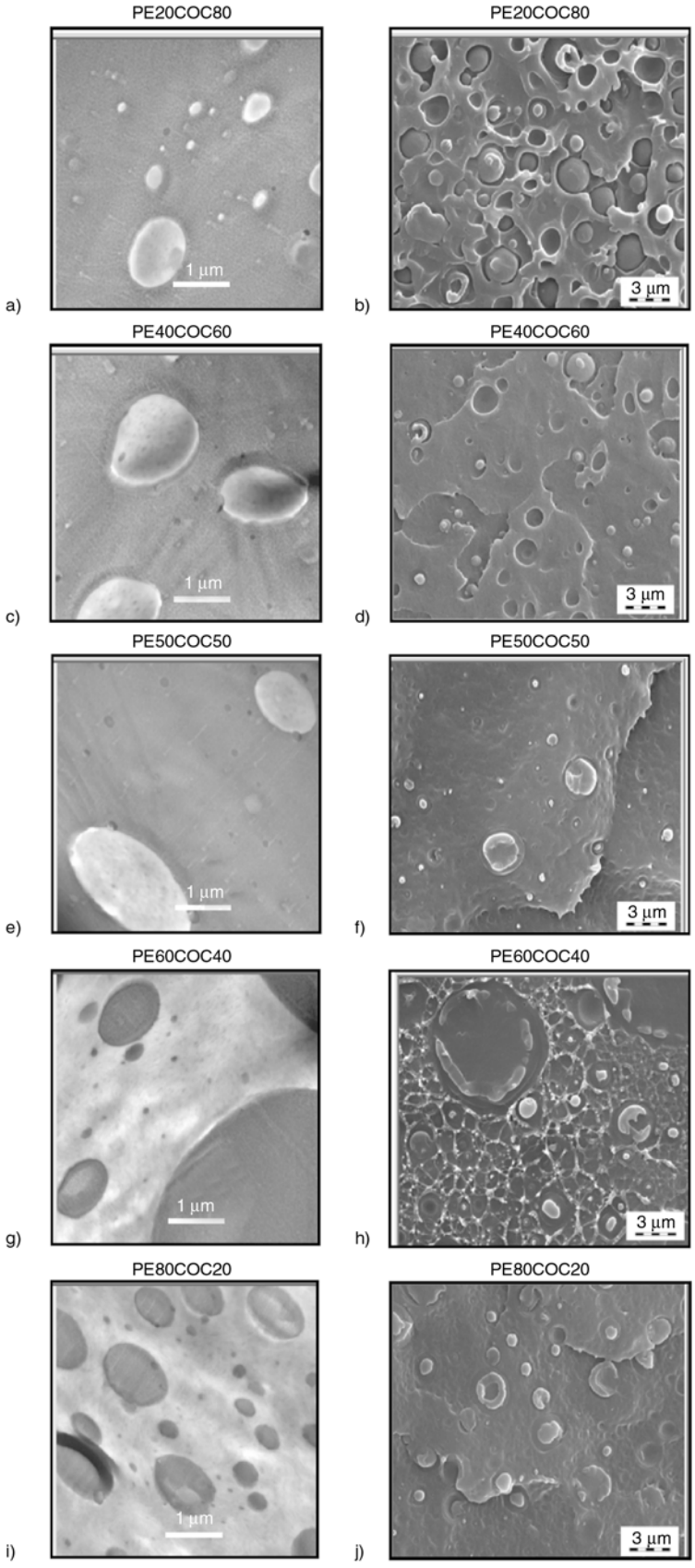

Figure 2. STEM micrographs (left column, pictures a, c, e, g, i) and SEM micrographs (right column, pictures b, d, f, h, j) of the PE/COC blends

0.5 μm. Some debonding, probably produced during the sample microtoming, can be detected around polyethylene particles. The phase inversion takes place in the blends with 40 to 60 wt% of LLDPE. SEM micrographs of PE40COC60, PE50COC50, PE60COC40 and PE80COC20 blends indicate quite high interfacial adhesion between the components, because the fracture frequently propagates through the particles of the minority phase and not along the LLDPE/COC interphase. This supports the hypothesis of a partial component miscibility in the LLDPE/COC blends, as originally advanced by Lamnawar *et al*. [48]. In fact, these authors indicated a partial phase miscibility by means of the Cole–Cole and equivalent plots of the dynamic rheological properties, which was subsequently confirmed by scanning electron microscopy. For the blends with low COC fractions (20 wt%), the microstructure is characterized by small microspheres of COC with a mean diameter of 0.5 μm and narrow size distribution.

3.2. Calorimetric and dynamic mechanical characterizations

Figure 3 reports DSC thermograms of the neat components and corresponding blends while the most relevant thermal properties are summarized in Table 2. As expected, the intensity of the endothermic peak associated to the melting of the crystalline regions of PE increases with the PE fraction in the blends, while the signal associated to the glass transition of the COC component at about 70°C is too weak to be quantitatively analyzed. The melting temperature of PE (Table 2) is not affected by the presence of COC, while the crystallinity degree of PE increases with the COC content in the blends. It can be tentatively hypothesized that a partial co-crystallization of the ethylene segments of COC may take place along with the crystallization of PE.

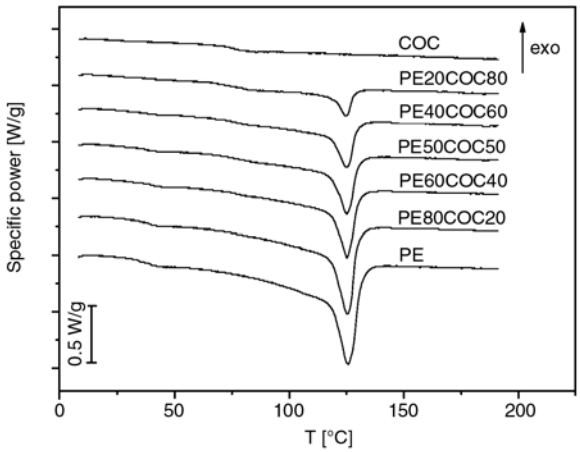

Figure 3. DSC thermograms of the PE/COC blends (first scan)

Table 2. Results obtained from DSC tests of the PE/COC blends

Sample	PE melting temperature [°C]		PE melting enthalpy [J/g]		PE crystallinity [%]	
	1st scan	2nd scan	1st scan	2nd scan	1st scan	2nd scan
PE	125.4	125.3	81.1	87.5	27.6	29.8
PE80COC20	125.5	125.4	73.1	73.9	31.1	31.5
PE60COC40	125.1	125.0	50.4	55.7	28.6	31.6
PE50COC50	125.1	125.1	47.7	47.5	32.5	32.4
PE40COC60	124.6	124.5	39.4	40.7	33.6	34.7
PE20COC80	124.9	124.9	24.3	23.3	41.4	39.7

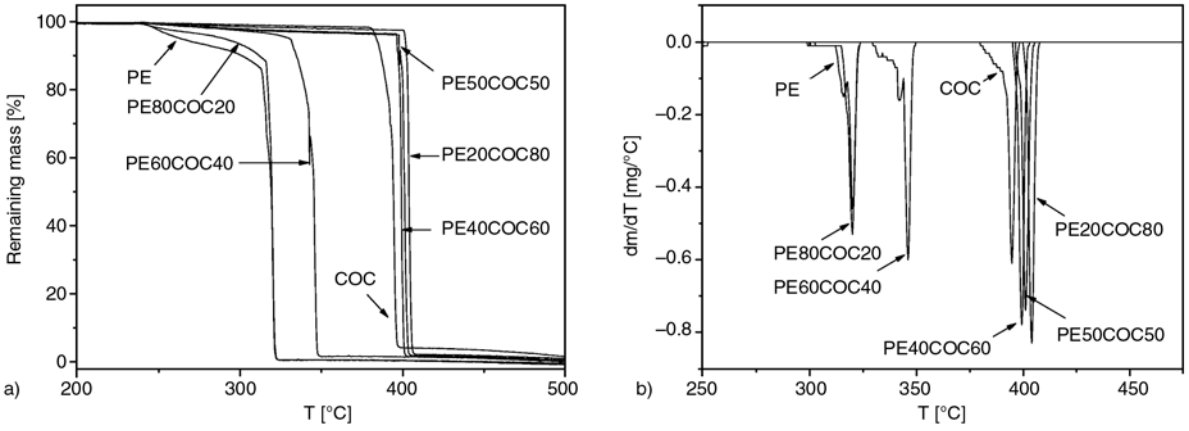

Figure 4. TGA tests of the PE/COC blends. Representative thermogravimetric curves (a) and derivative of the mass loss curves (b) under oxygen atmosphere

However, further investigations would be necessary to explain the observed increase of the LLDPE crystallinity due to the COC addition.

Representative thermogravimetric curves of the prepared blends under oxygen atmosphere are given in Figure 4a, while plots of the derivative of the mass loss curves with temperature are reported in Figure 4b. Although thermogravimetric curve of the PE80COC20 blend is very similar to that of the neat polyethylene, notable enhancements of the thermal degradation resistance, documented by a progressive increase of $T_{2\%}$, $T_{5\%}$ and T_d values, can be detected for the blends with the COC fractions higher than 40 wt% (Figure 5). Comparing thermogravimetric curves under different atmospheres, it is evident that the improvements due to the introduction of COC are more pronounced in oxygen atmosphere. For example, $T_{2\%}$ of the PE20COC80 blend is about 100°C higher than that of the neat PE matrix. As reported in literature [66, 67], it is probable that the presence of a second component with higher thermal stability limits the diffusion of the oxygen through the sample, thus delaying the degradation process of the PE component.

For as concerns DMTA tests, storage modulus (E') of the blends at different temperatures and the glass transition temperature (T_g) of the COC component, evaluated from tanδ peaks, are summarized in Table 3. At temperatures below the glass transition of PE (i.e. about –130°C) E' is slightly affected by the fraction of COC. On the other hand, at 25 and 50°C the increasing fraction of the stiffer COC component leads to a remarkable enhancement of the storage modulus. Another interesting feature is that T_g of the COC component slightly increases with the PE fraction in the blends. The presence of clearly separated glass transitions of the parent components indicates the formation of phase-separated blends (as confirmed by SEM and STEM images). However, the fine micron scale morphology obtained through melt blending may affect individual component transitions, such as crystallization and glass transition, through interphase physical interactions [68]. In fact, Thirta *et al*. [68, 69] showed that the T_g of polystyrene (PS) blended with polypropylene (PP) or PE was increased with decreasing PS percentage in the blends. The enhancement of the T_g of PS in PS/PP and PS/PE blends was attributed to two possible reasons:

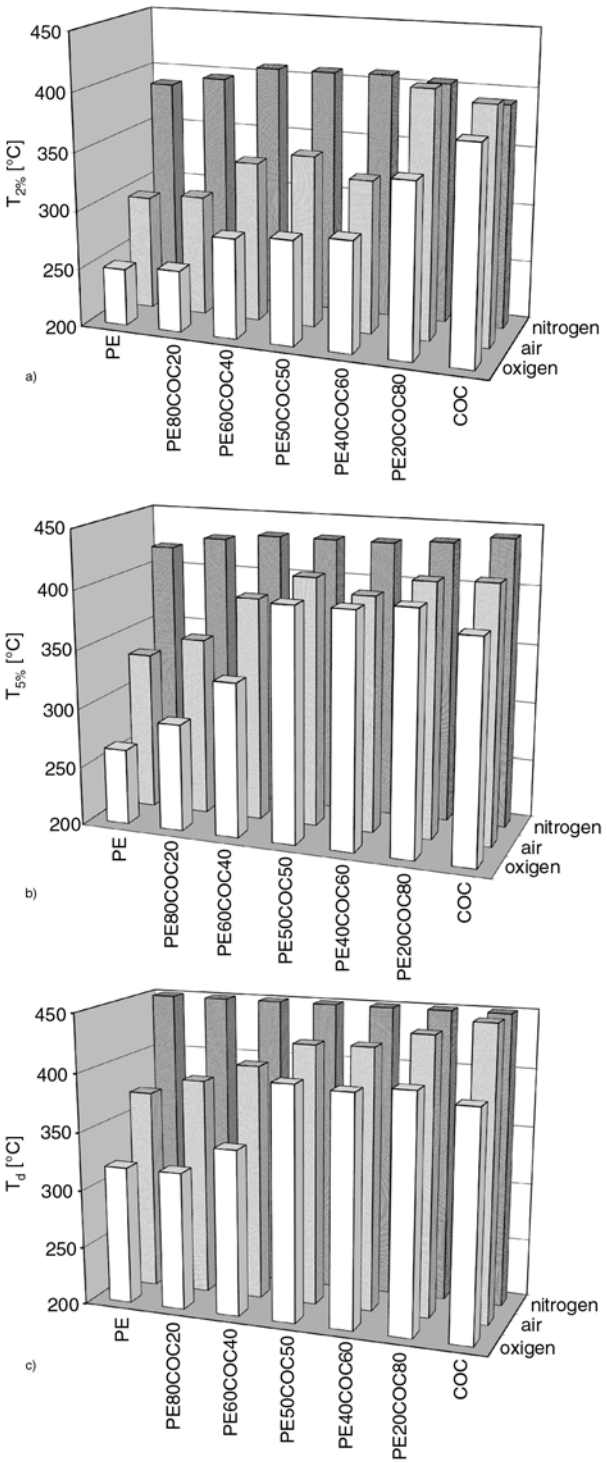

Figure 5. Results of TGA tests of the PE/COC blends under different atmospheres. (a) $T_{2\%}$, (b) $T_{5\%}$, (c) T_d

i) compressive pressure exerted on the amorphous PS domains due to differential shrinkage between the amorphous PS and crystallizing phases, and ii) immobilization of the polymer interfacial layer at the domain boundaries in a process similar to that observed in filled composite systems. In addition we could suppose another possible cause related to

Table 3. Storage modulus (E') at different temperatures and glass transition temperature (T_g) of the COC component from DMTA tests of the PE/COC blends

Sample	E' [MPa]				T_g COC [°C]
	–130°C	25°C	50°C	90°C	
PE	2349	180	64	4	–
PE80COC20	3296	477	243	34	86.5
PE60COC40	3295	671	334	20	86.0
PE50COC50	2988	752	379	14	85.4
PE40COC60	2969	1176	851	15	84.1
PE20COC80	2570	1393	1289	4	83.5
COC	2713	1860	1760	3	82.6

a partial incorporation of the ethylene segments of COC into PE crystalline phase. The remaining amorphous segments of the COC component will thus contain higher percentage of norbornene units, which may account for a lower backbone flexibility and, consequently, a higher T_g.

3.3. Tensile mechanical behaviour

Table 4 reports elastic modulus values of the PE/COC blends from quasi-static tensile tests, while in Figure 6 experimental data are compared with the theoretical prediction provided by the equivalent box model. In agreement with the existing literature [18–20, 56, 57], the introduction of a stiffer component accounts for an increase in the elastic modulus of the blends. The elastic modulus increase in the PE/COC blends is less pronounced for COC fractions smaller than 50%, while for its higher fractions a strong enhancement can be detected due to increasing phase continuity of the COC component in the blends. Also in this case, the data estimated by the EBM approach plausibly fit the experimental data over the whole range of investigated compositions.

In Figure 7a selected stress-strain curves illustrating the quasi-static tensile behaviour of the investigated blends are given. Neat PE and the PE80COC20 blend show an elasto-plastic behaviour with relatively low yield strength (about 10 MPa) and high strain at break (around 1500%).

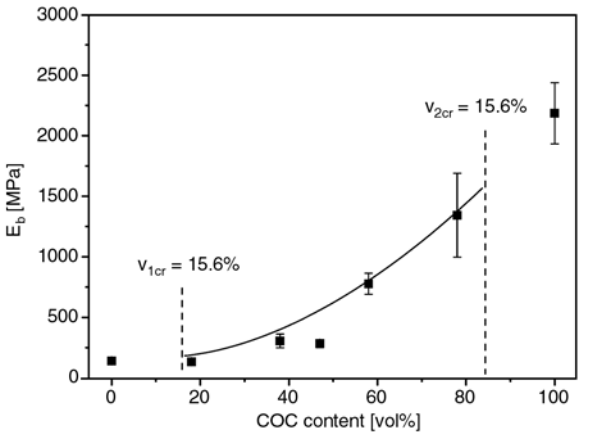

Figure 6. Elastic modulus of the PE/COC blends from quasi-static tensile tests and the theoretical prediction (continuous line) according to the equivalent box model (EBM)

For higher COC fractions, a pronounced reduction of the strain at break accompanied by an increase in yield strength can be observed. Neat COC matrix displays a rather brittle behaviour, typical of amorphous thermoplastics below their glass transition temperature. Interestingly enough, Figure 7b shows that also stress at break can be successfully fitted over the whole range of investigated compositions utilizing the equivalent box model. It is generally believed that the presence of a minimum on the tensile strength vs. blend composition dependence indicates poor interfacial adhesion between the components [50]. Considering Equation (5), the A

Table 4. Results of quasi-static tensile tests of the PE/COC blends, with the determination of the brittleness of the samples (B) according to Equation (9)

Sample	E [MPa]	σ_y [MPa]	σ_b [MPa]	ε_b [%]	10^{10}·B/(%·Pa)
PE	140±121	10.4±0.1	25.2±1.6	1540±64	0.036
PE80COC20	133±12	10.9±0.1	17.7±1.4	1210±92	0.017
PE60COC40	305±56	15.2±0.8	14.1±0.6	20±6	0.745
PE50COC50	283±32	16.6±0.8	15.9±1.2	11±3	1.209
PE40COC60	777±87	25.5±1.6	25.3±1.6	6±1	1.417
PE20COC80	1343±346	35.1±3.6	25.8±1.7	22±8	0.326
COC	2185±252	–	56.2±0.6	4±1	1.344

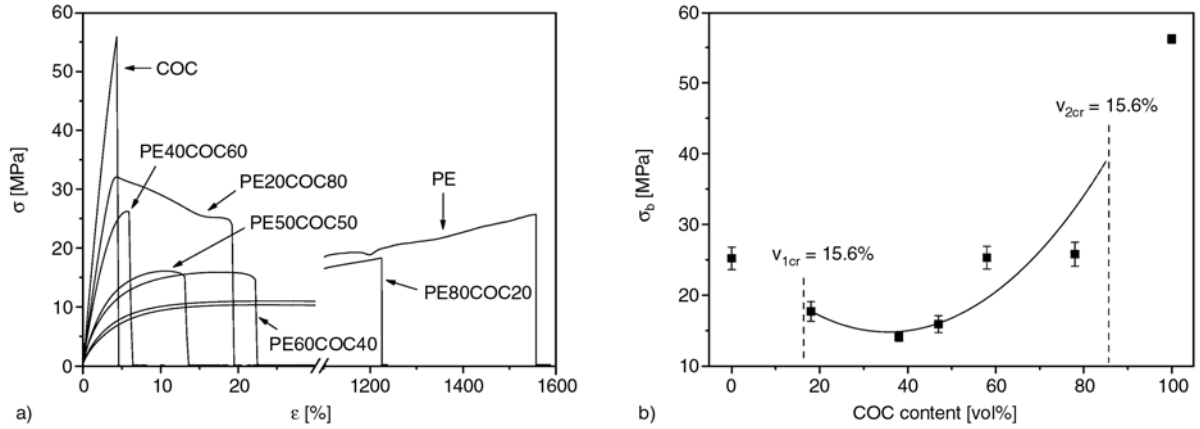

Figure 7. (a) Representative stress-strain curves from quasi-static tensile tests of the PE/COC blends, (b) stress at break values and theoretical prediction (continuous line) according to the equivalent box model (EBM) (A = 0.04)

value, for which the fitting of the stress at break data is performed, is proportional to the quality of the interfacial adhesion between the two phases. In the present case an A value near to zero (0.04) was adopted, which indicates a limited interfacial adhesion between LLDPE and COC. In order to quantitatively describe the embrittlement due to COC introduction, a brittleness (B) parameter was introduced by Brostow *et al*. [70, 71], as reported in Equation (9):

$$B = \frac{1}{\varepsilon_b \cdot E'} \tag{9}$$

where ε_b is the strain at break from quasi-static tensile tests and E' is the storage modulus at 25°C obtained from DMTA tests. As reported in Table 4, it can be seen that B values generally increase with the COC amount, passing from $0.036 \cdot 10^{-10}$ $(\% \cdot Pa)^{-1}$ for the neat LLPDE to $1.34 \cdot 10^{-10}$ $(\% \cdot Pa)^{-1}$ for the neat COC matrix. It is important to underline that the obtained values are very near to that reported in literature references for similar polymeric matrices [70, 71].

Representative force-displacement curves obtained under tensile impact conditions are reported in Figure 8 and the most important results are summarized in Table 5. Increasing fraction of COC in blends progressively increases the maximum load sustained by the samples, but decreases the ductility. For example, specific tensile energy to break (*TEB*) of PE80COC20 sample is about seven times lower than that of neat PE. It can be hypothesized that due to poor interfacial adhesion the COC particles embedded in PE matrix act as crack initiating sites. On the other hand, weakly bonded PE microspheres dispersed in the COC matrix may induce a toughening effect similar to that reported for rubber toughened thermoplastics [23, 24].

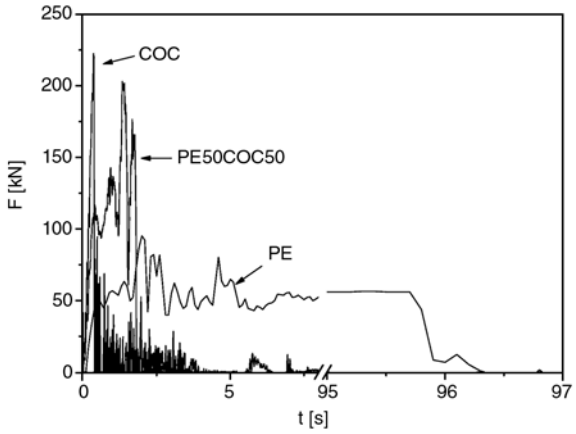

Figure 8. Representative curves of tensile impact tests of the PE/COC blends

Table 5. Results of tensile impact tests of the PE/COC blends

Sample	F_{max} [N]	ε_b [%]	TEB [J/mm²]
PE	99±4	852±126	5.38±0.71
PE80COC20	121±5	105±30	0.76±0.16
PE60COC40	166±12	50±9	0.46±0.08
PE50COC50	206±5	21±2	0.23±0.03
PE40COC60	152±6	11±1	0.12±0.02
PE20COC80	207±6	8±2	0.11±0.04
COC	231±12	4±1	0.05±0.01

3.4. Creep behaviour

Isothermal creep compliance curves of neat PE at 30°C obtained at different stress levels (ranging from 20 to 60% of the yield strength) are reported in Figure 9a, while in Figure 9b isochronous curves

at different times (from 600 to 3600 s) are given. As generally known, an enhancement of the applied stress produces a noticeable increase in the creep compliance of semicrystalline polymers above their glass transition temperature [72]. This nonlinear viscoelastic effects have been associated to a strain-induced increase in the free volume in the amorphous phase of the material [17, 20, 46, 72]. From the analysis of the isochronous curves it is evident that the apparent linearity limit can be registered at strain levels of less than 5%.

Isochronous curves at 3600 s of neat components and of the relative blends as obtained from isothermal creep tests are compared in Figure 10. The introduction of small amounts of COC (up to 20 wt%) in the PE matrix does not substantially affect the creep behaviour of the resulting blend, because the creep-resistant COC component is fully discontinuous (Figure 10). For higher COC fractions, a progressive improvement of the creep resistance can be detected. Analogously, the creep behaviour of PE20COC80 blends is very similar to that of the neat COC matrix. Figure 10b indicates that PE and PE80COC20 samples do not show the apparent linear viscoelastic behaviour even at relatively small strains. In contrast, the creep compliance of COC and PE20COC80 blend seems to be practically stress independent over the whole range of considered stress, which is typical for thermoplastic materials below their glass transition temperature.

The effect of the COC fraction on the stress dependent creep behaviour of the prepared blends can be evaluated on a longer time scale by constructing creep compliance generalized master curves according to the time-stress superposition principle (Equa-

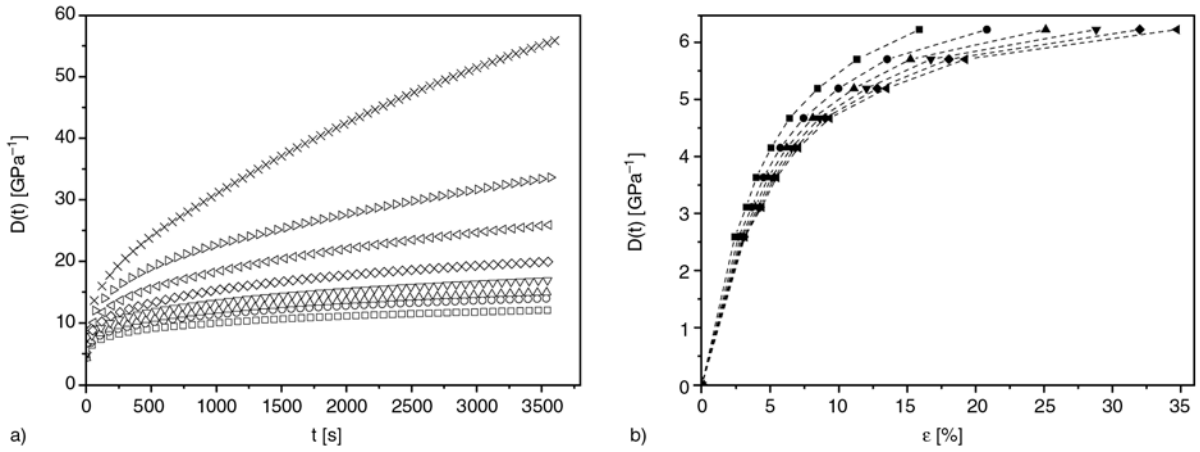

Figure 9. (a) Representative isothermal creep compliance curves of PE sample at various stress levels (T = 30°C), (□) 2.59 MPa, (o) 3.11 MPa, (Δ) 3.63 MPa, (∇) 4.15 MPa, (◊) 4.67 MPa, (◁) 5.19 MPa, (▷) 5.70 MPa, (×) 6.22 MPa. (b) Isochronous curves of PE sample at different times (T = 30°C), (■) 600 s, (●) 1200 s, (▲) 1800 s, (▼) 2400 s, (♦) 3000 s, (◄) 3600 s.

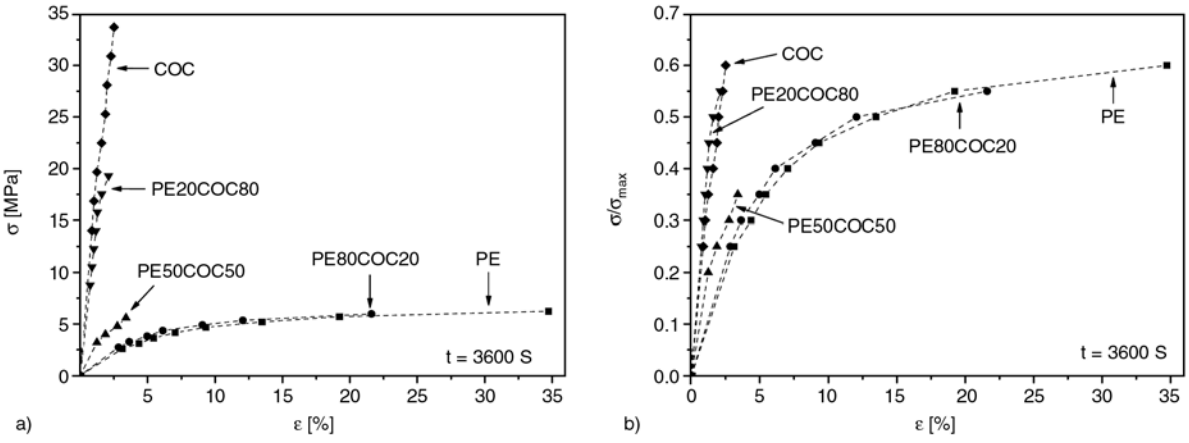

Figure 10. Isochronous curves at 3600 s of the PE/COC blends from isothermal creep tests, (a) stress-strain isochronous curves, (b) relative stress-strain isochronous curves

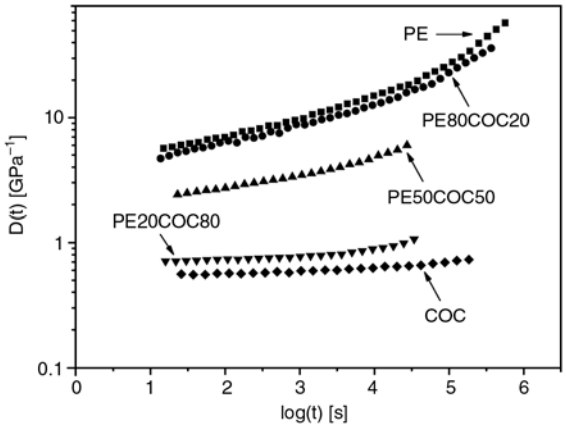

Figure 11. Isothermal creep compliance master curves of the PE/COC blends according to time-stress superposition principle (see Equation (7)), T_0 = 30°C, $\sigma_0 = 20\% \cdot \sigma_{max}$

tion (7)), starting from isothermal creep compliance data of neat components and of the related blends computed at different stress levels. Figure 11 reports creep compliance master curves of the prepared blends at T = 30°C, considering a reference stress equal to the 20% of the yield strength detected in quasi-static tensile tests. Even in this case it can be concluded that the creep behaviour of the neat matrices is not substantially affected by the presence of the second component up to concentrations of 20 wt%. Thus, master curve of neat LLDPE practically superimposes to that of PE80COC20 sample. Only for higher COC weight fractions the creep resistance of the blends is significantly improved by the introduction of a less compliant component.

4. Conclusions

Mechanical properties of LLDPE/COC heterogeneous blends prepared by melt mixing indicate poor interfacial adhesion despite the fact that physical interactions between the components are manifested by (i) increasing crystallinity of LLDPE with rising COC fraction, (ii) increasing T_g of COC with rising LLDPE fraction and (iii) SEM micrographs of fracture surfaces, which show that fracture frequently propagates through the particles and not along the PE/COC interphase. These results were tentatively explained by (i) a partial incorporation of the ethylene segments of COC into the LLDPE crystalline phase and, consequently, (ii) increasing percentage of norbornene units in the remaining COC component undergoing the glass transition. The presence of COC in the blends promoted a relevant increase of the thermal degradation stability, especially when an oxidative atmosphere was considered. Quasi-static tensile tests showed that increasing fraction of COC in the blends accounts for an enhancement of the elastic modulus and a decrease in the strain at break, while tensile strength passes through a minimum. These results are in a good conformity with the model predictions based on the equivalent box model and equations provided by the percolation theory. Moreover, increasing fraction of COC in the blends increased the maximum load sustained by the samples in impact tests, but profoundly decreased the blend ductility. Concurrently, creep measurements demonstrated that a significant reduction of the creep compliance of LLDPE could be achieved only for the COC fractions exceeding 20 wt%.

Acknowledgements

The last author (J. K.) is greatly indebted to the Grant Agency of the Czech Republic for financial support making the participation in this work possible (grant No. 106/09/1348).

References

[1] Folkes M. J., Hope P. S.: Polymer blends and alloys. Chapman and Hall, Cambridge (1993).

[2] Luettmer-Strathmann J., Lipson J. E. G.: Miscibility of polyolefin blends. Macromolecules, **32**, 1093–1102 (1999).
DOI: 10.1021/ma981478e

[3] Olabisi O., Robenson L. M., Shaw M. T.: Polymer-polymer miscibility. Academic Press, New York (1979).

[4] Paul D. R., Bucknall C. B.: Polymer blends. Wiley, New York (1999).

[5] Arndt M., Beulich I.: C_1-symmetric metallocenes for olefin polymerisation, 1. Catalytic performance of [Me_2C(3-^{tert}BuCp)(Flu)]$ZrCl_2$ in ethene/norbornene copolymerisation. Macromolecular Chemistry and Physics, **199**, 1221–1232 (1998).
DOI: 10.1002/(SICI)1521-3935(19980601)199:6<1221::AID-MACP1221>3.0.CO;2-2

[6] Donner M., Fernandes M., Kaminsky W.: Synthesis of copolymers with sterically hindered and polar monomers. Macromolecular Symposia, **236**, 193–202 (2006).
DOI: 10.1002/masy.200690055

[7] Kaminsky W., Hoff M., Derlin S.: Tailored branched polyolefins by metallocene catalysis. Macromolecular Chemistry and Physics, **208**, 1341–1348 (2007).
DOI: 10.1002/macp.200700053

[8] Kaminsky W., Tran P. D., Werner R.: New polymers by copolymerization of ethylene and norbornene with metallocene catalysts. Macromolecular Symposia, **213**, 101–108 (2004).
DOI: 10.1002/masy.200450911

[9] Ruchatz D., Fink G.: Ethene−norbornene copolymerization using homogenous metallocene and half-sandwich catalysts: Kinetics and relationships between catalyst structure and polymer structure. 1. Kinetics of the ethene-norbornene copolymerization using the [(isopropylide ne)(η^5-inden-1-ylidene-η^5-cyclopentadienyl)]zirconium ndichloride/methylaluminoxane catalyst. Macromolecules, **31**, 4669–4673 (1998).
DOI: 10.1021/ma971041r

[10] Ruchatz D., Fink G.: Ethene-norbornene copolymerization using homogenous metallocene and half-sandwich catalysts: Kinetics and relationships between catalyst structure and polymer structure. 2. Comparative study of different metallocene- and half-sandwich/methylaluminoxane catalysts and analysis of the copolymers by ^{13}C nuclear magnetic resonance spectroscopy. Macromolecules, **31**, 4674–4680 (1998).
DOI: 10.1021/ma971042j

[11] Ruchatz D., Fink G.: Ethene-norbornene copolymerization with homogeneous metallocene and half-sandwich catalysts: Kinetics and relationships between catalyst structure and polymer structure. 3. Copolymerization parameters and copolymerization diagrams. Macromolecules, **31**, 4681–4683 (1998).
DOI: 10.1021/ma971043b

[12] Ruchatz D., Fink G.: Ethene-norbornene copolymerization with homogeneous metallocene and half-sandwich catalysts: Kinetics and relationships between catalyst structure and polymer structure. 4. Development of molecular weights. Macromolecules, **31**, 4684–4686 (1998).
DOI: 10.1021/ma9710444

[13] Tritto I., Boggioni L., Jansen J. C., Thorshaug K., Sacchi M. C., Ferro D. R.: Ethylene-norbornene copolymers from metallocene-based catalysts: Microstructure at tetrad level and reactvity ratios. Macromolecules, **35**, 616–623 (2002).
DOI: 10.1021/ma011365m

[14] Forsyth J., Pereña J. M., Benavente R., Pérez E., Tritto I., Boggioni L., Brintzinger H-H.: Influence of the polymer microstructure on the thermal properties of cycloolefin copolymers with high norbornene contents. Macromolecular Chemistry and Physics, **202**, 614–620 (2001).
DOI: 10.1002/1521-3935(20010301)202:5<614::AID-MACP614>3.0.CO;2-C

[15] Forsyth J. F., Scrivani T., Benavente R., Marestin C., Pereña J. M.: Thermal and dynamic mechanical behavior of ethylene/norbornene copolymers with medium norbornene contents. Journal of Applied Polymer Science, **82**, 2159–2165 (2001).
DOI: 10.1002/app.2063

[16] Scrivani T., Benavente R., Pérez E., Pereña J. M.: Stress-strain behaviour, microhardness, and dynamic mechanical properties of a series of ethylene-norbornene copolymers. Macromolecular Chemistry and Physics, **202**, 2547–2553 (2001).
DOI: 10.1002/1521-3935(20010801)202:12<2547::AID-MACP2547>3.0.CO;2-X

[17] Kolařík J., Pegoretti A., Fambri L., Penati A.: Non-linear long-term tensile creep of poly(propylene)/cycloolefin copolymer blends with fibrous structure. Macromolecular Materials and Engineering, **288**, 629–641 (2003).
DOI: 10.1002/mame.200300005

[18] Pegoretti A., Kolařík J., Fambri L., Penati A.: Polypropylene/cycloolefin copolymer blends: Effects of fibrous phase structure on tensile mechanical properties. Polymer, **44**, 3381–3387 (2003).
DOI: 10.1016/S0032-3861(03)00248-9

[19] Kolařík J., Kruliš Z., Šlouf M., Fambri L.: High-density polyethylene/cycloolefin copolymer blends. Part 1: Phase structure, dynamic mechanical, tensile, and impact properties. Polymer Engineering and Science, **45**, 817–826 (2005).
DOI: 10.1002/pen.20337

[20] Kolařík J., Pegoretti A., Fambri L., Penati A.: High-density polyethylene/cycloolefin copolymer blends. Part 2: Nonlinear tensile creep. Polymer Engineering and Science, **46**, 1363–1373 (2006).
DOI: 10.1002/pen.20580

[21] Pimbert S.: Evaluation of the fractionated crystallization of isotactic polypropylene and high density polyethylenes in their blends with cycloolefin copolymers. Macromolecular Symposia, **203**, 277–283 (2003).
DOI: 10.1002/masy.200351330

[22] Šlouf M., Kolařík J., Fambri L.: Phase morphology of PP/COC blends. Journal of Applied Polymer Science, **91**, 253–259 (2004).
DOI: 10.1002/app.13253

[23] Stricker F., Mülhaupt R.: Rubber-toughened cycloolefin copolymers. Die Angewandte Makromolekulare Chemie, **256**, 101–104 (1998).
DOI: 10.1002/(SICI)1522-9505(19980401)256:1<101::AID-APMC101>3.0.CO;2-4

[24] Khanarian G.: Rubber toughened and optically transparent blends of cyclic olefin copolymers. Polymer Engineering and Science, **40**, 2590–2601 (2000).
DOI: 10.1002/pen.11389

[25] Durmuş A., Woo M., Kaşgöz A., Macosko C. W., Tsapatsis M.: Intercalated linear low density polyethylene (LLDPE)/clay nanocomposites prepared with oxidized polyethylene as a new type compatibilizer: Structural, mechanical and barrier properties. European Polymer Journal, **43**, 3737–3749 (2007).
DOI: 10.1016/j.eurpolymj.2007.06.019

[26] Hotta S., Paul D. R.: Nanocomposites formed from linear low density polyethylene and organoclays. Polymer, **45**, 7639–7654 (2004).
DOI: 10.1016/j.polymer.2004.08.059

[27] Kontou E., Niaounakis M.: Thermo-mechanical properties of LLDPE/SiO_2 nanocomposites. Polymer, **47**, 1267–1280 (2006).
DOI: 10.1016/j.polymer.2005.12.039

[28] Lew C. Y., Murphy W. R., McNally G. M.: Preparation and properties of polyolefin-clay nanocomposites. Polymer Engineering and Science, **44**, 1027–1035 (2004).
DOI: 10.1002/pen.20096

[29] Niaounakis M., Kontou E.: Effect of LDPE on the thermomechanical properties of LLDPE-based films. Journal of Polymer Science B: Polymer Physics, **43**, 1712–1727 (2005).
DOI: 10.1002/polb.20473

[30] Bondioli F., Dorigato A., Fabbri P., Messori M., Pegoretti A.: High-density polyethylene reinforced with submicron titania particles. Polymer Engineering and Science, **48**, 448–457 (2008).
DOI: 10.1002/pen.20973

[31] Osman M. A., Rupp J. E. P., Suter U. W.: Tensile properties of polyethylene-layered silicate nanocomposites. Polymer, **46**, 1653–1660 (2005).
DOI: 10.1016/j.polymer.2004.11.112

[32] Handge U. A., Okamoto K., Münstedt H.: Recoverable deformation and morphology after uniaxial elongation of a polystyrene/linear low density polyethylene blend. Rheologica Acta, **46**, 1197–1209 (2007).
DOI: 10.1007/s00397-007-0208-5

[33] Liu Y., Shi Q., Ke Z., Yin L., Yin J.: Reactive compatibilization of LLDPE/PS blends with a new type of Lewis acid as catalyst. Polymer Bulletin, **63**, 411–421 (2009).
DOI: 10.1007/s00289-009-0114-3

[34] Zhang H., Zhang Y., Guo W., Xu D., Wu C.: Thermal properties and morphology of recycled poly(ethylene terephthalate)/maleic anhydride grafted linear low-density polyethylene blends. Journal of Applied Polymer Science, **109**, 3546–3553 (2008).
DOI: 10.1002/app.28456

[35] Zhang Y., Zhang H., Yu Y., Guo W., Wu C.: Recycled poly(ethylene terephthalate)/linear low-density polyethylene blends through physical processing. Journal of Applied Polymer Science, **114**, 1187–1194 (2009).
DOI: 10.1002/app.30030

[36] Ismail H., Ahmad Z., Nordin R., Rashid A. R.: Processibility and miscibility studies of uncompatibilized linear low density polyethylene/poly(vinyl alcohol) blends. Polymer-Plastics Technology and Engineering, **48**, 1191–1197 (2009).
DOI: 10.1080/03602550903147379

[37] Su Z., Li Q., Liu Y., Xu H., Guo W., Wu C.: Phase structure of compatibilized poly(lactic acid)/linear low-density polyethylene blends. Journal of Macromolecular Science B: Physics, **48**, 823–833 (2009).
DOI: 10.1080/00222340902956327

[38] Da Costa H. M., Ramos V. D.: Analysis of thermal properties and rheological behavior of LLDPE/EPDM and LLDPE/EPDM/SRT mixtures. Polymer Testing, **27**, 27–34 (2008).
DOI: 10.1016/j.polymertesting.2007.08.001

[39] Passaglia E., Coiai S., Giordani G., Taburoni E., Fambri L., Pagani V., Penco M.: Modulated crosslinking of polyolefins through radical processes in the melt. Macromolecular Materials and Engineering, **289**, 809–817 (2004).
DOI: 10.1002/mame.200400155

[40] Penco M., Della Sciucca S., Passaglia E., Giordani G., Coiai S., Di Landro L.: Effects of reactive melt mixing on the morphology and thermal behavior of linear low-density polyethylene/rubber blends. Journal of Applied Polymer Science, **109**, 1014–1021 (2008).
DOI: 10.1002/app.28108

[41] Qin J., Ding H., Wang X., Xie M., Yu Z.: Blending LLDPE and ground rubber tires. Polymer-Plastics Technology and Engineering, **47**, 199–202 (2008).
DOI: 10.1080/03602550701816217

[42] Sperling L. H.: Polymeric multicomponent materials: An introduction. Wiley, New York (1997).

[43] Utracki L. A.: Commercial polymer blends. Chapman and Hall, London (1988).

[44] Utracki L. A.: Polymer alloys and blends. Hanser, Munich (1990).

[45] Kopczynska A., Ehrenstein G. W.: Polymeric surfaces and their true surface tension in solids and melts. Journal of Materials Education, **29**, 325–340 (2007).

[46] Kolařík J., Pegoretti A., Fambri L., Penati A.: Prediction of nonlinear long-term tensile creep of heterogeneous blends: Rubber-toughened polypropylene-poly (styrene-*co*-acrylonitrile). Journal of Applied Polymer Science, 88, 641-651 (2003).
DOI: 10.1002/app.11586

[47] Rana D., Lee C. H., Cho K., Lee B. H., Choe S.: Thermal and mechanical properties for binary blends of metallocene polyethylene with conventional polyolefins. Journal of Applied Polymer Science, **69**, 2441–2450 (1998).
DOI: 10.1002/(SICI)1097-4628(19980919)69:12<2441::AID-APP15>3.0.CO;2-#

[48] Lamnawar K., Vion-Loisel F., Maazouz A.: Rheological, morphological, and heat seal properties of linear low density polyethylene and cyclo olefine copolymer (LLDPE/COC) blends. Journal of Applied Polymer Science, **116**, 2015–2022 (2010).
DOI: 10.1002/app.31804

[49] Van Krevelen D. W.: Properties of polymers: Their correlation with chemical structure; Their numerical estimation and prediction from additive group contributions. Elsevier, Amsterdam (1990).

[50] De Gennes P. G.: On a relation between percolation theory and the elasticity of gels. Journal de Physique Lettres, **37**, 1–2 (1976).
DOI: 10.1051/jphyslet:019760037010100

[51] Lyngaae-Jorgensen J., Kuta A., Sondergaard K., Poulsen K. V.: Structure and properties of polymer blends with dual phase continuity. Polymer Networks and Blends, **3**, 1–13 (1993).
[52] Hsu W. Y., Wu S.: Percolation behavior in morphology and modulus of polymer blends. Polymer Engineering and Science, **33**, 293–302 (1993).
DOI: 10.1002/pen.760330509
[53] Sax J., Ottino J. M.: Modeling of transport of small molecules in polymer blends: Application of effective medium theory. Polymer Engineering and Science, **23**, 165–176 (1983).
DOI: 10.1002/pen.760230310
[54] Kolařík J., Lednický F., Locati G. C., Fambri L.: Ultimate properties of polycarbonate blends: Effects of inclusion plastic deformation and of matrix phase continuity. Polymer Engineering and Science, **37**, 128–137 (1997).
DOI: 10.1002/pen.11653
[55] Horák Z., Kolařík J., Šípek M., Hynek V., Večerka F.: Gas permeability and mechanical properties of polystyrene–polypropylene blends. Journal of Applied Polymer Science, **69**, 2615–2623 (1998).
DOI: 10.1002/(SICI)1097-4628(19980926)69:13<2615::AID-APP12>3.0.CO;2-T
[56] Kolařík J.: Simultaneous prediction of the modulus and yield strength of binary polymer blends. Polymer Engineering and Science, **36**, 2518–2524 (1996).
DOI: 10.1002/pen.10650
[57] Kolařík J.: Simultaneous prediction of the modulus, tensile strength and gas permeability of binary polymer blends. European Polymer Journal, **34**, 585–590 (1998).
DOI: 10.1016/S0014-3057(97)00176-6
[58] Kolařík J., Fambri L., Pegoretti A., Penati A.: Prediction of the gas permeability of heterogeneous polymer blends. Polymer Engineering and Science, **40**, 127–131 (2000).
DOI: 10.1002/pen.11145
[59] Kolařík J., Pegoretti A., Fambri L., Penati A.: Polypropylene/elastomer/poly(styrene-*co*-acrylonitrile) blends: Manifestation of the critical volume fraction of SAN in dynamic mechanical, tensile and impact properties. Journal of Polymer Research, **7**, 7–14 (2000).
[60] Findley W. N., Lai J. S. Y.: A modified superposition principle applied to creep of nonlinear viscoelastic material under abrupt changes in state of combined stress. Journal of Rheology, **11**, 361–380 (1967).
DOI: 10.1122/1.549091
[61] Jazouli S., Luo W., Bremand F., Vu-Khanh T.: Application of time–stress equivalence to nonlinear creep of polycarbonate. Polymer Testing, **24**, 463–467 (2005).
DOI: 10.1016/j.polymertesting.2005.01.002
[62] Brostow W.: Time–stress correspondence in viscoelastic materials: An equation for the stress and temperature shift factor. Materials Research Innovations, **3**, 347–351 (2000).
DOI: 10.1007/s100190000054
[63] Luo W., Yang T-Q., An Q.: Time-temperature-stress equivalence and its application to nonlinear viscoelastic materials. Acta Mechanica Solida Sinica, **14**, 195–199 (2001).
[64] Schapery R. A.: On the characterization of nonlinear viscoelastic materials. Polymer Engineering and Science, **9**, 295–310 (1969).
DOI: 10.1002/pen.760090410
[65] Yen S-C., Williamson F. L.: Accelerated characterization of creep response of an off-axis composite material. Composites Science and Technology, **38**, 103–118 (1990).
DOI: 10.1016/0266-3538(90)90001-L
[66] Saikrasun S., Limpisawasdi P., Amornsakchai T.: Effect of LCP and rPET as reinforcing materials on rheology, morphology, and thermal properties of in situ microfibrillar-reinforced elastomer composites. Journal of Applied Polymer Science, **112**, 1897–1908 (2009).
DOI: 10.1002/app.29715
[67] Saikrasun S., Saengsuwan S.: Thermal decomposition kinetics of *in situ* reinforcing composite based on polypropylene and liquid crystalline polymer. Journal of Materials Processing Technology, **209**, 3490–3500 (2009).
DOI: 10.1016/j.jmatprotec.2008.08.005
[68] Thirtha V., Lehman R., Nosker T.: Morphological effects on glass transition behavior in selected immiscible blends of amorphous and semicrystalline polymers. Polymer, **47**, 5392–5401 (2006).
DOI: 10.1016/j.polymer.2006.05.014
[69] Thirtha V. M., Lehman R. L., Nosker T. J.: Glass transition phenomena in melt-processed polystyrene/polypropylene blends. Polymer Engineering and Science, **45**, 1187–1193 (2005).
DOI: 10.1002/pen.20387
[70] Brostow W., Lobland H., Narkis M.: Sliding wear, viscoelasticity, and brittleness of polymers. Journal of Material Research, **21**, 2422–2428 (2006).
DOI: 10.1557/JMR.2006.0300
[71] Brostow W., Lobland H. E. H.: Brittleness of materials: Implications for composites and a relation to impact strength. Journal of Material Science, **45**, 242–250 (2010).
DOI: 10.1007/s10853-009-3926-5
[72] Kolařík J., Pegoretti A.: Non-linear tensile creep of polypropylene: Time-strain superposition and creep prediction. Polymer, **47**, 346–356 (2006).
DOI: 10.1016/j.polymer.2005.11.013

eXPRESS Polymer Letters Vol.5, No.1 (2011) 38–46
Available online at www.expresspolymlett.com
DOI: 10.3144/expresspolymlett.2011.5

Facile synthesis of superhydrophobic TiO_2/polystyrene core-shell microspheres

*Z. M. Chen, S. J. Pan, H. J. Yin, L. L. Zhang, E. C. Ou, Y. Q. Xiong, W. J. Xu**

Institute of Polymer Science and Engineering, College of Chemistry and Chemical Engineering, Hunan University, Changsha 410082, China

Received 7 July 2010; accepted in revised form 12 September 2010

Abstract. In this paper, core-shell TiO_2/polystyrene (TiO_2/PS) microspheres with superhydrophobic properties were prepared via a facile method. Our method needs neither special apparatus nor complicated chemical treatment. The whole process includes two steps: firstly, coupling agent was used to modify TiO_2 by sol-gel method; secondly, fabrication of TiO_2/PS dispersions was carried out via *in-situ* free-radical polymerization strategy. The component and structure of the TiO_2/PS particles were characterized by Fourier transform infrared (FTIR) spectroscopy, thermogravimetric analysis (TGA), field emission scanning electron microscope (FE-SEM) and transmission electron microscopy (TEM). The TiO_2 gel particles with average diameter of 1 μm exhibited irregular spherical shape and obvious aggregation. Compared with the TiO_2 particles, the resulting TiO_2/PS particulates showed regular spherical shape, better dispersion and bigger size. By directly depositing the resulted TiO_2/PS dispersion on a Cu foil, the coating showed superhydrophobic property which was reflected by the contact angle (CA) of water on the surface with high water adhesion. The apparent CA of water is 153.5±1.5°, suggesting that this composite possesses well superhydrophobicity.

Keywords: *adhesion, TiO_2/PS particles, sol-gel method, in-situ free-radical polymerization, superhydrophobicity*

1. Introduction

Recently, organic/inorganic composites have been received great interest due to their unique properties and possibility for numerous applications in modern technology [1–3], such as electroplating [4], biotechnology [5] and electrochemistry [6]. The core-shell sphere is one of the most attractive composite structure because of its amazing functions originating from the different composition of the core and shell materials. Currently a lot of methods are available to prepare organic-inorganic hybrid particles with core-shell structure, such as subsequent polymerization [7], emulsion polymerization [8], layer-by-layer (LBL) method [9] and sol-gel method [10]. Among these methods, sol-gel process is undoubtedly one of the simplest and the cheapest techniques for the fabrication of materials starting from a chemical solution that reacts to produce colloidal particles.

In recent years, superhydrophobic surfaces, with a water CA greater than 150°, have received much attention not only for their significance to fundamental research but also for their important applications in fields ranging from self-cleaning materials to microfluidic devices [11, 12]. There exists two kinds of extremely superhydrophobic cases in nature, that is, 'sliding' superhydrophobic lotus leaves with ultralow water sliding resistance and 'sticky' superhydrophobic gecko feet with high adhesive force. Generally, micrometer or nanometer order rough surfaces with low-surface-energy materials are the keys to obtain superhydrophobic surfaces [13]. The materials having low surface energy used to make the superhydrophobic surfaces

*Corresponding author, e-mail: weijianxu59@gmail.com

are fluorocarbon, silicones, organic materials (polyethylene, polystyrene, etc.) [14], and inorganic materials (ZnO and TiO_2) [15]. There are many approaches to create rough surfaces, such as layer-by-layer and colloidal assembly [16, 17], laser/plasma/chemical etching [18–20], sol-gel processing [21–26], etc. Unfortunately, in many cases, the reported approaches employ either expensive materials, such as carbon nanotubes [27] and semi- or perfluorinated materials [28, 29], or multistep processes [23], thereby the applications in large-scale superhydrophobic surfaces are greatly hampered.

In our laboratory, click chemistry has been used to prepare cactus-like superhydrophobic surfaces with the water CAs greater than 150° [30]. In this paper, we choose TiO_2 and styrene as raw materials, which are of low-surface-energy. Because of TiO_2 gels are inorganic materials, but styrene is an organic material, therefore, the compatibility of them is not very good. 3-(trimethoxysilyl)propylmethacrylate (MPS) is indeed a good coupling agent to modify inorganic particles. Furthermore, the end group of MPS is C=C, when MPS hydrolyzed and grafted to TiO_2 gels, the C=C group can be reacted with styrene through *in-situ* polymerization. Firstly, MPS-TiO_2 gels are obtained via sol-gel method. Afterwards, TiO_2/PS dispersions were fabricated via *in-situ* free-radical polymerization. Finally, TiO_2/PS core-shell composites with superhydrophobic properties were prepared. By directly depositing the dispersion onto the substrate, a superhydrophobic (CA = 153.5±1.5°) and adhesive surface is obtained. Our strategy possesses various advantages: (1) the TiO_2/PS composites present superhydrophobic properties with high water adhesion, which have many potential applications, such as no loss microdroplet transfer, trace-liquid reactors, biochemical separation and *in-situ* detection [12, 31, 32]; (2) the raw materials of TiO_2 and styrene are pretty cheap, making the whole reaction cost-effective; (3) the whole reaction involves only two steps, which makes the synthetic process more facile, therefore, it is possible to introduce it into industry applications; (4) the as-prepared hybrids show excellent chemical and optical stability for there is no change of the water CAs of the coatings when exposing to UV light. It is expected that the facile and scalable synthesis of such robust uniform TiO_2/PS hybrids would pave the way for applying materials with superhydrophobic properties in practical fields.

2. Experimental

2.1. Materials

The coupling agent, 3-(trimethoxysilyl)propylmethacrylate (MPS), was received from Qufu Wanda Chemical Co., Ltd (Shandong, China). Ammonia (25–28 wt%), ethanol, 2,2-azobis(isobutyronitrile) (AIBN), N,N′-dimethylformamide (DMF) and styrene monomer were commercially available from Tianjin Damao Chemical Reagent Company (Tianjin, China). 2,2-azobis(isobutyronitrile) (AIBN) was recrystallized from tetrahydrofuran before use. The styrene monomer was distilled under reduced pressure to remove the inhibitor before polymerization, which was also received from Tianjin Damao Chemical Reagent Company (Tianjin, China). Tetrabutyl titanate (TBT) as the titania source was purchased from China Medicine Group Shanghai Chemical Reagent Company (Shanghai, China).

2.2. Synthesis of MPS-TiO_2 gels

Typically, MPS-grafted colloidal titanium gels were fabricated by the following steps: firstly, TBT (10 g) and MPS (0.73 g) in DMF ([TBT]:[MPS] = 10:1 mol/mol) were mixed in a round-bottom flask followed by stirring the mixture for 4 h until it was homogeneous. Then, the reaction of the mixture stirred at 60°C for 5 h after adding deionized water and little hydrochloric acid solution (36 wt%) ([TBT]:[H_2O]:[DMF] = 1:6:4 mol/mol). Finally, the MPS-grafted colloidal titanium suspensions were obtained, which was then filtered and washed by DMF, and finally the product was dried in vacuum.

2.3. Synthesis of TiO_2/PS microspheres

Subsequently, the TiO_2/PS composites were prepared via *in-situ* free-radical polymerization. The method for synthesis of TiO_2/PS microparticles is described briefly as follows: styrene monomer (20 g), AIBN (0.09 g), and DMF (50 ml) containing 0.2 g of MPS-grafted titanium gels were mixed in a round-bottom flask at room temperature for 30 min. The mixtures were then reacted at 68°C for 5 h under a nitrogen-protected atmosphere. Figure 1 shows the schematic synthesis route for TiO_2/PS microspheres. The fabrication of PS spheres is the

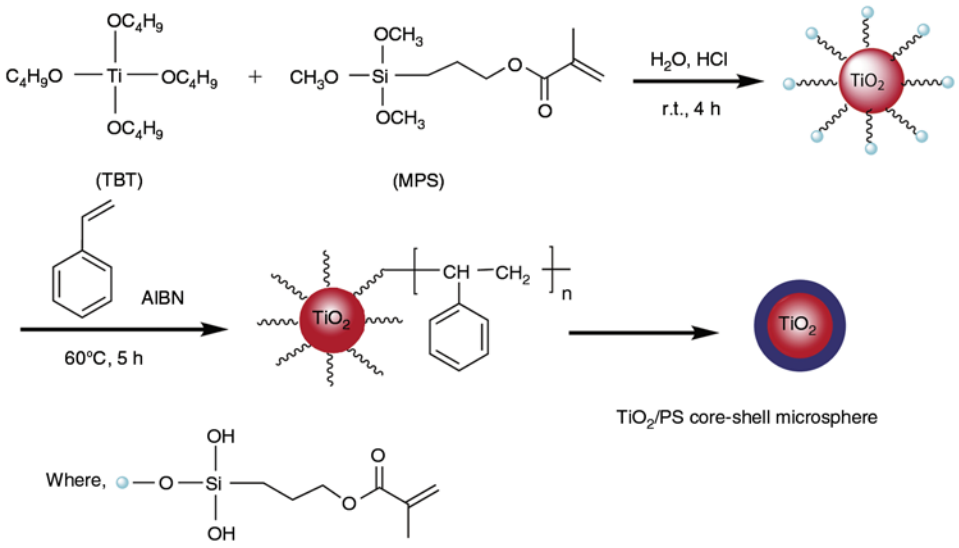

Figure 1. Synthesis route of TiO_2/PS core-shell materials from MPS modified TBT

same as the procedure of fabricating TiO_2/PS under the similar conditions without the addition of MPS-grafted titanium gels.

2.4. Preparation of superhydrophobic coatings

Copper foils (20 mm×10 mm×0.1 mm) were mechanically polished with a series of emery papers of different grit size (800, 2000) followed by rinsing in deionized water; they were ultrasonically cleaned in acetone and ethanol for 5 min, respectively. Then the as-prepared TiO_2/PS dispersions were coated on a clean copper foil and dried at room temperature for one day.

2.5. Characterization

Fourier transform infrared spectrometry (FTIR) was performed on a WQF-200 instrument (Rayleigh, Sci-Tek, Olney, UK) using conventional KBr pellets. Thermogravimetric analysis (TGA) was performed on a Netzsch STA409PC instrument (Netzsch, Selb, Germany) under a flowing argon atmosphere from 30 to 700°C at a scan rate of 10°C/min. Scanning electron microscope and energy dispersive X-ray spectra (SEM/EDX, JEOL, JSM-6700F) were used for the morphological and compositional analysis of the TiO_2/PS particles which was prepared on the substrate of copper foil. Transmission electron microscopy (TEM) images of the composites were obtained at 80 kV with a TEM-H800 (JEOL, Japan). The images of the air-solid-liquid interface were observed by an SONY microscope. The static water contact angles were measured with deionized water (4 μl) on a contact angle goniometer (JC2001) instrument at room temperature (about 28°C). The contact angles were measured at three different points for each sample surface, and the average values were reported here.

3. Results and discussion

3.1. Fabrication of TiO_2/PS microspheres

Figure 2 shows the FTIR spectrum of pristine MPS (a), MPS-TiO_2 particles (b), and TiO_2/PS microspheres (c). In Figure 2b corresponding to the TiO_2-MPS sample, the characteristic absorptions (cm^{-1}) of 2973–2928 (υ_{C-H}) and 1708 ($\upsilon_{C=O}$) for MPS are observed, which indicates that a few MPS molecules have been grafted on the TiO_2 particles suc-

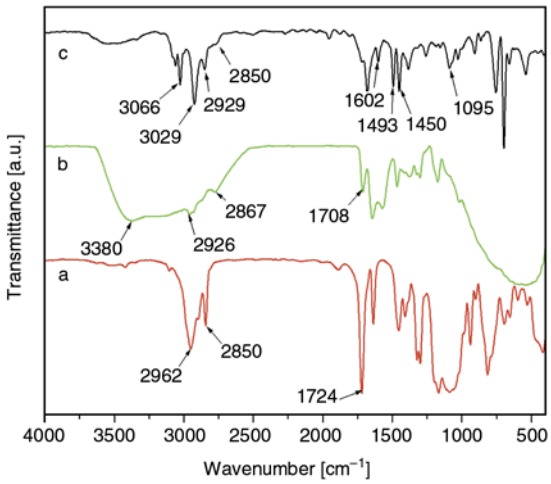

Figure 2. FTIR spectra of (a) pristine MPS, (b) MPS-TiO_2 and (c) TiO_2/PS composites

cessfully. The shift of the C=O vibration band from 1724 to 1708 cm^{-1} is due to the formation of the hydrogen bond between the carbonyl group from MPS and the hydroxyl groups on the surface of TiO_2. A similar phenomenon appeared in the previous spectra as well [33]. From Figure 2, it also displays the typical titanium broad absorption bands at about 450–800 cm^{-1} (Figure 2b). The typical PS absorption bands at 1450, 1493, 1602, 2929, and 3029 cm^{-1} are clearly seen in the spectrum of TiO_2/PS sol hybrids (Figure 2c).

The relative amounts of grafted MPS on TiO_2 and PS on MPS-TiO_2 were determined by TGA through the thermal decomposition of MPS and PS under argon atmosphere. As shown in Figure 3, for the MPS-TiO_2 particles, there are three main temperature regions of weight loss. The weight loss below 300°C can be attributed to the evaporation of physical absorbed water and residual solvent in the samples; the weight loss in the temperature region of 300–460°C can be resulted from the decomposition of MPS; the weight loss in the temperature beyond 460°C can be assigned to the decomposition of titania-bonded groups such as –OH [34]. For the TiO_2/PS core-shell particles, the decomposition temperature region of PS is observed at 350–460°C. According to the results, we can conclude that around 67% of residual for MPS-TiO_2 particles is left and around 19.9% for TiO_2/PS core-shell particulates. It is further confirmed that PS have been grafted to MPS-TiO_2 particles successfully, in accordance with the results of FT-IR.

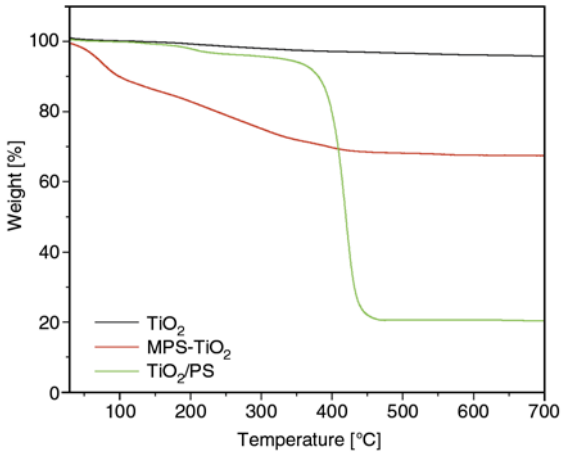

Figure 3. TGA curves of TiO_2, MPS-TiO_2 and TiO_2/PS core-shell particles

3.2. Surface morphology

Figure 4 shows a typical SEM image of PS (a), MPS-TiO_2 (b) and TiO_2/PS (c). From the SEM image of PS (Figure 4a), we can discover that the surface of the spheres is slippery, there is no hierarchical structure presented. For TiO_2 microspheres (Figure 4b), it can be found that the surface of MPS-TiO_2 microspheres with mean diameter of about 1 μm are very rough and seriously aggregated. However, the as-prepared TiO_2/PS microspheres are better dispersed and with larger mean diameter compared with MPS-TiO_2 (Figure 4c), originating from the facts that PS has been successfully grafted onto the surface of the as-prepared MPS-TiO_2 particles. In order to confirm the content of PS coating on the surface of MPS-TiO_2, the TiO_2/PS is also detected by the EDX. Figure 5 gives the EDX spectrum of the TiO_2/PS particulates. The element peaks of titanium together with little oxygen are very weak, confirming that MPS-TiO_2 is encapsulated by PS completely. There is a set of strong peaks in the graph, which belongs to carbon element. The peaks of Cu are for the copper foil, the appearance of this element may be the result of using copper foil as substrate to prepare TiO_2/PS coatings. It convincingly indicates that the

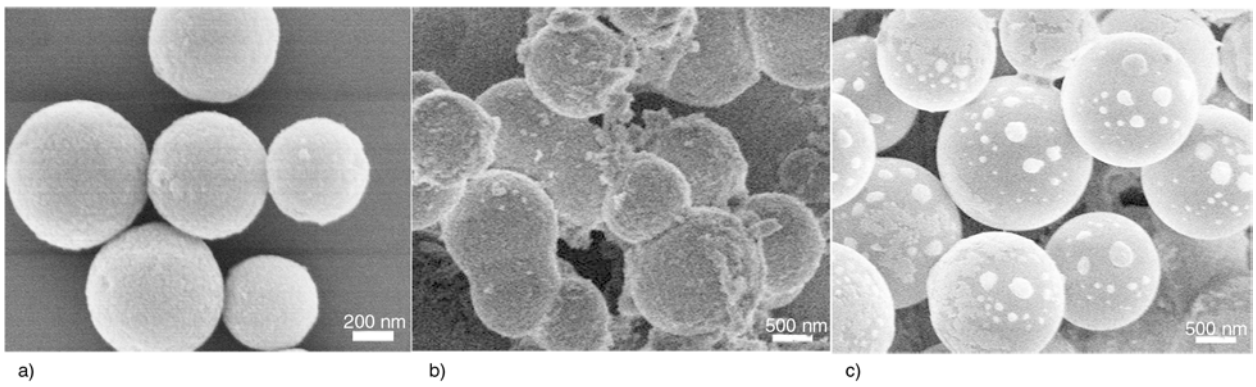

Figure 4. SEM images of PS (a), MPS-TiO_2 (b) and TiO_2/PS (c)

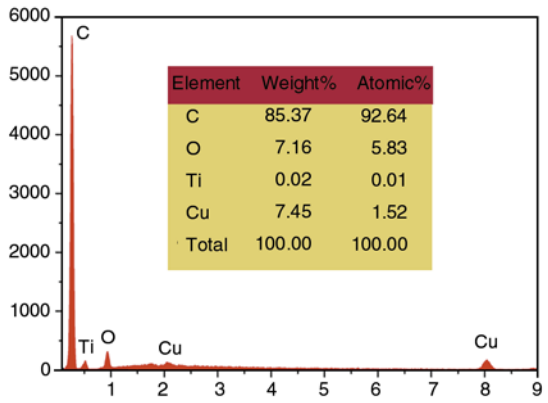

Figure 5. EDX spectrum of TiO_2/PS, the inset table is the elementary analysis for TiO_2/PS microspheres

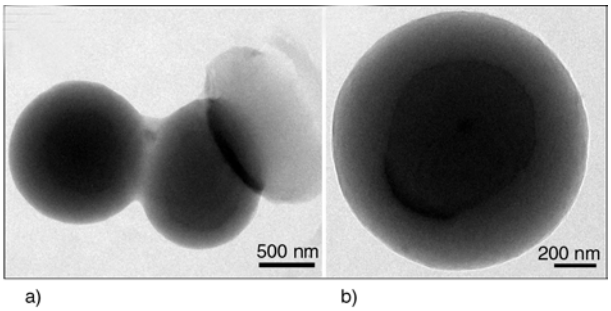

Figure 6. TEM images of TiO_2/PS core-shell particles with low (a) and high magnifications (b)

material coated on the surface of the MPS-TiO_2 is PS. The inset table is the elementary analysis for TiO_2/PS microspheres. It can be seen from the table that the carbon content on the surface of MPS-TiO_2 reaches 85.37 wt%, corresponding to the result of TGA measurement.

Figure 6 shows a typical transmission electron microscope (TEM) image of the as-prepared TiO_2/PS surface. It can be found that a well-defined core-shell structure with TiO_2 particles as core and PS as shell has been formed. The dispersed particles, which are regular in shape, have a distinct layer of PS chains grafted onto the surface of the titanium cores (Figure 6a). The magnification image clearly displays MPS-functionalized titanium cores with the diameter about 600 nm and the PS shell with the thickness about 200 nm (Figure 6b). The result coincides with our suggested mechanism.

3.3. Surface wettability

In the simplest case, the wettability of a solid surface is evaluated by the contact angle given by Young's equation. There exist three different phases when a drop of liquid is on a solid substrate. Generally, there are three surface tensions to consider: solid-liquid (γ_{SL}), liquid-vapor (γ_{LV}), and solid-vapor (γ_{SV}). The relationship between the cosine of the contact angle θ_y that the drop makes with the surface and the three surface tensions is given by Young's equation (Equation (1)):

$$\gamma_{SV} = \gamma_{SL} + \gamma_{LV} \cdot \cos\theta_y \quad (1)$$

Equation (1) can be interpreted as a mechanical force balance for the line of the three-phase contact and is always used under the condition of ideal surface.

As previously shown, surface wettability which depends on the surface energy is subject to Young's equation. However, this equation is not applicable to rough surfaces. The theory explaining such a transition from hydrophobicity to superhydrophobicity occurring on the rough surfaces was proposed by Wenzel [35]. According to Wenzel's modification of Young's equation, the roughness factor r enhances both hydrophilicity and hydrophobicity. The apparent contact angle θ_r is predicted by the following Equation (2):

$$\cos\theta_r = \frac{r \cdot (\gamma_{SV} - \gamma_{SL})}{\gamma_{LV}} = r \cdot \cos\theta \quad (2)$$

Here, r is the roughness of the surface, which is the ratio between the actual surface and its horizontal projection. θ_r and θ are the water CAs of a rough surface and a native flat surface, respectively. It is easy to deduce from Equation (2), when the intrinsic water contact angle is larger than 90° on a flat surface, the hydrophobicity of the surface is enhanced by this effect. In contrast, when the intrinsic water contact angle is smaller than 90° on a flat surface, the hydrophilicity of the surface is enhanced by this effect. Here, θ is 110±2°. Figure 7 shows the water CAs of PS (a), colloid MPS-TiO_2 gels (b) and TiO_2/PS particulates (c), the CAs of them are 94.5±1.5°, 110±2° and 153.5±1.5°, respectively. From Figure 4a we can find that the surface of PS spheres is slippery. When TiO_2 is modified by MPS for the first time, the surface of the TiO_2 is rough which can be seen from Figure 4b, resulting in the increase of θ_r. Then MPS-TiO_2 particles are encapsulated by PS, the surface presents hierarchical structure which also can be found from Figure 4c. The Wenzel mode can well explain why these surfaces are more hydrophobic after modification. In

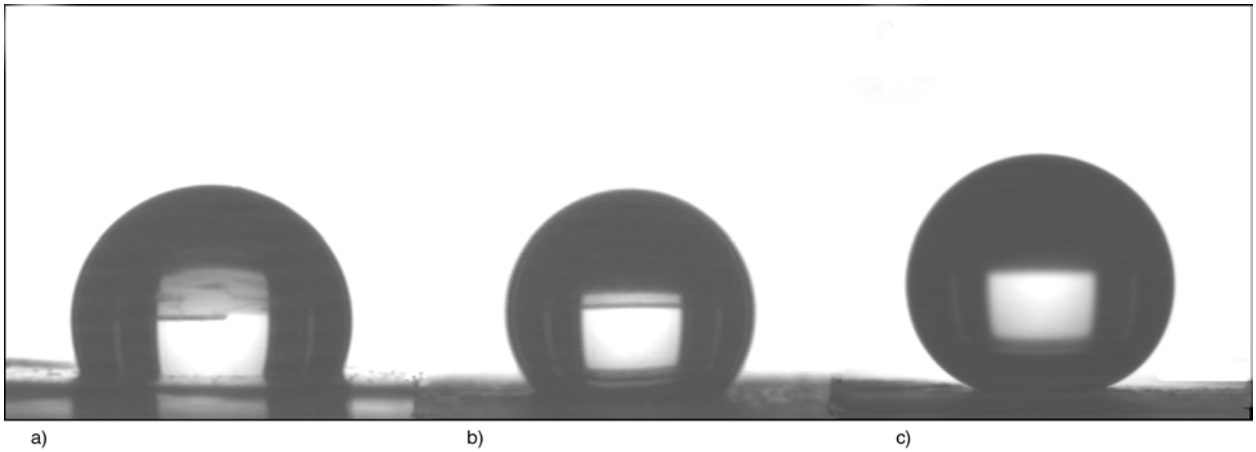

Figure 7. Images for the water CAs of PS (a), MPS-TiO_2 gels (b) and TiO_2/PS particulates (c)

the above cases, the hierarchical TiO_2/PS particulate surface has the biggest water CA after modification, which indicates that this hierarchical structure has the largest roughness. On the other hand, PS is a material of low surface energy, which may affect the hydrophobic property of the coatings. Figure 4c also presents that the 1 μm MPS-TiO_2 gels formed the micrometer structure, on the surface of which there are finer structures at the level of nanometer. The forming of this micro-/nanostructures structure can greatly improve the hydrophobicity of the TiO_2/PS coatings [30, 36].

Interestingly, the droplet deposited on the prepared surface is also featured by high adhesion and high hysteresis of the apparent contact angle. Water droplet on the studied surface keeps a spherical shape even when the surface is turned upside down, as shown in Figure 8. We find that the adhesive ability of the roughness TiO_2/PS-based surface is strong enough to catch a water droplet at a volume of 15 μl even when the copper foil substrate is tilted to 115° (Figure 8b) or turned upside down (Figure 8c), suggesting that the adhesion force between the as-prepared surface and the water droplet is larger than 150 μN. The strong adhesion between water and TiO_2/PS-based nanostructures can be explained mainly by the dispersive adhesion caused by van der Waals' forces, which are largely dependent on the distance between water droplets and surfaces, as confirmed in our experiments. It is significant that when the water droplets are getting close to the surface, the water is repelled and could hardly adhere to the surface until it eventually sticks to the surface. The van der Waals' mechanism of the gecko suggests that the remarkable adhesion property of the gecko's setae is mainly the result of the

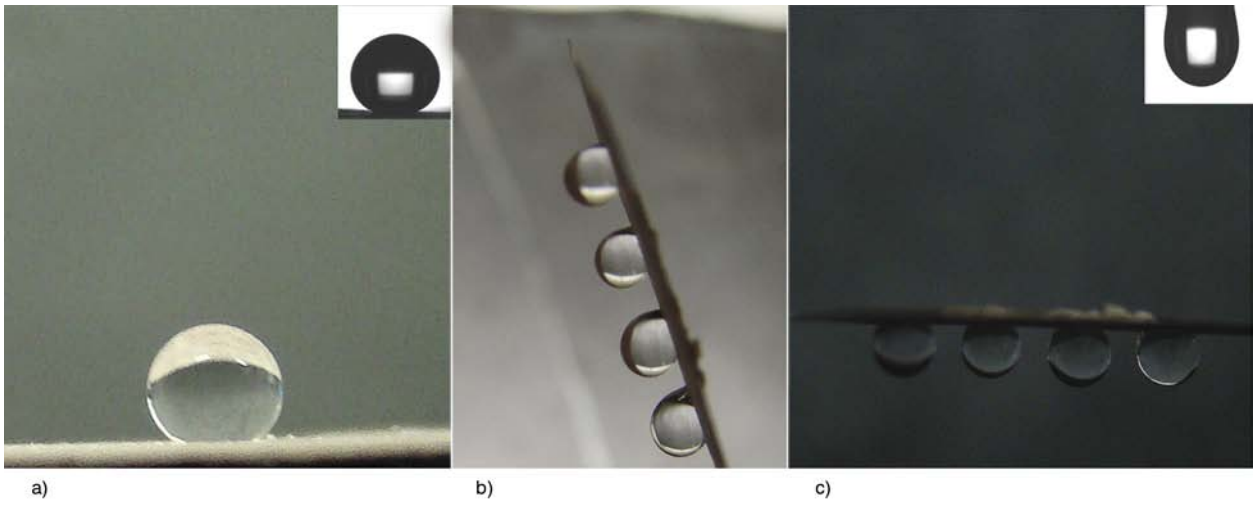

Figure 8. Shapes of water droplets on the as-prepared surface with different tilt angles: (a) 0°, (b) 115°, and (c) 180°. The inset of (a) is the water CA on the as-prepared surface with a value of about 153.5±1.5°. The weights of water droplets employed in (a–c) are about 10, 20, and 20 mg, respectively.

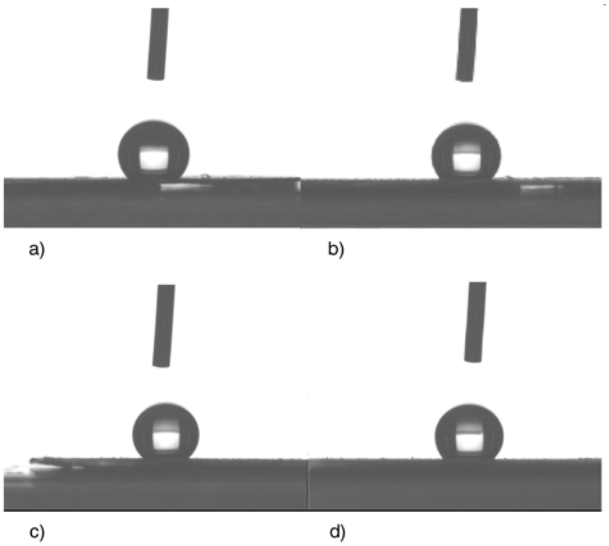

Figure 9. Photographs for the water CAs of TiO_2/PS coatings before and after being immersed in the ethanol (a, b) and exposed to UV light (c, d)

size and shape of its tips and is not strongly affected by chemical properties of the surface [37]. At the same time, according to the capillary mechanism, each micro-orifice produces a miniscule capillary force. Myriad micro-orifices and the wall roughness on the as-prepared surface acting together create formidable adhesion, which is sufficient to endure the weight of the water droplet even when the surface is turned upside down. The stability of the superhydrophobic film is tested by immersing the surfaces into water and ethanol solution overnight, it is found that the surface wetting property of the film did not change. Figure 9a and 9b present the water CAs of the films, they are 153±1° and 151.5±1° before and after being immersed in the ethanol. It also shows excellent optical stability for there is no change of the water CAs of the coatings when exposing to UV light after 30 minutes, which can be deduced from Figure 9, for the water CAs of TiO_2/PS coatings before and after exposing to UV light is 152±1° and 151±1°, respectively.

4. Conclusions

In conclusion, we have prepared a superhydrophobic TiO_2/PS surface with the biggest water contact angle of 153.5±1.5°. The raw materials of TiO_2 and styrene are pretty cheap, and the whole reaction involves two steps, which makes the synthetic process cost-effective and facile. Therefore, it is possible to apply it into industry applications. The as-prepared hybrids present excellent chemical and optical stability as well. Compared with the traditional superhydrophobic surfaces, the as-prepared surface shows a strong adhesive property. This novel wetting behavior is attributed to the distinct microscale surface roughness and heterogeneous surface composition. The highly surface roughness and hydrophobic component contribute to the high static CAs. These results offer us an opportunity to further understand the wettability of solid surface, and also could be used in important industrial applications. We anticipate that the prepared materials have many potential applications, for instance, in no loss microdroplet transfer, trace-liquid reactors, biochemical separation and *in-situ* detection.

Acknowledgements

Authors are thankful to Mr. Chengjun Pan, Mr. Li Zhou, Mr. Sijia Yan and Mr. Guoliang Wu for their kind help in preparing the manuscript. We are indebted to engineer Liu Zhen for TEM imaging.

References

[1] Schneider J. J.: Magnetic core/shell and quantum-confined semiconductor nanoparticles via chimie douce organometallic synthesis. Advanced Materials, **13**, 529–533 (2001).
DOI: 10.1002/1521-4095(200104)13:7<529::AID-ADMA529>3.0.CO;2-X

[2] Zhang K., Zheng L. L., Zhang X. H., Chen X., Yang B.: Silica-PMMA core-shell and hollow nanospheres. Colloids and Surfaces A: Physicochemical and Engineering Aspects, **277**, 145–150 (2006).
DOI: 10.1016/j.colsurfa.2005.11.049

[3] Landfester K., Rothe R., Antonietti M.: Convenient synthesis of fluorinated latexes and core-shell structures by miniemulsion polymerization. Macromolecules, **35**, 1658–1662 (2002).
DOI: 10.1021/ma011608a

[4] Kammona O., Kotti K., Kiparissides C., Celis J. P., Fransaer J.: Synthesis of polymeric and hybrid nanoparticles for electroplating applications. Electrochimica Acta, **54**, 2450–2457 (2009).
DOI: 10.1016/j.electacta.2008.05.017

[5] Chen X., Cui Z. C., Chen Z. M., Zhang K., Lu G., Zhang G., Yang B.: The synthesis and characterizations of monodisperse cross-linked polymer microspheres with carboxyl on the surface. Polymer, **43**, 4147–4152 (2002).
DOI: 10.1016/S0032-3861(02)00262-8

[6] Fu L. J., Liu H., Zhang H. P., Li C., Zhang T., Wu Y. P., Holze R., Wu H. Q.: Synthesis and electrochemical performance of novel core/shell structured nanocomposites. Electrochemistry Communications, **8**, 1–4 (2006).
DOI: 10.1016/j.elecom.2005.10.006

[7] Marinakos S. M., Brousseau L. C., Jones A., Feldheim D. L.: Template synthesis of one-dimensional Au, Au-poly(pyrrole), and poly(pyrrole) nanoparticle arrays. Chemistry of Materials, **10**, 1214–1219 (1998).
DOI: 10.1021/cm980059t

[8] Zhang K., Chen H. T., Chen X., Chen Z. M., Cui Z. C., Yang B.: Monodisperse silica-polymer core-shell microspheres via surface grafting and emulsion polymerization. Macromolecular Materials and Engineering, **288**, 380–385 (2003).
DOI: 10.1002/mame.200390031

[9] Kumaraswamy G., Dibaj A. M., Caruso F.: Photonic materials from self-assembly of 'tolerant' core-shell coated colloids. Langmuir, **18**, 4150–4154 (2002).
DOI: 10.1021/la011772r

[10] Song X. F., Gao L.: Fabrication of hollow hybrid microspheres coated with silica/titania via sol-gel process and enhanced photocatalytic activities. The Journal of Physical Chemistry C, **23**, 8180–8187 (2007).
DOI: 10.1021/jp071142j

[11] Lee K., Lyu S., Lee S., Kim Y. S., Hwang W.: Characteristics and self-cleaning effect of the transparent super-hydrophobic film having nanofibers array structures. Applied Surface Science, **256**, 6729–6735 (2010).
DOI: 10.1016/j.apsusc.2010.04.081

[12] Jin M. H., Feng X. J., Feng L., Sun T. L., Zhai J., Li T. J., Jiang L.: Superhydrophobic aligned polystyrene nanotube films with high adhesive force. Advanced Materials, **17**, 1977–1981 (2005).
DOI: 10.1002/adma.200401726

[13] Bormashenko E., Bormashenko Y., Stein T., Whyman G., Pogreb R., Barkay Z.: Environmental scanning electron microscopy study of the fine structure of the triple line and Cassie-Wenzel wetting transition for sessile drops deposited on rough polymer substrates. Langmuir, **23**, 4378–4382 (2007).
DOI: 10.1021/la0634802

[14] Feng X. J., Feng L., Jin M. H., Zhai J., Jiang L., Zhu D. B.: Reversible super-hydrophobicity to super-hydrophilicity transition of aligned ZnO nanorod films. Journal of the American Chemical Society, **126**, 62–63 (2004).
DOI: 10.1021/ja038636o

[15] Nimittrakoolchai O., Supothina S.: Polymer-based superhydrophobic coating fabricated from polyelectrolyte multilayers of poly(allylamine hydrochloride) and poly(acrylic acid). Macromolecular Symposia, **264**, 73–79 (2008).
DOI: 10.1002/masy.200850412

[16] Lim H. S., Han J. T., Kwak D. H., Jin M. H., Cho K.: Photoreversibly switchable superhydrophobic surface with erasable and rewritable pattern. Journal of the American Chemical Society, **128**, 14458–14459 (2006).
DOI: 10.1021/ja0655901

[17] Amigoni S., de Givenchy E. T., Dufay M., Guittard F.: Covalent layer-by-layer assembled superhydrophobic organic-inorganic hybrid films. Langmuir, **25**, 11073–11077 (2009).
DOI: 10.1021/la901369f

[18] Jin M. H., Feng X. J., Xi J. M., Zhai J., Cho K., Feng L., Jiang L.: Super-hydrophobic PDMS surface with ultra-low adhesive force. Macromolecular Rapid Communications, **26**, 1805–1809 (2005).
DOI: 10.1002/marc.200500458

[19] Chen W., Fadeev A. Y., Hsieh M. C., Öner D., Youngbloo J., McCarthy T. J.: Ultrahydrophobic and ultralyophobic surfaces: Some comments and examples. Langmuir, **15**, 3395–3399 (1999).
DOI: 10.1021/la990074s

[20] Guo Z. G., Fang J., Hao J. C., Liang Y. M., Liu W. M.: A novel approach to stable superhydrophobic surfaces. ChemPhysChem, **7**, 1674–1677 (2006).
DOI: 10.1002/cphc.200600217

[21] Hikita M., Tanaka K., Nakamura T., Kajiyama T., Takahara A.: Super-liquid-repellent surfaces prepared by colloidal silica nanoparticles covered with fluoroalkyl groups. Langmuir, **21**, 7299–7302 (2005).
DOI: 10.1021/la050901r

[22] Tadanaga K., Morinaga J., Matsuda A., Minami T.: Superhydrophobic-superhydrophilic micropatterning on flowerlike alumina coating film by the sol-gel method. Chemistry of Materials, **12**, 590–592 (2000).
DOI: 10.1021/cm990643h

[23] Yang S. Y., Chen S., Tian Y., Feng C., Chen L.: Facile transformation of a native polystyrene (ps) film into a stable superhydrophobic surface via sol-gel process. Chemistry of Materials, **20**, 1233–1235 (2008).
DOI: 10.1021/cm703220r

[24] Peng Y. T., Lo K. F., Juang Y. J.: Constructing a superhydrophobic surface on polydimethylsiloxane via spin coating and vapor-liquid sol-gel process. Langmuir, **26**, 5167–5171 (2010).
DOI: 10.1021/la903646h

[25] Latthe S. S., Imai H., Ganesan V., Rao A. V.: Superhydrophobic silica films by sol-gel co-precursor method. Applied Surface Science, **256**, 217–222 (2009).
DOI: 10.1016/j.apsusc.2009.07.113

[26] Du X., Liu X. M., Chen H. M., He J. H.: Facile fabrication of raspberry-like composite nanoparticles and their application as building blocks for constructing superhydrophilic coatings. The Journal of Physical Chemistry C, **113**, 9063–9070 (2009).
DOI: 10.1021/jp9016344

[27] Alivisatos A. P.: Semiconductor clusters, nanocrystals, and quantum dots. Science, **271**, 933–937 (1996).
DOI: 10.1126/science.271.5251.933

[28] Yang J., Zhang Z. Z., Men X. H., Xu X. H., Zhu X. T.: Reversible conversion of water-droplet mobility from rollable to pinned on a superhydrophobic functionalized carbon nanotube film. Journal of Colloid and Interface Science, **346**, 241–247 (2010).
DOI: 10.1016/j.jcis.2010.02.040

[29] Nakajima A., Fujishima A., Hashimoto K., Watanabe T.: Preparation of transparent superhydrophobic boehmite and silica films by sublimation of aluminum acetylacetonate. Advanced Materials, **11**, 1365–1368 (1999).
DOI: 10.1002/(SICI)1521-4095(199911)11:16<1365::AID-ADMA1365>3.0.CO;2-F

[30] Peng J. Y., Yu P. R., Zeng S. J., Liu X., Chen J. R., Xu W. J.: Application of click chemistry in the fabrication of cactus-like hierarchical particulates for sticky superhydrophobic surfaces. The Journal of Physical Chemistry C, **114**, 5926–5931 (2010).
DOI: 10.1021/jp909430z

[31] Cheng Z. J., Feng L., Jiang L.: Tunable adhesive superhydrophobic surfaces for superparamagnetic microdroplets. Advanced Functional Materials, **18**, 3219–3225 (2008).
DOI: 10.1002/adfm.200800481

[32] Song X. Y., Zhai J., Wang Y. L., Jiang L.: Fabrication of superhydrophobic surfaces by self-assembly and their water-adhesion properties. The Journal of Physical Chemistry C, **109**, 4048–4052 (2005).
DOI: 10.1021/jp045152l

[33] Rong Y., Chen H. Z., Wu G., Wang M.: Preparation and characterization of titanium dioxide nanoparticle/polystyrene composites via radical polymerization. Materials Chemistry and Physics, **91**, 370–374 (2005).
DOI: 10.1016/j.matchemphys.2004.11.042

[34] Peng B., Tang F. Q., Chen D., Ren X. L., Meng X. W., Ren J.: Preparation of PS/TiO_2/UF multilayer core-shell hybrid microspheres with high stability. Journal of Colloid and Interface Science, **329**, 62–66 (2009).
DOI: 10.1016/j.jcis.2008.09.069

[35] Wenzel R. N.: Surface roughness and contact angle. The Journal of Physical Chemistry C, **53**, 1466–1467 (1949).
DOI: 10.1021/j150474a015

[36] Feng J., Huang M. D., Qian X.: Fabrication of polyethylene superhydrophobic surfaces by stretching-controlled micromolding. Macromolecular Materials and Engineering, **294**, 295–300 (2009).
DOI: 10.1002/mame.200800331

[37] Autumn K., Gravish N.: Gecko adhesion: Evolutionary nanotechnology. Philosophical Transactions of the Royal Society A, **366**, 1575–1590 (2008).
DOI: 10.1098/rsta.2007.2173

eXPRESS Polymer Letters Vol.5, No.1 (2011) 47–59
Available online at www.expresspolymlett.com
DOI: 10.3144/expresspolymlett.2011.6

Self-healing of fatigue crack in epoxy materials with epoxy/mercaptan system

Y. C. Yuan[1,3], *M. Z. Rong*[1], *M. Q. Zhang*[2*], *G. C. Yang*[1], *J. Q. Zhao*[3]

[1]Key Laboratory for Polymeric Composite and Functional Materials of Ministry of Education, DSAPM Lab, School of Chemistry and Chemical Engineering, Sun Yat-sen University, Guangzhou 510275, P. R. China
[2]Materials Science Institute, Sun Yat-sen (Zhongshan) University, Guangzhou 510275, P. R. China
[3]College of Materials Science and Engineering, South China University of Technology, Guangzhou 510640, P. R. China

Received 9 July 2010; accepted in revised form 17 September 2010

Abstract. Successful retardation or arrest of fatigue crack is observed in self-healing epoxy composite containing dual encapsulated healant, i.e. two types of microcapsules that respectively include epoxy prepolymer and mercaptan/tertiary amine hardener. Fast curing of the released healing agent from the broken capsules leads to rapid development of its bonding strength and fracture toughness at room temperature. It is found that the effects of microcapsules induced-toughening, hydrodynamic pressure crack tip shielding, polymeric wedge and adhesive bonding of the healing agent are responsible for the extension of fatigue life. Depending on the applied stress intensity range, ΔK_I, and the competition between polymerization kinetics of the healing agent and crack growth rate, the above mechanisms exert different influences on crack retardation. The results might serve as a reference for further improving the performance of the healant system under fatigue circumstances.

Keywords: *smart polymers, fracture and fatigue, self-healing, epoxy*

1. Introduction

Fatigue and fatigue failure are critical for polymeric materials used in structural applications. Most polymeric materials suffer from poor fatigue resistance and would fail at stress levels much lower than the critical stress intensity, K_{IC}. Therefore, imparting self-healing capability to polymers and polymer composites [1–9] should be an effective way to solve the problem. It is hoped that the fatigue cracks can be autonomously eliminated soon after their emergence.

So far, only a few papers of healing of fatigue failure have been reported in the literature for polymeric materials. Daniel and Kim [10] investigated fatigue damage in asphalt by evaluating the changes in the stiffness gain under high temperature during the rest period. Zako and Takano [11] studied crack healing in notched epoxy composite specimens using tensile fatigue tests. The stiffness could almost be fully recovered by application of heat to trigger flow and polymerization of embedded particles of B-staged epoxy resin. Nevertheless, the influence of healing process on neither crack growth rate nor absolute fatigue life was considered in their works [5].

Brown *et al*. [4] firstly established a protocol to extend fatigue life of epoxy using dicyclopentadiene (DCPD). Viscous flow of DCPD in the crack plane retarded crack growth, and its polymerized version further acted as a wedge at the crack tip for artificial crack closure. On the basis of this pilot research, they prepared self-healing epoxy with embedded DCPD-loaded microcapsules and particulate Grubbs' catalyst, which was capable of

*Corresponding author, e-mail: ceszmq@mail.sysu.edu.cn

responding to propagating fatigue cracks by autonomic processes that led to higher endurance limit and life extension, or even complete arrest of cracking [5–8], in addition to the ability to repair the cracks generated by monotonic fracture [9]. The degree of fatigue life extension was found to be dependent on the relative magnitude of mechanical kinetics of crack propagation and chemical kinetics of healing.

In our previous work [12], the epoxy/mercaptan/tertiary amine healing system proved to be able to suppress and rehabilitate fatigue crack in epoxy materials via manual infiltration. Effect of adhesive curing process on fatigue crack propagation was studied in detail. As a continuation of our project, the present paper is focused on self-healing of fatigue crack in epoxy composites containing dual encapsulated healant, i.e. two types of microcapsules that respectively include epoxy prepolymer as the polymerizable component and mercaptan/tertiary amine catalyst as the hardener. The knowledge might provide deeper understanding of the healant for future application.

2. Experimental

2.1. Materials and specimen preparation

The encapsulated healing agent, poly(melamine-formaldehyde)-walled capsules containing epoxy and its hardener, was made according to the methods described elsewhere [13]. The epoxy-loaded microcapsules hold a 1:1 weight ratio mixture of diglycidyl ether of bisphenol A (EPON 828, Hexion Specialty Chemicals, Columbus, USA) and diglycidyl ether of resorcin (J-80, Wuxi Resin Factory of Bluestar New Chemical Materials Co., Ltd., Jiangsu, China), while the hardener-loaded microcapsules include pentaerythritol tetrakis (3-mercaptopropionate) (PMP, Fluka Chemie AG, Buchs, Switzerland) and 2,4,6-tris(dimethylaminomethyl) phenol (DMP-30, Shanghai Medical Group Reagent Co., Shanghai, China). For comparative study, polythiol-loaded microcapsules containing only PMP without amine catalyst were also synthesized. Table 1 lists the specifications of the capsules.

Unfilled epoxy specimens in the form of tapered double cantilever beam (TDCB, with groove length of 55 mm [14, 15]) were cast from the mixture of 100 parts EPON 828 and 12.5 parts diethylenetriamine (DETA, Shanghai Medical Group Reagent Co., Shanghai, China), while the self-healing epoxy specimens of the same configuration were prepared by uniformly mixing 10 wt% epoxy-loaded microcapsules and 10 wt% hardener-loaded microcapsules with the aforesaid mixture of EPON 828 and DETA. Control specimens were fabricated with 10 wt% epoxy-loaded microcapsules and 10 wt% polythiol-loaded microcapsules (that exclude tertiary amine catalyst) to inhibit the healability of the healing agent, while maintaining other characteristics of the capsules. The compounds were degassed, poured into a closed silicone rubber mold and cured for 24 h at room temperature, followed by 48 h at 40°C. Table 2 shows the material properties.

Table 1. Description of the microcapsules

Names	Average diameter [μm]	Density [g/cm^3]	Core substance	
			Ingredient	Content [wt%]
Epoxy-loaded microcapsules	104.3	1.24	EPON 828 J-80	48.7 48.7
Hardener-loaded microcapsules	102.1	1.23	PMP DMP-30	81.2 15.7
Polythiol-loaded microcapsules	101.9	1.25	PMP	97.1

Table 2. Properties of the specimens of cured epoxy and its composites

Properties	Neat epoxy specimens	Control specimens*	Self-healing specimens**
Density [g/cm^3]	1.172	1.182	1.186
K_{IC} [MPa·m$^{1/2}$]	0.587±0.016	0.692±0.023	0.695±0.038
Young's modulus [GPa]	3.7±0.2	3.2±0.3	3.2±0.1
Paris power law exponent, n***	7.12	4.20	–
Paris power law constant, C_0***	0.11	$4.3 \cdot 10^{-4}$	–

*The control specimens contain 10 wt% epoxy-loaded microcapsules and 10 wt% polythiol-loaded microcapsules (excluding tertiary amine catalyst)

**The self-healing specimens contain 10 wt% epoxy-loaded microcapsules and 10 wt% hardener-loaded microcapsules

***n and C_0 were obtained according to equation (3) reported in ref. [17]

2.2. Mechanical testing and characterization

Fatigue crack propagation behavior of the TDCB specimens was studied by a Shimadzu air servo fatigue and endurance testing system ADT-AV02K1S5 (Shimadzu Co., Ltd., Kyoto, Japan) with 2 kN load cell at room temperature (24±1°C). The specimens were pre-cracked (~2.5 mm) with a razor blade while ensuring the pre-crack tip was centered in the groove and immediately cyclically loaded. A triangular waveform of frequency 5 Hz was applied with a stress ratio, R, of 0.1 ($R = K_{min}/K_{max}$, where K_{min} and K_{max} denote the minimum and maximum values of the cyclic stress intensity, respectively). Fatigue cracks were grown within constant mode-I stress intensity factor range, ΔK_I ($\Delta K_I = K_{max} - K_{min}$). Load line crack opening displacement (COD) was measured by a clip gauge. Mode I fatigue cracks were constrained along the centerline of the specimen because of use of side grooves molded in the specimen (Figure 1). The optically measured crack tip position and specimen compliance were plotted against number of cycles. The linear relationship between optically measured crack length and specimen compliance (Figure 2) was used to calculate the crack tip position of the specimens at all times during the experiment [5]. Each loading condition was investigated with continuous cyclic loading to specimen failure and/or with a rest period to allow for healing with stationary crack faces. In the latter case, cyclic loading was stopped after a small amount of crack growth and healing was allowed under different steady-state stress intensities for different times. In the case of manual infiltration, about 0.5 μl of pre-mixed

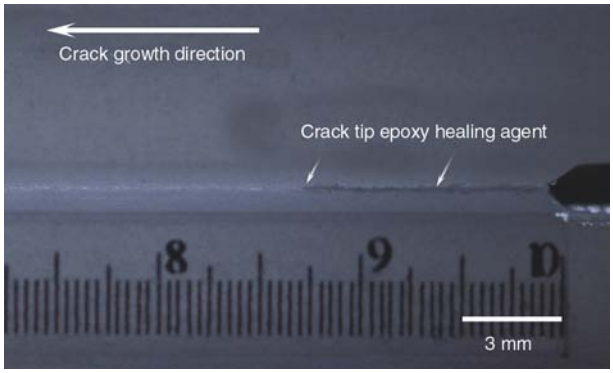

Figure 1. Optical microscopic side view of crack tip during fatigue test of a self-healing specimen. The testing parameters are $\Delta K_I = 0.605$ MPa·m$^{1/2}$, $K_{max} = 0.672$ MPa·m$^{1/2}$, $K_{min} = 0.067$ MPa·m$^{1/2}$, $R = 0.1$ and $f = 5$ Hz.

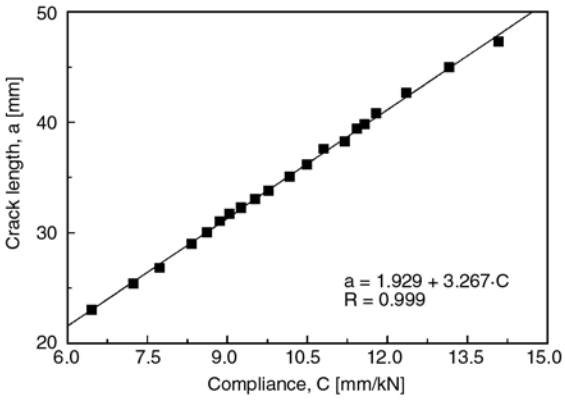

Figure 2. Plot illustrating calculation of continuous crack-tip position of self-healing specimen from compliance data and finite optical measurements. The squares (■) represent compliance values corresponding to the optical data, while the solid line (–) is the linear best fit. The testing parameters are $\Delta K_I = 0.605$ MPa·m$^{1/2}$, $K_{max} = 0.672$ MPa·m$^{1/2}$, $K_{min} = 0.067$ MPa·m$^{1/2}$, $R = 0.1$ and $f = 5$ Hz.

epoxy and polythiol (keeping the stoichiometric ratio while excluding catalyst) was injected into the crack plane of unfilled epoxy specimen with a microsyringe after a crack growth increment of ~8 mm, and fatigue loading was not interrupted throughout the process [12].

The healing efficiency, λ, was defined by fatigue life extension [4], see Equation (1):

$$\lambda = \frac{N_{Healed} - N_{Control}}{N_{Control}} \quad (1)$$

where N_{Healed} and $N_{Control}$ denote the total number of cycles to failure of the self-healing specimen and that of a similar control specimen without healing, respectively. For each test, the result was an average of five specimens.

To evaluate original fracture toughness and development of healing efficiency of epoxy specimens, a natural pre-crack (~2.5 mm) was created on the TDCB specimens by inserting a fresh razor blade and gently tapping into the molded notch starter [15]. Subsequently, the specimen was pin loaded and tested with a Hounsfield 10K-S universal testing machine (Hounsfield Test Equipment Ltd., Surrey, UK) under displacement control using a 3 mm/min displacement rate at room temperature. Specimens were fractured only to the end of the groove. For self-healing specimens, they were unloaded and left to cure for different times at room

temperature. Finally, the healed specimens were tested again following the above procedure.

Micro-Raman measurements were carried out using a Renishaw inVia (Renishaw Co., Ltd., Gloucestershire, UK) spectrometer equipped with a Leica microscope. The Raman spectra were excited by a 785 nm laser line at a resolution of 1 cm^{-1}, and the laser was focused by a 20× objective to a spot size of ~1 μm. Morphological observation and energy dispersive spectroscopy (EDS) analysis were conducted by a Hitachi model S-4800 field emission scanning electron microscope (SEM, manufactured by Hitachi High-Technologies Corporation, Tokyo, Japan). Prior to the experiment, the specimen surface was coated by gold/palladium sputter. Isothermal curing kinetics of the healing agent was studied with a TA differential scanning calorimeter (DSC) Q10 calorimeter (TA Instruments, New Castle, USA) in N_2 at 25°C.

3. Results and discussion

3.1. Self-healing behaviors of the in-situ system

For successful *in-situ* self-healing, the healing agent released into the crack plane must have enough time to polymerize [5]. To facilitate the healing process of the cracks soon after their formation, fast consolidation of the repair chemicals is required.

As shown in Figure 1, small amount of epoxy healing agent in the vicinity of crack tip is squeezed out during the fatigue crack growth. *In-situ* confocal Raman microscopy study of this part of healing agent on the self-healing specimen indicates that epoxide groups quickly react with hydrosulfide groups in the presence of catalyst DMP-30 (Figure 3). About 70% epoxide groups are consumed within 15 min. It means that curing of epoxy healing agent can be completed within very short time.

Accordingly, the development of fracture toughness in self-healing specimens was measured through monotonic fracture tests performed at prescribed times following the initial virgin fracture. It is seen from Figure 4 that after an initial dwell period of about 6 min during which no appreciable healing is measured, the fracture toughness increases rapidly, tapering off after about 30 min. Moreover, time dependence of curing degree of the healing agents measured by differential scanning calorimetry (DSC) shows a similar exponential relationship. The slight difference between the two groups of data should come from (i) mixing uniformity of the healant ingredients under different circumstances, and (ii) the difference in measurement methods [16].

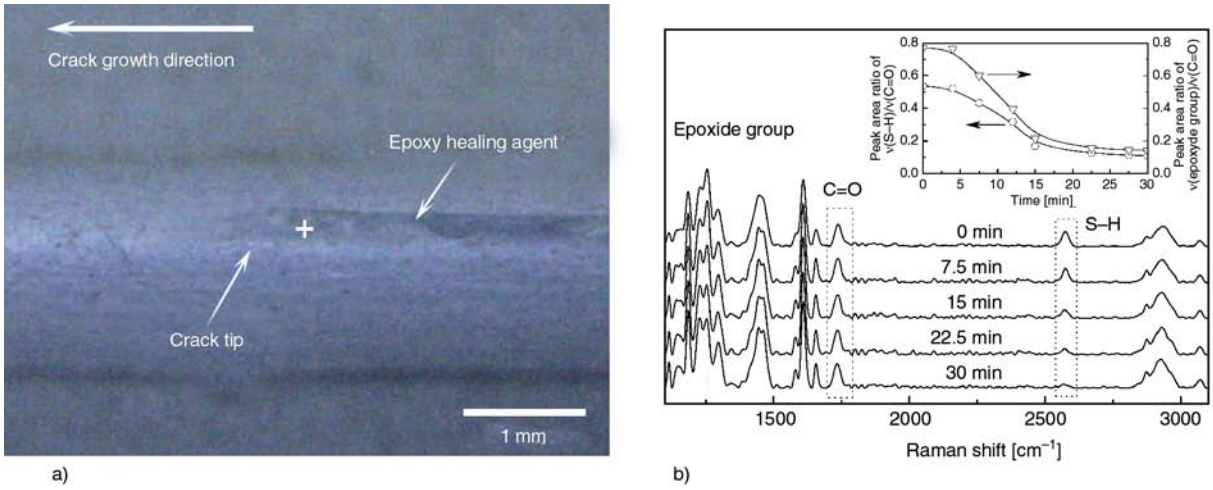

Figure 3. *In-situ* confocal Raman microscopy observation. The photo (a) displays fatigue crack tip in side groove of a self-healing specimen. The figure (b) shows typical Raman spectra collected from the center of the extruded healing agent in the vicinity of crack tip at different times counted from crack stop. The inset summarizes time dependences of the characteristic Raman peak area ratios. Here three peaks are of interests: stretching modes of epoxide group at 1256 cm^{-1}, carbonyl group at 1738 cm^{-1} and hydrosulfide group at 2573 cm^{-1}. Since carbonyl originates from mercaptan, and the reaction between epoxy and mercaptan cannot produce any carbonyl, the peak area of carbonyl group at 1738 cm^{-1} is able to serve as the reference for evaluating the variation in the peak areas of epoxide and hydrosulfide groups with time. This figure provides a live record of the curing reaction of the released healing agent in an authentic specimen. The testing parameters are $\Delta K_I = 0.605$ MPa·$m^{1/2}$, $K_{max} = 0.672$ MPa·$m^{1/2}$, $K_{min} = 0.067$ MPa·$m^{1/2}$, $R = 0.1$ and $f = 5$ Hz.

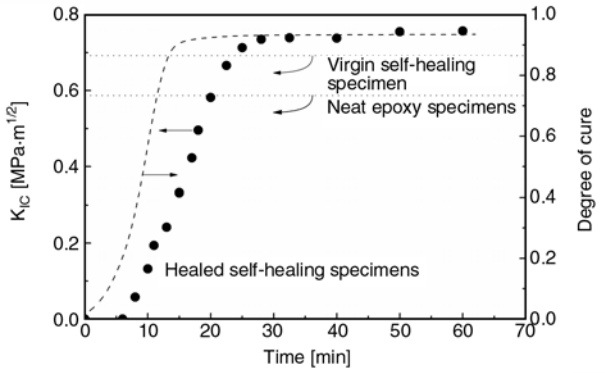

Figure 4. Time dependences of fracture toughness (●) developed in healed self-healing specimen and degree of cure (dash line) of the healing agent. The lower horizontal dotted line represents average K_{IC} of neat epoxy specimens and the upper horizontal dotted line represents that of virgin self-healing specimens. All the fracture toughness values of self-healing specimens were obtained from monotonic fracture tests. The data of degree of cure were estimated from isothermal polymerization of the healing agent conducted in DSC at 25°C [12]. The K_{IC} of virgin self-healing specimen is higher than that of neat epoxy specimen as a result of toughening effect induced by the embedded microcapsules, which will be discussed in sub-section 3.2.

On the whole, it can be considered that the increase in fracture toughness keeps in step with degree of cure of the healing agent. The result well agrees with that reported by Brown *et al*. [5].

Clearly, the above results manifest that healing proceeds quite fast at room temperature, which should satisfy the prerequisite for *in-situ* repairing fatigue crack.

3.2. Effect of microcapsules on fatigue performance of epoxy

Incorporation of healing agent capsules into epoxy would certainly affect the latter's properties. As shown in Table 2 and Figure 4, the presence of 20 wt% microcapsules (i.e. 10 wt% epoxy-loaded capsules and 10 wt% polythiol-loaded capsules or hardener-loaded capsules) has raised the virgin monotonic fracture toughness of epoxy by up to ~18%. The toughening effect is also reflected by a change in fracture morphology from mirror-like of the unfilled epoxy to hackle markings of the capsules filled version (Figure 5). The result coincides with previous report on a similar system, where crack pinning mechanism was believed to take the responsibility [13, 14, 17]. Such an increase of material's toughness would inevitably improve its fatigue performance because of the increased resistance to fatigue crack propagation.

Additionally, under cyclic loading condition, the forces required to squeeze the fluidic healing agent (released from the broken capsules) out of the crack during unloading and to draw the fluid into the crack during loading would shield the crack tip [18]. This hydrodynamic pressure crack tip shielding mechanism can also improve the resistance to fatigue crack propagation. Here in this work, the effect is firstly revealed by manually injecting the mixture of epoxy prepolymer and polythiol at the stoichiometric ratio of 1.2:1 by weight (which is the same as the healing agent formulation except that the amine catalyst is excluded) into the crack plane of neat epoxy specimen without interrupting the

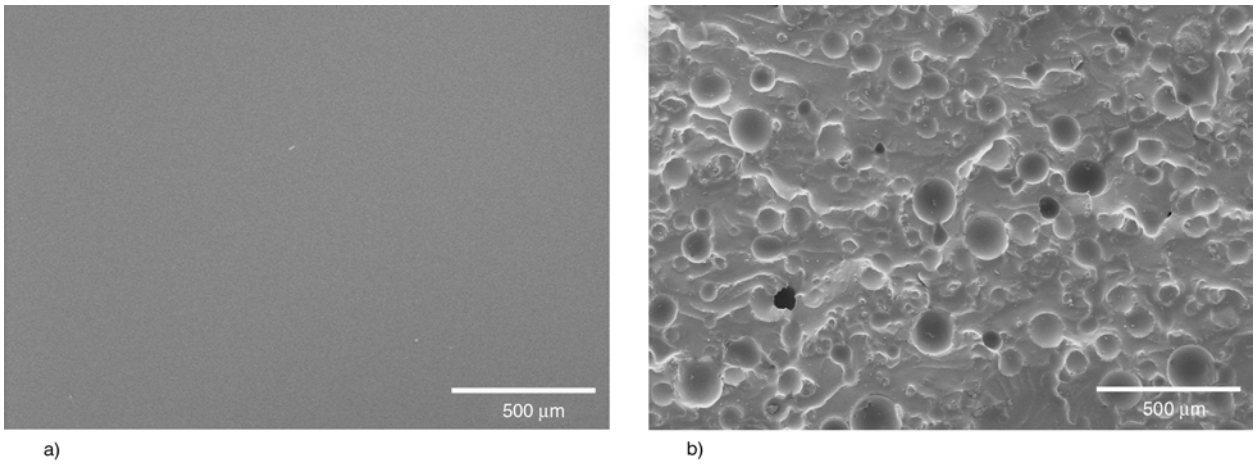

Figure 5. SEM micrographs of fatigue fracture surfaces of (a) neat epoxy specimen and (b) control specimen. The testing parameters are $\Delta K_I = 0.504$ MPa·m$^{1/2}$, $K_{max} = 0.560$ MPa·m$^{1/2}$, $K_{min} = 0.056$ MPa·m$^{1/2}$, $R = 0.1$ and $f = 5$ Hz. Note: The crack propagates from left to right in the images.

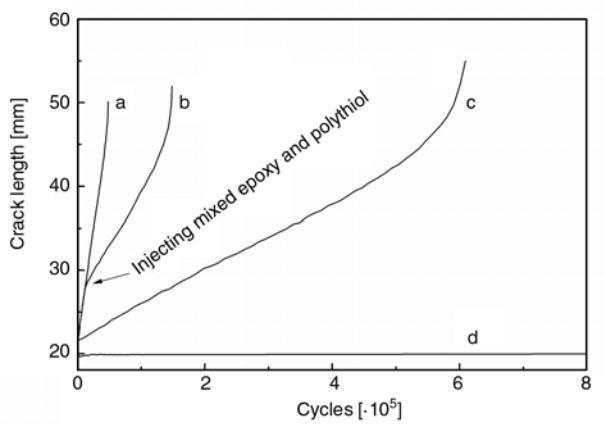

Figure 6. Crack length vs. fatigue cycle of (a) neat epoxy specimen, (b) manual infiltration specimen, (c) control specimen and (d) self-healing specimen. The manual injection specimen was injected by the stoichiometric mixture of epoxy and polythiol excluding the amine catalyst in dynamic infiltration fashion [12]. The testing parameters are $\Delta K_I = 0.504$ MPa·m$^{1/2}$, $K_{max} = 0.560$ MPa·m$^{1/2}$, $K_{min} = 0.056$ MPa·m$^{1/2}$, $R = 0.1$ and $f = 5$ Hz.

fatigue experiment (Figure 6). The infiltrated liquid mixture can be considered to be chemically stable because epoxy-polythiol would hardly react with each other without proper catalysis. As a result, the subsequent crack propagation keeps steadiness on the whole like the case of submerged specimens [19]. Compared to the neat epoxy specimen, the infiltration greatly decreases the crack growth rate from $1.8 \cdot 10^{-3}$ mm/cycle to $4.0 \cdot 10^{-4}$ mm/cycle and increases the fatigue life by ~207% (cf. curves a and b in Figure 6). The results agree with those observed in the case of infiltration of epoxy prepolymer (or the hardener, i.e. mixture of PMP and DMP-30) alone [12]. Secondly, the dependence of crack length on fatigue cycle of control specimen with 10 wt% epoxy-loaded capsules and 10 wt% polythiol-loaded capsules (no tertiary amine catalyst is included) was measured (curve c in Figure 6). The crack growth rate is further reduced to $1.3 \cdot 10^{-4}$ mm/cycle, and the fatigue life extension increases by ~1161% comparing with neat epoxy specimen. It means that both microcapsules induced-toughening and hydrodynamic pressure crack tip shielding mechanisms have taken effect, while the former makes more contribution to retardation of fatigue crack than the latter.

When the healing agent flowing out of the broken microcapsules contain catalyst and could rapidly react, polymeric wedge and adhesive bonding mechanisms [12–14] are involved, which can greatly extend fatigue life of the material (see curve d in Figure 6). More details of this aspect will be discussed in the next section.

3.3. Effect of applied range of cyclic stress intensity

Following the traditional crack closure concept [18, 20–26], it is known that if fatigue crack opening load is purposely increased at the crack tip of self-healing specimens by the aforesaid four mechanisms (i.e. microcapsules induced-toughening, hydrodynamic pressure crack tip shielding, polymeric wedge and adhesive bonding), the effective stress intensity factor range, ΔK_{eff}, would be reduced accordingly, see Equation (2):

$$\Delta K_{eff} = \Delta K_I - \Delta K_{toughening} - \Delta K_{liquid} - \\ - \Delta K_{bonding} - \Delta K_{wedge} \quad (2)$$

where $\Delta K_{toughening}$ denotes the stress intensity due to microcapsules induced increase of matrix ductility, ΔK_{liquid} the crack-opening and crack-closure stress intensity from viscosity resistance of the liquid, $\Delta K_{bonding}$ the stress intensity due to the combined (tensile) stresses in adhesives across the crack faces, and ΔK_{wedge} the crack-closure stress intensity due to the wedge from adhesives gelling and hardening.

Considering that the competition between polymerization kinetics and crack growth would be a major factor affecting successful healing, three levels of applied range of stress intensity were prescribed for the fatigue tests of self-healing specimens hereinafter: two high cycle fatigue cases and one low cycle fatigue case. The high cycle fatigue refers to the fatigue regime of low ΔK_I, relatively slow crack growth rate and longer fatigue life (even infinite life). Low cycle fatigue refers to the fatigue regime where K_{max} approaches K_{IC} and rapid crack growth causes specimen failure after very short time.

For low ΔK_I, chemical kinetics of the healing agent dominates, the crack is fully arrested within short time, and self-healing provides infinite fatigue life extension. In this regime, the specimen's fatigue life exceeds the time for the healing agent to gel and for quasi-static healing efficiency to develop [5]. For example, when $\Delta K_I = 0.504$ MPa·m$^{1/2}$ ($K_{max}/K_{IC} = 0.81$), self-healing specimens were precracked and immediately cyclically loaded. A typi-

cal plot of crack length vs. fatigue cycle is shown by curve d in Figure 6. The initial release of healing agent during precracking firstly retards the crack growth, and leads to certain amount of crack regression (~2 mm). After a few cycles, the crack does not further progress within the time frame of the test (10^7 cycles) and hence is fully arrested. According to Equation (1), the healing efficiency is infinite. This behavior was repeatedly observed for all the five specimens tested. In contrast, the precrack in the control specimen is more rapidly growing at a constant rate (see curve c in Figure 6).

When the self-healing specimen with fully arrested fatigue crack was fractured under static load without precrack, its fracture toughness was found to be 0.963 MPa·m$^{1/2}$, which is much higher than that of virgin self-healing specimen (0.695 MPa·m$^{1/2}$). As shown in Figure 7, the healing agent released during the precrack event has formed a partial polymer wedge at the crack tip. Cohesive failure of the cured healing agent is confirmed by micro-Raman and energy dispersive spectroscopy (EDS) analysis (figure omitted). Obviously uniform tearing traces appear on the fast fracture plane when the healing agent is in the rubbery state (Figure 7b). It implies that stronger adhesion effect is obtained at lower ΔK_I, which favors to arrest fatigue crack. Therefore, adhesive bonding and polymeric wedge shielding mechanisms play an important role to indefinitely extend fatigue life of the material in this regime.

With a further rise in ΔK_I, crack growth rate has to be greatly reduced but the crack cannot be fully arrested. In this regime, the self-healing specimen's fatigue life approaches the time for the healing agent to gel. For example, when ΔK_I = 0.504 MPa·m$^{1/2}$ (K_{max}/K_{IC} = 0.89), the crack growth is retarded at the beginning (refer to curve b in Figure 8) in a way similar to curve d in Figure 6. Following this period of crack arrest, the crack eventually grows past the healed precrack at ~$6 \cdot 10^4$ cycles. The subsequent crack growth behavior is a combination of steady growth and retardation, offering a healing efficiency of about 575%. In the course of fatigue crack propagation, as shown in Figure 9, large quantities of epoxy healing agent were squeezed into thin cakes densely covering the fatigue fracture surface, and some were extruded into tiny balls filling in the concaves left by the broken microcapsules. Besides cohesive failure of the

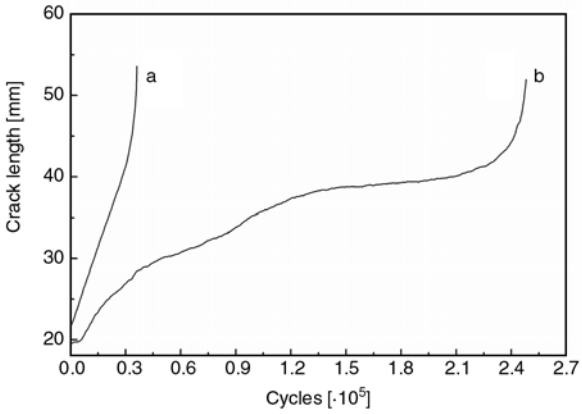

Figure 8. Crack length vs. fatigue cycles of (a) control specimen and (b) self-healing specimen. The testing parameters are ΔK_I = 0.554 MPa·m$^{1/2}$, K_{max} = 0.616 MPa·m$^{1/2}$, K_{min} = 0.062 MPa·m$^{1/2}$, R = 0.1 and f = 5 Hz.

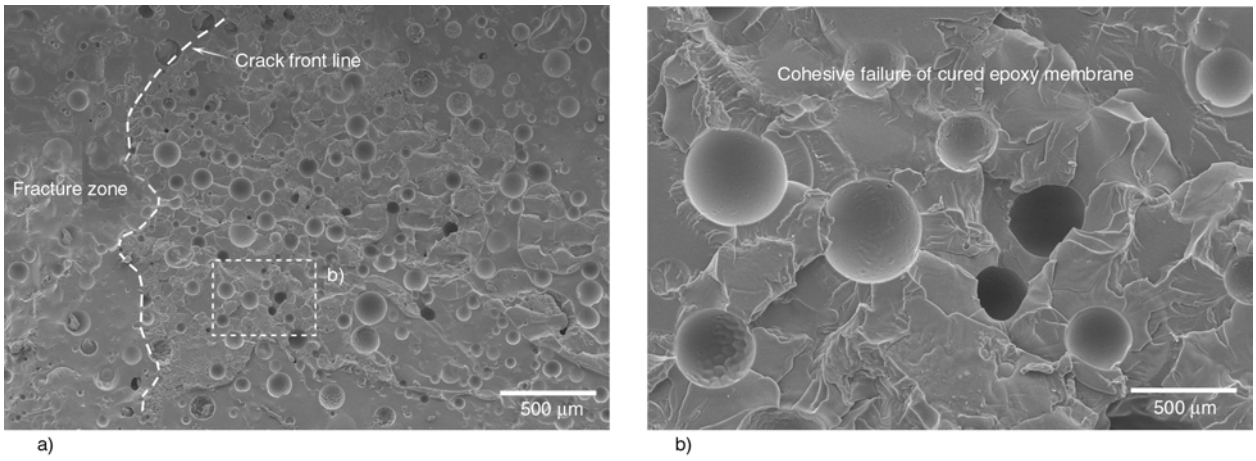

Figure 7. SEM micrographs of fatigue fracture surface of self-healing specimen. Crack can hardly advance for $1 \cdot 10^7$ cycles and hence is fully arrested. The specimen was fractured under static load using a rate of displacement of 3 mm/min without precrack. The fatigue testing parameters are ΔK_I = 0.504 MPa·m$^{1/2}$, K_{max} = 0.560 MPa·m$^{1/2}$, K_{min} = 0.056 MPa·m$^{1/2}$, R = 0.1 and f = 5 Hz. Note: The crack propagates from right to left in the images.

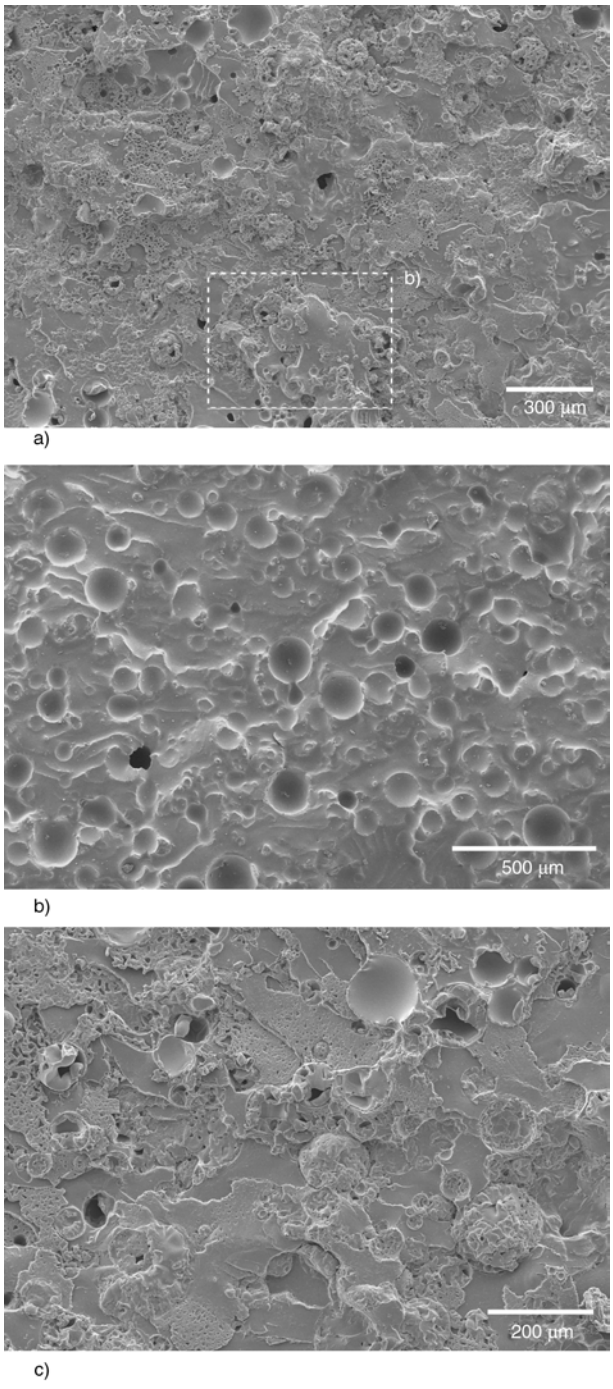

Figure 9. SEM micrographs of fatigue fracture surface of self-healing specimen. The testing parameters are $\Delta K_I = 0.554$ MPa·m$^{1/2}$, $K_{max} = 0.616$ MPa·m$^{1/2}$, $K_{min} = 0.062$ MPa·m$^{1/2}$, $R = 0.1$ and $f = 5$ Hz. Note: The crack propagates from left to right in the images.

cured healing agent membranes, adhesively bonded epoxy from the opposite fracture plane is also discovered at some regions. Both result in retardation of crack growth (Figure 8). Evidently, adhesive bonding mechanism governs fatigue life extension in this regime.

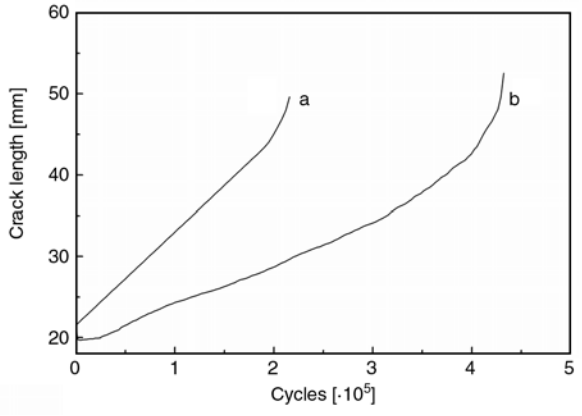

Figure 10. Crack length vs. fatigue cycles of (a) control specimen and (b) self-healing specimen. The testing parameters are $\Delta K_I = 0.605$ MPa·m$^{1/2}$, $K_{max} = 0.672$ MPa·m$^{1/2}$, $K_{min} = 0.067$ MPa·m$^{1/2}$, $R = 0.1$ and $f = 5$ Hz.

Under high ΔK_I (i.e. when K_{max} approaches K_{IC}), the mechanical kinetics of fatigue crack growth is extremely fast and the healing system does not have sufficient time to inhibit the crack propagation. This causes specimen failure within very short time. In this regime, the specimen fatigue life lags behind the time for the healing agent to gel. For example, when $\Delta K_I = 0.605$ MPa·m$^{1/2}$ ($K_{max}/K_{IC} = 0.97$), the fatigue crack in the self-healing specimen shows a constant growth rate with occasional crack retardation (refer to curve b in Figure 10). The healing efficiency is estimated to be about 89%. Accordingly, the SEM photos in Figure 11 indicate that the released healing agent has sparsely covered the fatigue fracture surface, and some were stretched into tapeworm-shaped gels with obvious tearing traces. It suggests that the healing agent suffered from severe tension action in the process of gelling or polymerization. On the basis of these results, we know that when the mechanical kinetics of fatigue crack growth becomes the controlling factor, the liberated healing agent lacks enough time to produce strong adhesion for inhibiting the crack advance.

It is worth noting that, when ΔK_I further increases, as K_{max} overly approaches the fracture toughness of the polymer, K_{IC}, unstable fracture will occur. A summary of life extension values under different loading conditions is given in Figure 12. The lower the applied range of stress intensity, the more evident the retardation effect and the higher healing efficiency. This trend is fully in line with the simu-

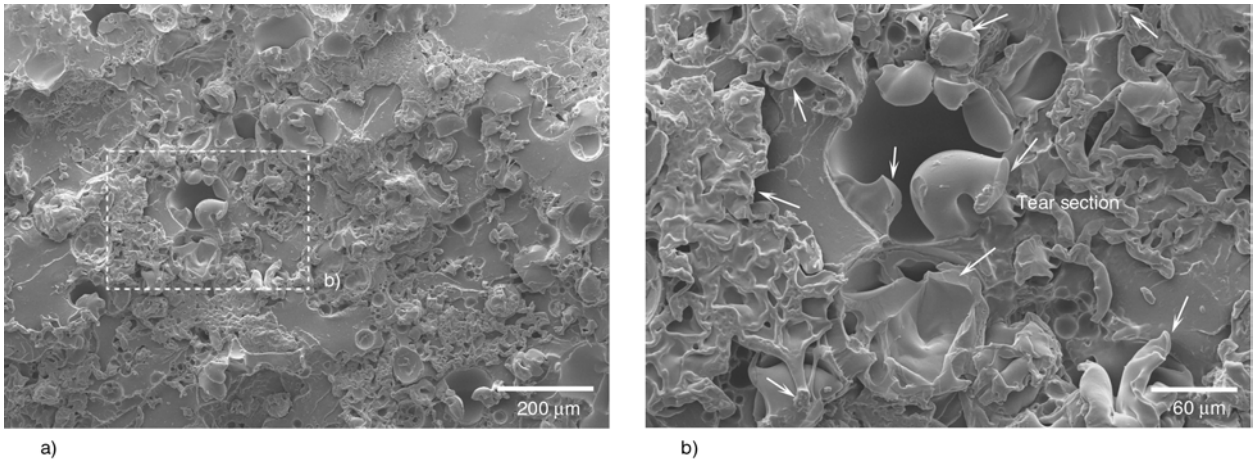

Figure 11. SEM micrographs of fatigue fracture surface of self-healing specimen. The testing parameters are ΔK_I = 0.605 MPa·m$^{1/2}$, K_{max} = 0.672 MPa·m$^{1/2}$, K_{min} = 0.067 MPa·m$^{1/2}$, R = 0.1 and f = 5 Hz. Note: The crack propagates from left to right in the images.

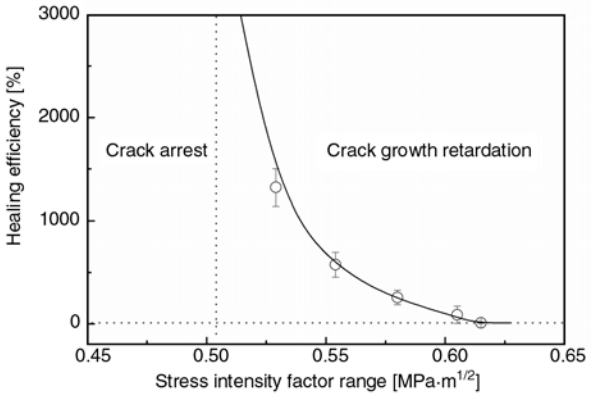

Figure 12. Healing efficiency of self-healing specimens as a function of stress intensity factor range, ΔK_I. The data are calculated partly using the results in Figure 6, 8 and 10.

lative healing results by dynamic manual infiltration [12]. Especially when ΔK_I is not more than 0.504 MPa·m$^{1/2}$, crack can hardly advance for more than 10^7 cycles as a result of gelation and solidification of the healing agent, and hence is considered to be fully arrested. In this context, the value of ΔK_I of 0.504 MPa·m$^{1/2}$ represents a watershed between fatigue crack growth retardation and crack arrest. Compared with control specimen, the mechanisms of adhesive bonding and polymeric wedge involved in crack tip shielding of self-healing specimens are highlighted, regardless whether ΔK_I is high or low.

3.4. Effects of steady-state stress intensity and healing time

According to Equation (2), it is known that if the fatigue crack opening load is purposely increased by a wedge with adhesive properties at the crack tip, the effective stress intensity factor range would be reduced [18, 20–26]. Keeping this idea in mind, researchers have made attempts to artificially introduce crack surface contact. Size and performance of the wedge have been found to be the most crucial factors affecting the crack closure effect. In this work, loading condition is investigated with a rest period to allow that (i) healing can be conducted with stationary crack faces and (ii) the healing agent flowing out of the capsules can form a crosslinked epoxy wedge in the crack tip. Meantime, the wedge size is adjusted by changing the steady-state stress intensity required for holding the crack open after a small amount of crack growth, while the wedge performance is tuned by changing the steady-state healing time, during which the cyclic loading pauses and crack is held open.

Figure 13 exhibits that the fatigue life extension due to precrack healing is drastically improved by adding a rest period. In the case of steady-state stress intensity = 0, loading is stopped after a small amount of crack growth and the specimen is allowed to heal unloaded for 10 min to ensure partial cure of the healing agent. The crack tip regresses to the approximate position of the TDCB notch as shown by curve b in Figure 13. Then, after about $4.1 \cdot 10^4$ cycles, the crack tip slowly progresses through the healed region to its location prior to healing. The crack growth rate of the self-healing specimens is lower than that of control specimens on the whole because the fracture toughness of the healing agent develops rapidly within

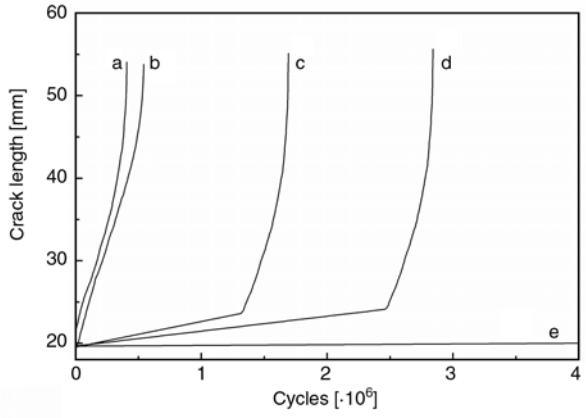

Figure 13. Crack length vs. fatigue cycles of self-healing specimens. The applied steady-state stress intensity for holding crack open and steady-state healing time are: (a) 0 MPa·m$^{1/2}$, 0 min, (b) 0 MPa·m$^{1/2}$, 10 min, (c) 0.336 MPa·m$^{1/2}$, 9.5 min, (d) 0.168 MPa·m$^{1/2}$, 10 min, and (e) 0.336 MPa·m$^{1/2}$, 10 min. The testing parameters are ΔK_I = 0.605 MPa·m$^{1/2}$, K_{max} = 0.672 MPa·m$^{1/2}$, K_{min} = 0.067 MPa·m$^{1/2}$, R = 0.1 and f = 5 Hz.

short period of time and exceeds that of matrix as indicated in Figure 4. The fatigue healing efficiency for this case is around 33%.

Sharp *et al*. [18] indicated that the load level or stress intensity applied for holding the crack open plays a decisive role in retarding or arresting fatigue crack. Evidently, it is also valid for the current system. Fatigue crack growth is retarded at different steady-state stress intensities. Higher steady-state stress intensity applied during healing results in more prominent retardation effect (Figure 13) and higher healing efficiency (Figure 14). The results coincide with those obtained by the simulative healing through static manual infiltration [12]. When the applied stress intensity is not less than 0.336 MPa·m$^{1/2}$ (for the steady-state healing time of 10 min), crack can hardly advance for more than 10^7 cycles and is considered to be completely arrested. Therefore, the applied stress intensity of 0.336 MPa·m$^{1/2}$ acts as a threshold for distinguishing fatigue crack growth retardation from crack arrest (Figure 14). The above results can be understood by the fact that thicker wedge is produced when the specimen is healed at higher applied steady-state stress intensity. Consequently, ΔK_{wedge} increases and ΔK_{eff} decreases (refer to Equation (2)). When $\Delta K_{eff} \le \Delta K_{th}$ (i.e. $\Delta K_{bonding} + \Delta K_{wedge} \ge \Delta K_I - \Delta K_{th}$), fatigue crack is fully arrested.

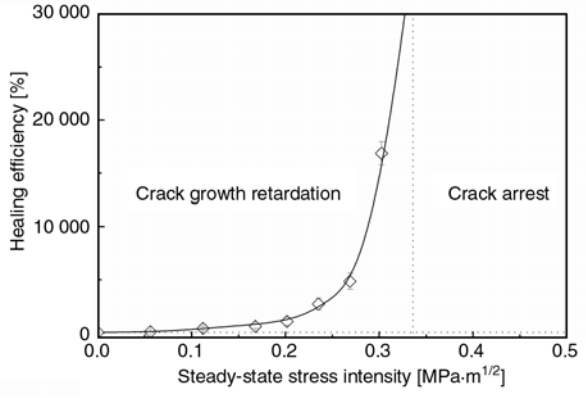

Figure 14. Healing efficiency of self-healing specimens with a rest period as a function of the applied steady-state stress intensity. The data are calculated partly using the results in Figure 13. The steady-state healing time is set at 10 min. The testing parameters are ΔK_I = 0.605 MPa·m$^{1/2}$, K_{max} = 0.672 MPa·m$^{1/2}$, K_{min} = 0.067 MPa·m$^{1/2}$, R = 0.1 and f = 5 Hz.

Taking the specimen with fatigue crack arrested at steady-state stress intensity of 0.336 MPa·m$^{1/2}$ as an example. The specimen is eventually fractured at static load without precrack and the fracture toughness reaches 1.089 MPa·m$^{1/2}$, much higher than the value of the virgin self-healing specimen (0.695 MPa·m$^{1/2}$). As shown in Figure 15, the healing agent released during the precrack event has formed a thick polymer wedge at the crack tip, leading to cohesive failure of the matrix in the ultimate fracture experiment. Very strong adhesion must have been achieved, which certainly favors to arrest crack.

In addition to the above study on the effect of steady-state stress intensity that is related to wedge size, the influence of steady-state healing time that is related to wedge performance is evaluated in the following. For this purpose, the fatigue test paused after a small amount of crack growth and the crack was held open at a constant steady-state stress intensity of 0.336 MPa·m$^{1/2}$. After different steady-state healing times from 0 to 1 h, fatigue loading was reestablished.

The results shown in Figure 13 and 16 indicate that the healing effect is negligible (healing efficiency = 10~15%) within the steady-state healing time range of 0~8.5 min. When the steady-state healing time reaches 9.5 and 9.75 min, however, the healing efficiency is greatly increased to 415 and 1263%, respectively. In the case that the steady-state heal-

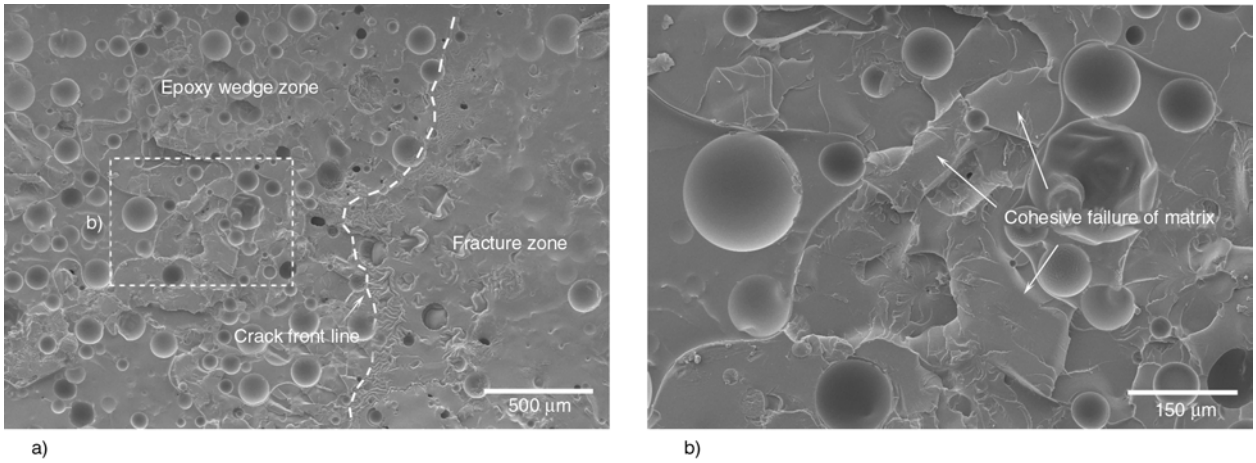

Figure 15. SEM micrographs of fatigue fracture surface of self-healing specimen. The applied steady-state stress intensity for holding crack open is 0.336 MPa·m$^{1/2}$ and the steady-state healing time is 10 min. Crack can hardly advance for 107 cycles and hence is fully arrested. The specimen was fractured under static load using a rate of displacement of 3 mm/min without precrack. The fatigue testing parameters are ΔK_I = 0.605 MPa·m$^{1/2}$, K_{max} = 0.672 MPa·m$^{1/2}$, K_{min} = 0.067 MPa·m$^{1/2}$, R = 0.1 and f = 5 Hz. Note: The crack propagates from left to right in the images.

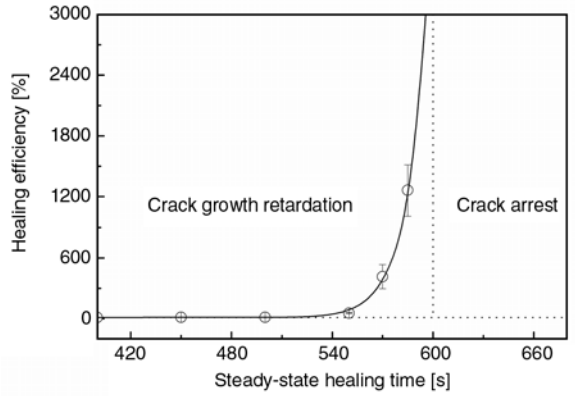

Figure 16. Healing efficiency of self-healing specimens with a rest period as a function of steady-state healing time. The data are calculated partly using the results in Figure 13. The applied steady-state stress intensity for holding crack open is 0.336 MPa·m$^{1/2}$. The testing parameters are ΔK_I = 0.605 MPa·m$^{1/2}$, K_{max} = 0.672 MPa·m$^{1/2}$, K_{min} = 0.067 MPa·m$^{1/2}$, R = 0.1 and f = 5 Hz.

ing time is not less than 10 min, crack can hardly advance after more than 10^7 fatigue cycles and is considered to be fully arrested. Similarly, this time can be regarded as the critical threshold to distinguish fatigue crack growth retardation from crack arrest (Figure 16). The phenomena have been found in the simulative healing tests based on static manual infiltration [12], but the critical value of steady-state healing time becomes longer for the present *in-situ* system. It might be because the ingredients ratio, mixing uniformity and amount of the released healing agent in fatigue crack of self-healing specimens are not optimized as the case of simulative healing [12, 14].

The above results are closely related to the curing process of the healing agent and the development of its fracture toughness. During curing of the healing agent, the system transforms from low molecular liquid mixture into three dimensionally cross-linked macromolecular networks. Molecular dynamics and macroscopic behavior of the material drastically change in the meantime [16]. Previous study on curing kinetics demonstrated that the viscosity of the healing agent slowly increased in the beginning a few minutes after mixing, and then rapidly increased until it gelled within about one minute [13, 14]. The gelation of the healing agent is essentially a rapid formation and increase process of hardness and adhesive strength as shown in Figure 4. Although nearly no adhesion can be detected at a time less than 6 min, fracture toughness of the healing agent sharply increases as of 8 min, and exceeds that of the epoxy matrix at about 20 min. With the rapid development of bonding strength of the cured healing agent, fatigue crack growth would become gradually difficult in the starting position. The deduction is confirmed by the fact that the longer the steady-state healing time corresponds to the fewer tearing marks in the gel state appearing at the initial phase of the fatigue crack (figure omitted). Accordingly, evident retardation effect is obtained for the steady-state healing time from 8 to

9.75 min and the crack is fully arrested for the steady-state healing time as of 10 min.

4. Conclusions

The self-healing epoxy materials containing encapsulated epoxy/mercaptan system exhibit significantly extended fatigue life as compared with the unfilled versions. Effects of microcapsules induced-toughening, hydrodynamic pressure crack tip shielding, polymeric wedge and adhesive bonding account for the improvement. Under different operation circumstances, however, the above mechanisms exert different influences on crack retardation.

The healing efficiency strongly depends on the applied stress intensity range, ΔK_I. The lower ΔK_I, the higher healing efficiency. The applied stress intensity range of 0.504 MPa·m$^{1/2}$ represents a watershed between fatigue crack growth retardation and crack arrest for the current system.

In the case of high ΔK_I, extension of fatigue life in self-healing specimens can also be achieved by holding the crack open for a while after a small amount of crack growth. Higher steady-state stress intensity required for holding the crack open results in more prominent retardation effect. When the steady-state stress intensity is not less than 0.336 MPa·m$^{1/2}$ (for the steady-state healing time of 10 min), crack can hardly advance for more than 10^7 cycles and is considered to be completely arrested. In this case, adhesive bonding and polymeric wedge mechanisms play the controlling role. Similarly, on the other hand, when the steady-state healing time is not less than 10 min (for the steady-state stress intensity of 0.336 MPa·m$^{1/2}$), the fatigue crack is fully arrested.

Acknowledgements

The authors are grateful to the support of the Natural Science Foundation of China (Grants: U0634001, 20874117, 50573093, 51073176 and 50903095), Doctor Fund of Ministry of Education of China (Grant: 2009310004111671) and the Science and Technology Program of Guangdong Province (Grant: 2010B010800021) and China Postdoctoral Science Foundation.

References

[1] Murphy E. B., Wudl F.: The world of smart healable materials. Progress in Polymer Science, **35**, 223–251 (2010).
DOI: 10.1016/j.progpolymsci.2009.10.006

[2] Yuan Y. C., Yin T., Rong M. Z., Zhang M. Q.: Self healing in polymers and polymer composites. Concepts, realization and outlook: A review. Express Polymer Letters, **2**, 238–250 (2008).
DOI: 10.3144/expresspolymlett.2008.29

[3] Caruso M. M., Davis D. A., Shen Q., Odom S. A., Sottos N. R., White S. R., Moore J. S.: Mechanically-induced chemical changes in polymeric materials. Chemical Reviews, **109**, 5755–5798 (2009).
DOI: 10.1021/cr9001353

[4] Brown E. N., White S. R., Sottos N. R.: Retardation and repair of fatigue cracks in a microcapsule toughened epoxy composite – Part I: Manual infiltration. Composites Science and Technology, **65**, 2466–2473 (2005).
DOI: 10.1016/j.compscitech.2005.04.020

[5] Brown E. N., White S. R., Sottos N. R.: Retardation and repair of fatigue cracks in a microcapsule toughened epoxy composite – Part II: In situ self-healing. Composites Science and Technology, **65**, 2474–2480 (2005).
DOI: 10.1016/j.compscitech.2005.04.053

[6] Jones A. S., Rule J. D., Moore J. S., Sottos N. R., White S. R.: Life extension of self-healing polymers with rapidly growing fatigue cracks. Journal of the Royal Society Interface, **4**, 395–403 (2007).
DOI: 10.1098/rsif.2006.0199

[7] Maiti S., Geubelle P. H.: Cohesive modeling of fatigue crack retardation in polymers: Crack closure effect. Engineering Fracture Mechanics, **73**, 22–41 (2006).
DOI: 10.1016/j.engfracmech.2005.07.005

[8] Maiti S., Shankar C., Geubelle P. H.: Continuum and molecular-level modeling of fatigue crack retardation in self-healing polymers. Journal of Engineering Materials and Technology-Transactions of the ASME, **128**, 595–602 (2006).
DOI: 10.1115/1.2345452

[9] White S. R., Sottos N. R., Geubelle P. H., Moore J. S., Kessler M. R., Sriram S. R., Brown E. N., Viswanathan S.: Autonomic healing of polymer composites. Nature, **409**, 794–797 (2001).
DOI: 10.1038/35057232

[10] Daniel J. S., Kim Y. R.: Laboratory evaluation of fatigue damage and healing of asphalt mixtures. Journal of Materials in Civil Engineering, **13**, 434–440 (2001).
DOI: 10.1061/(ASCE)0899-1561(2001)13:6(434)

[11] Zako M., Takano N.: Intelligent material systems using epoxy particles to repair microcracks and delamination damage in GFRP. Journal of Intelligent Material Systems and Structures, **10**, 836–841 (1999).
DOI: 10.1106/YEIH-QUDH-FC7W-4QFM

[12] Yuan Y. C., Rong M. Z., Zhang M. Q., Yang G. C., Zhao J. Q.: Healing of fatigue crack in epoxy materials with epoxy/mercaptan system via manual infiltration. Express Polymer Letters, **4**, 644–658 (2010).
DOI: 10.3144/expresspolymlett.2010.79

[13] Yuan Y. C., Rong M. Z., Zhang M. Q., Chen J., Yang G. C., Li X. M.: Self-healing polymeric materials using epoxy/mercaptan as the healant. Macromolecules, **41**, 5197–5202 (2008).
DOI: 10.1021/ma800028d

[14] Yuan Y. C., Rong M. Z., Zhang M. Q., Yang G. C.: Study of factors related to performance improvement of self-healing epoxy based on dual encapsulated healant. Polymer, **50**, 5771–5781 (2009).
DOI: 10.1016/j.polymer.2009.10.019

[15] Brown E. N., Sottos N. R., White S. R.: Fracture testing of a self-healing polymer composite. Experimental Mechanics, **42**, 372–379 (2002).
DOI: 10.1007/BF02412141

[16] Petrie E. M.: Epoxy adhesive formulations. McGraw-Hill, New York (2006).

[17] Brown E. N., White S. R., Sottos N. R.: Fatigue crack propagation in microcapsule-toughened epoxy. Journal of Materials Science, **41**, 6266–6273 (2006).
DOI: 10.1007/s10853-006-0512-y

[18] Sharp P. K., Clayton J. Q., Clark G.: Retardation and repair of fatigue cracks by adhesive infiltration. Fatigue and Fracture Engineering Materials and Structures, **20**, 605–614 (1997).
DOI: 10.1111/j.1460-2695.1997.tb00292.x

[19] Elber W.: Fatigue crack closure under cyclic tension. Engineering Fracture Mechanics, **2**, 37–45 (1970).
DOI: 10.1016/0013-7944(70)90028-7

[20] James M. N., Smith G. C.: Surface microcrack closure in fatigue: A comparison of compliance and crack sectioning data. International Journal of Fracture, **22**, R69–R75 (1983).
DOI: 10.1007/BF00942729

[21] Song P. S., Hwang S., Shin C. S.: Effect of artificial closure materials on crack growth retardation. Engineering Fracture Mechanics, **60**, 47–58 (1998).
DOI: 10.1016/S0013-7944(97)00180-X

[22] Shin C. S., Cai C. Q.: Surface fatigue crack growth suppression in cylindrical rods by artificial infiltration. International Journal of Fatigue, **30**, 560–567 (2008).
DOI: 10.1016/j.ijfatigue.2007.03.005

[23] Shin C. S., Wang C. M., Song P. S.: Fatigue damage repair: A comparison of some possible methods. International Journal of Fatigue, **18**, 535–546 (1996).
DOI: 10.1016/S0142-1123(96)00029-1

[24] Ur-Rehman A., Thomason P. F.: The effect of artificial fatigue crack closure on fatigue crack growth. Fatigue and Fracture of Engineering Materials and Structures, **16**, 1081–1090 (1993).
DOI: 10.1111/j.1460-2695.1993.tb00079.x

[25] Shin C. S., Chen Z. Z.: Fatigue life extension by electroless nickel infiltration plating. International Journal of Fatigue, **23**, 777–788 (2001).
DOI: 10.1016/S0142-1123(01)00038-X

[26] Wang Y., Zho M., Feng D.: A study of retarding fatigue crack growth using an artificial wedge. Fatigue and Fracture of Engineering Materials and Structures, **16**, 363–376 (1993).
DOI: 10.1111/j.1460-2695.1993.tb00093.x

eXPRESS Polymer Letters Vol.5, No.1 (2011) 60–72
Available online at www.expresspolymlett.com
DOI: 10.3144/expresspolymlett.2011.7

Crystalline polymer decoration on multiwalled carbon nanotubes: MWCNT-induced P4VP periodic crystallization in CO_2-expanded liquids

Y. Liu[1], *Y. N. Wei*[2], *R. H. Qin*[1], *L. Y. Zhang*[1], *L. T. Yang*[1], *H. P. Li*[1*], *X. J. Li*[2]

[1]Department of Chemistry, Zhengzhou University, Zhengzhou, Henan 450001, China
[2]Physical Engineering College, Zhengzhou University, Zhengzhou, Henan 450001, China

Received 13 July 2010; accepted in revised form 17 September 2010

Abstract. This work reports the functionalization of multi-walled carbon nanotubes (MWCNTs) with crystalline poly(4-vinylpyridine) (P4VP) in CO_2-expanded liquids (CXLs). The structure and morphology of MWCNT-induced polymer crystallization are examined, with the focus on molecular weight of P4VP (MW-P4VP), the pressure of CXLs and the concentration of P4VP. First, it is observed that the crystallization morphologies for the P4VP/MWCNTs composite with a low molecular weight P4VP (LMW-P4VP) matrix could be finely controlled in CXLs, and it is surprising to find that the $P4VP_{8700}$ wrapping patterns undergo a morphological evolution from dot crystals to dotted helical wrappings, and then to dense helical patterns by facile pressure tuning under lower polymer concentration. In other words, the CXLs method enables superior control of the P4VP crystallization patternings on MWCNTs, particularly efficient for LMW-P4VP at lower polymer concentration. Meanwhile, the CXL-assisted P4VP crystal growth mechanism on MWCNT is investigated, and the dominating growth mechanism is attributed to 'normal epitaxy' at lower P4VP concentration rather than 'soft epitaxy' at higher concentration. We believe that this work reports a new crystalline polymer wrapping approach in CXLs to noncovalent engineering of MWCNTs surfaces.

Keywords: *polymer composites, polymer crystallization, carbon nanotubes, poly(4-vinylpyridine), CO_2-expanded liquid*

1. Introduction

Carbon nanotubes (CNTs) have attracted tremendous attention in recent years because of their superb optical, electronic and mechanical properties. However, the problem of poor solubility and processability remains a severe limitation to the extensive use of CNTs, which explains the continuous interest in a further functionalization and modification of the CNT surface. Both chemical functionalization and non-covalent wrapping methods have been reviewed recently [1, 2]. Herein, noncovalent functionalization of CNTs is of particular interest because it enables one to tailor their properties while still preserving nearly all of the nanotube's intrinsic properties. The non-covalent methods involve using soft matter such as surfactants, oligomers, biomolecules and polymers to 'wrap' CNTs, to enhance their solubility or dispersibility [3–5].

Polymeric solubilization and functionalization of CNTs can play a vital role in exploring and developing its application. Polymer/CNT nanocomposite (PCN) is one of the most promising fields for CNTs [6, 7]. The potential applications of PCNs include conductivity enhancement, electrostatic dissipation and aerospace structural materials, and the properties of PCN usually differ substantially from those of the pristine polymer matrix, and a variety of

*Corresponding author, e-mail: lihongping@zzu.edu.cn

polymers have been studied to form nanocomposites with CNTs depending on the targeted properties [1]. Recently, PCNs formed by CNTs and semicrystalline polymers such as isotactic polypropylene (iPP), polyethylene (PE), polyvinyl alcohol, polyacrylonitrile, poly(3-caprolactone), thermoplastic polyimide, conjugated organic polymer, as well as thermoplastic elastomers such as polyurethane systems have been studied [1, 8, 9]. Wrapping CNTs with crystalline polymers is thought to be an ideal functionalization method considering the excellent mechanical properties of crystalline polymers as well as the potential specific chain registry of different polymers upon CNTs. This method can retain the structural integrity of CNTs and simultaneously overcome the disability of the noncovalent modification method [8]. The CNT-induced polymer crystallization with the focus on the nanohybrid shish kebab (NHSK) structure have recently been reviewed by Li *et al.* [1].

Gas expanded liquids (GXLs) are mixtures consisting of a liquid organic solvent and a near-critical gas such as CO_2. These mixtures are currently being explored as potential replacements for pure organic solvents in chemical processing [10–12]. As such, they reflect a compromise between the use of conventional solvents, which are a major source of industrial pollution, and completely benign solvents like neat CO_2, whose poor solvent qualities and high pressure requirements have limited its application. In addition to the environmental benefits of GXLs, the ability to readily pressure tune the mole fraction of the gaseous component and thereby alter the solvating power, fluidity, and many other properties of these solvents proves advantageous in a variety of applications, such as materials processing [13, 14], analytical separations [15] and cleaning [16], and as media for organic reactions [11, 17, 18]. CO_2-expanded liquids (CXLs) are the most commonly used class of GXLs because of the safety and economic advantages of CO_2. CXLs have been regarded as the ideal solvents in a variety of roles including inducing separations, precipitating fine particles, and facilitating polymer processing [19]. CO_2 dissolution has been shown to lower the melting temperature, the crystallization temperature, and the glass transition temperature and to raise the rate and degree of crystallization for a variety of polymers, and polymer process in CXLs taking advantage of the melting-point lowering and viscosity-lowering effects has been used to adjust particle size and morphology of polymers and to facilitate extrusion, foaming, impregnation, and mixing or co-molding of polymers [19]. Moreover, GXLs/CXLs combine the beneficial properties of compressed gases and of conventional solvents, leading to a new class of tunable solvents that are often the ideal type of solvents for a given application while simultaneously reducing the environmental burden through substantial replacement of organic solvents with environmentally benign CO_2 [19].

This work aims at reporting the functionalization of MWCNTs with polymers in CXLs, and the model polymer used is poly(4-vinylpyridine) (P4VP). P4VP is so intriguing material and there are several reasons for choosing it as our functional polymer. First of all, it has reactive pyridine group for coordinative with transition metals, which can be widely used in the field of catalysis [20–23], humidity sensitive material [24], waste water treatment [25, 26] and also as a host ligand of metal-containing chromophores [27, 28]. Moreover, its solution behavior can be changed significantly, being a hydrophobic polymer in apolar solvents and a cation polyelectrolyte in water at low pH [29, 30]. Therefore, the pH-sensitive P4VP can be readily quaternized by alkylogen and then form the positively charged polyelectrolytes as sensors and actuators [31, 32] and the N-alkylated pyridinium polymers as antimicrobial materials [33]. Thus, the unique hybrid structure of P4VP/MWCNT nanocomposite is expecting to play a vital role in exploring and developing the potential applications of the corresponding PCNs.

In this article, efforts are made to examine the structure and morphology of MWCNT-induced P4VP crystallization, with the focus on three types of peripheral effect on the periodic morphology change. We shall first discuss the effect of the molecular weight of P4VP, followed by the pressure of CXLs and the concentration of P4VP effect on the crystallization behavior. Meanwhile, the mechanism of CXL-assisted P4VP crystal growth on MWCNT is investigated. We believe that this work reports a new wrapping approach in CXLs to noncovalent engineering of MWCNTs surfaces that leads to an enhancement of solubility of MWCNTs and enables superior control of the relative placement of functionalities on the nanotube surface. The unique peri-

odic wrapping PCNs in CXLs can serve as a nanoscale template for CNT functionalization in a milder way compared to the well-known supercritical antisolvent (SAS) processes.

Here, the difference between a CXL process and a SAS method should be mentioned. According to the phase behavior of the solvent mixture CO_2+dimethyl sulphoxide (DMSO) in this work, the SAS processes correspond to an operating region above the critical pressure of the mixture (Pc). At conditions above the Pc, DMSO and CO_2 are miscible in the whole composition range and polymer modification behavior results from gas-phase nucleation. The CXL processes are under conditions below the mixture critical pressure, and there exists a vapor-liquid equilibrium, and the CXL material processing is usually conducted in the liquid phase of the solvent mixture. In this work, the critical composition (critical mole fraction of CO_2, x_{C,CO_2}) and critical pressure of CO_2-DMSO at 338.2 K are $x_{C,CO_2} = 0.860$ and $P_C = 15.11$ MPa, respectively [34]. The experimental pressures are chosen to be lower than P_C and along the bubble-point curve at 338.2 K in CO_2-expanded DMSO. Therefore, the MWCNT functionalization in CXLs can be performed under milder operating conditions in contrast with the SAS processes.

2. Experimental section

2.1. Materials

MWCNTs were from Tsinghua Unversity (China) with a purity of 93 wt%. Dimethyl sulphoxide (DMSO) and acetic anhydride $(CH_3CO)_2O$ were supplied by the Damao Chemical Reagent Co., Ltd. (Tianjin, China). The monomer 4-vinyl pyridine (4VP) and Benzoyl Peroxide (BPO) were from Alfa Aesar (Beijing, China), and 2,2,6,6,-tetramethylpiperidine-N-oxyl (TEMPO) was supplied by Dengfeng Chemical Reagent Co., Ltd. (Tianjin, China). CO_2 with a purity of 99.95% was provided by Zhengzhou Shuangyang Gas Co. (China). 4VP was purified prior to use by fractionated distillation. BPO was purified by reprecipitation of a saturated dried chloroform solution by methanol. TEMPO and $(CH_3CO)_2O$ were used as received. $P4VP_{8700}$ (M_n = 8700) and $P4VP_{45\,000}$ (M_n = 45000) used in this work were prepared in our lab. MWCNTs were dried in a vacuum oven at 308.2 K for 24 h before use.

2.2. Preparation of P4VP

$P4VP_{8700}$ was prepared according to the literature [35], and $P4VP_{45\,000}$ prepared by a method described by Fischer [36]. In a typical polymerization procedure, a two-necked round-bottom flask was loaded with an appropriate amount of TEMPO, 4VP, BPO, and/or $(CH_3CO)_2O$; degassed by an argon gas purge; and sealed off under vacuum. The temperature of the polymerization and the duration was varied. P4VP formed, was end-capped with TEMPO, was precipitated in hexane, and dried under vacuum. The detailed reaction conditions for the preparation of P4VP, the number-average molecular weight (M_n) and polydispersity index (M_w/M_n) of P4VP determined by Gel Permeation Chromatography (GPC) are provided in Table 1.

2.3. The functionalization of MWCNTs by P4VP

The experimental apparatus is illustrated in Figure 1. Typically, appropriate amount of P4VP were dissolved in an organic solvent DMSO at a suitable temperature. 0.1 mg of MWCNTs was dispersed in DMSO solution, the mixture was then ultrasonicated for 2–4 h at the temperature between 298.2–318.2 K in order to disperse the MWCNTs homogeneously in the solution. The dispersion was then added into P4VP/DMSO solution in a tube. After equilibration, the tube containing the mixture was quickly transferred into a stainless-steel autoclave at the temperature of 338.2 K. CO_2 was then charged into the autoclave to achieve the desired pressure

Table 1. Polymerization of 4-vinyl pyridine at different reaction conditions

Sample	Time [h]	Accelerator	Temperature [K]	TEMPO/BPO molar ratio	M_n[a]	M_w/M_n[a]
1	16	$(CH_3CO)_2O$[b]	368.2–408.2	1.30:1	8700	1.66
2	7	–	398.2	0.65:1	45000	1.88

[a]Number-average molecular weight (M_n) and polydispersity index (M_w/M_n) were determined by Gel Permeation Chromatography (GPC) in DMF at 313.2 K, flow rate 1 ml/min

[b]1% (w/w)

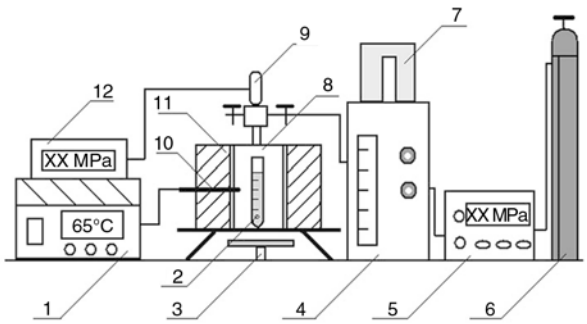

Figure 1. CXLs experimental apparatus description diagram: (1) temperature controller; (2) magnet; (3) magnetic stirrers; (4) syringe pump; (5) pump controller; (6) gas cylinder; (7) cooling jacket.; (8) autoclave (9) pressure transducer; (10) thermoelectric couple; (11) heating-jacket; and (12) pressure indicator

within a short time. After 3 h reaction in CO_2-expanded DMSO, the system was slowly depressurized and the sample was collected and labeled.

Comparative experiments of $P4VP_{8700}$ or $P4VP_{45\,000}$ decorated MWCNTs under the same experimental conditions free of CO_2 were also performed, and the corresponding TEM images are provided in Figure 2.

2.4. Characterization methods

The number-average molecular weight (M_n) and polydispersity index (M_w/M_n) of P4VP were determined by GPC (1200 series, Agilent Technologies U.S.A.), and are tabulated in Table 1. The morphology of P4VP functionalized MWCNTs was characterized by transmission electron microscopy (TEM). Samples were collected on a TEM grid and conducted using a JEOL JEM-2100 microscope with an accelerating voltage of 200 kV.

3. Results and discussion

The challenging task is to achieve the controlled functionalization of MWCNTs by adjusting the P4VP crystallization patternings. Accordingly, three types of peripheral effect such as MW-P4VP, the mass ratio of P4VP to MWCNT, and the pressure of CXLs on the periodic morphology change are examined. The experiments in this work are designed as such: MW-P4VP as M_{8700} and $M_{45\,000}$ are used, respectively; different mass ratio of P4VP to MWCNT as 5:1 (i.e., 0.01 wt% P4VP to 0.002 wt% MWCNTs) and 10:1 (i.e., 0.02 wt% P4VP to 0.002 wt% MWCNTs) are employed, respectively; and pressures are chosen along the bubble-point curve at 338.2 K in CO_2-expanded DMSO.

3.1. Effect of pressure in CO_2-expanded DMSO on the modification of MWCNTs with $P4VP_{8700}$

The experimental conditions for the modification of MWCNTs are that reaction systems of P4VP concentration (0.01 wt%) and MWCNTs concentration (0.002 wt%) in DMSO were treated at 338.2 K and different pressures for 3 h, with pressures chosen to

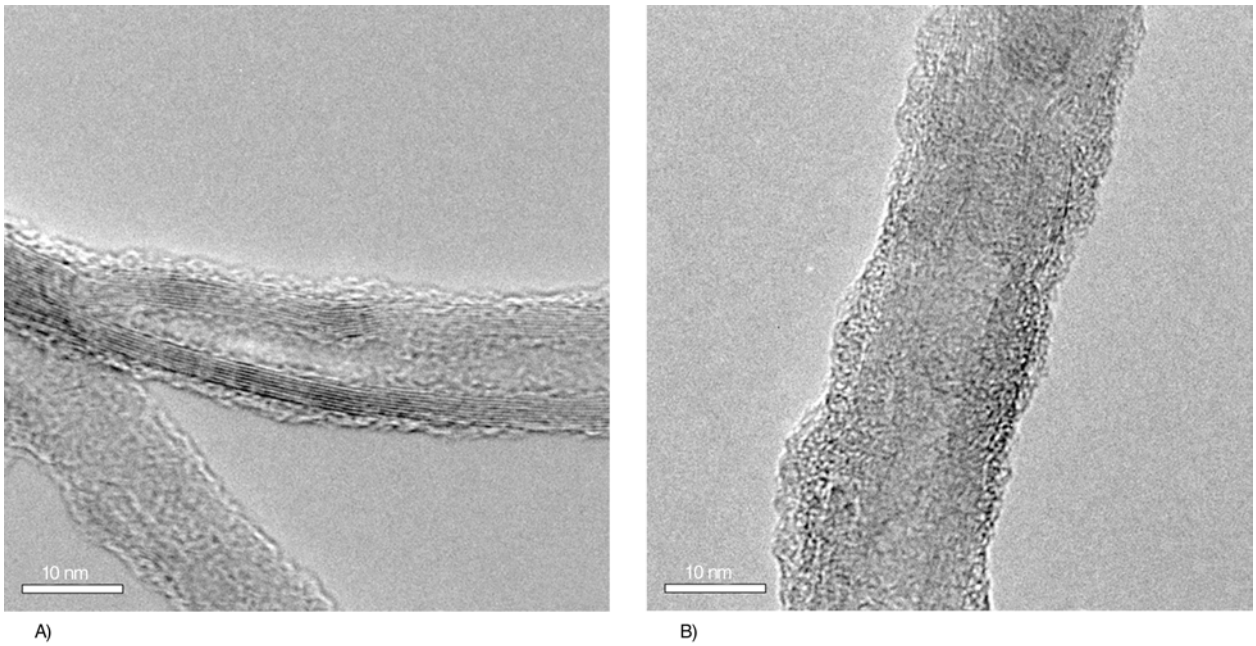

Figure 2. TEM images of P4VP-decorated MWCNTs obtained in DMSO at 338.2 K for 3 h. The P4VP and MWCNTs concentrations in DMSO are 0.01 and 0.002 wt%, respectively: (A) $P4VP_{8700}$; (B) $P4VP_{45\,000}$.

be 6.22 MPa (x_{CO_2} = 0.325), 9.84 MPa (x_{CO_2} = 0.505) and 13.50 MPa (x_{CO_2} = 0.715), respectively, along the bubble-point curve at 338.2 K in CO_2-expanded DMSO [34]. The compositions of the liquid phase (mole fraction of CO_2, x_{CO_2}) were determined using known relations between the liquid composition and the coexisting vapor pressure of CO_2-DMSO phase diagram at 338.2 K [34]. The characteristic structures of $P4VP_{8700}$ decorated MWCNTs are reflected in the TEM image (Figure 3A–3D). From Figure 3, it is obvious that $P4VP_{8700}$ can grow by epitaxy on MWCNTs when MWCNTs are used as the modification subject. And it is interesting to find that multiple P4VP periodic

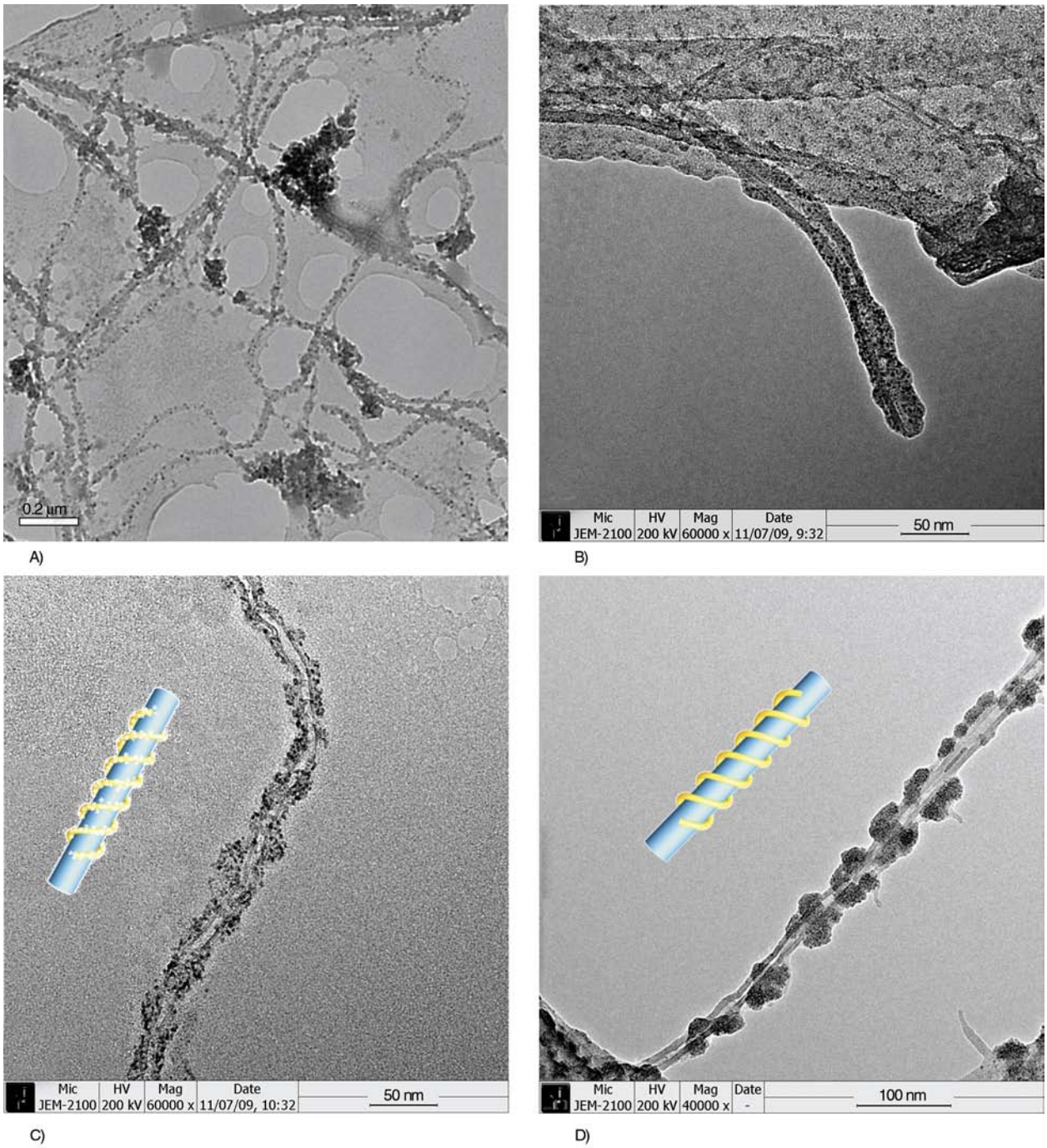

Figure 3. TEM images of $P4VP_{8700}$-decorated MWCNTs obtained in CO_2-expanded DMSO conditions (338.2 K/varied pressure for 3 h) and $P4VP_{8700}$ concentrations in DMSO (0.01 wt%), with MWCNTs concentrations of 0.002 wt%: (A)/(B) 6.22 MPa (x_{CO_2} = 0.325); (C) 9.84 MPa (x_{CO_2} = 0.505); (D) 13.5 MPa (x_{CO_2} = 0.715). The schematic representations of the helical structures of the P4VP/MWCNTs composite are shown on image (C) and (D), respectively.

crystallization structures are formed with increasing pressure, i.e., the P4VP cystallization on MWCNTs undergoes a wrapping pattern transition first from dots (Figure 3A, 3B) to dotted-helix (Figure 3C), and then to a dense helical structure (Figure 3D) as the pressure increases from 6.22 to 9.84, and then to 13.50 MPa, respectively. So far as we know, it is the first time that the pressure dependence of morphological evolution of crystalline P4VP is obtained in GXLs.

The images from Figure 3A, 3B (6.22 MPa) indicate that the sidewalls of MWCNTs are decorated with some dots, and these dots are generally regarded as nanocrystals. The mechanism is suggested as follows. CO_2 cannot dissolve P4VP but is miscible with DMSO under suitable conditions. Therefore, compressed CO_2 is used as the antisolvent for P4VP/DMSO system. With the injection of CO_2 to the P4VP/DMSO system, the volume of the DMSO-rich phase is expanded owing to the dissolution of CO_2 and the solvent power on P4VP is reduced, therefore P4VP molecules precipitate out of the supersaturated solution and start to be adsorbed on the surface of MWCNTs. With the increasing amount of P4VP wrapping, P4VP molecules with folded-chains begin to align along MWCNTs as dots crystal so as to decrease the polymer surface energy, i.e., P4VP dot crystals are formed on MWCNTs because this structure is energetically favorable and a cooperative orientation between the polymer chains and MWCNT axes supports this crystallization pattern. So at lower pressure as 6.22 MPa, there spawned tiny size of heteronucleus dots of P4VP on the MWCNTs almost everywhere. These P4VP dot-like nanocrystals formed on the MWCNTs at lower pressure could also be regarded as a steady intermediate state, which could further form ordered patterning of nanohybrid structure when suitable experimental conditions are achieved. Upon increasing CO_2 pressure to 9.84 MPa, the solvent strength of the CXLs would further decrease due to more CO_2 dissolved in DMSO; therefore more P4VP can be deposited. Under such circumstance, there are two possible factors that affect the nanohybrid P4VP crystal growth: the epitaxial growth of P4VP on CNTs and geometric confinement [1]. Here, the size of $P4VP_{8700}$ may be relatively small compared to the pristine MWCNTs (average diameter about 25–30 nm) used in the work. Therefore, on the surface of the CNTs with a diameter larger than the polymer size, the polymer behaves as if it were on a flat surface. Strict lattice match and epitaxy are therefore the main growth mechanisms herein [1]. And because of the different rolling directions or chiralities of the CNTs, there exist multiple orientations of the graphitic lattice with respect to the CNT axis. Meanwhile, polymer chains normally posses a coil conformation [37], thus, with more P4VP deposited under higher pressures (9.84 and 13.50 MPa), multiple orientations of the P4VP molecules would coil along the MWCNT axis with crystal lamellae oblique to the MWCNT axis and finally a helical P4VP wrapping pattern is formed owing to the dominance of the epitaxy factor. With CO_2 pressure further increases up to 13.50 MPa, more P4VP can be deposited compared to that at 9.84 MPa, therefore a denser P4VP helix on MWCNTs at 13.50 MPa is obtained whereas a dotted helical wrapping of P4VP is formed at 9.84 MPa.

3.2. Modification of MWCNTs with $P4VP_{45\,000}$ in CO_2-expanded DMSO

The experimental conditions are that the $P4VP_{45\,000}$ (concentration 0.01 wt%) and MWCNTs (concentration 0.002 wt%) in DMSO were treated at 338.2 K and different pressures for 3 h, with pressures chosen to be 10.47 MPa ($x_{CO_2} = 0.539$) and 11.84 MPa ($x_{CO_2} = 0.617$), respectively, along the bubble-point curve at 338.2 K in CO_2-DMSO [34]. The structures of $P4VP_{45\,000}$ decorated MWCNTs are shown in the TEM image (Figure 4A–4D).

It is shown from Figure 4 that the $P4VP_{45000}$ cystallization on MWCNTs undergoes a wrapping pattern evolution from dots (Figure 4A, 4B) to multi-helical wrapping (Figure 4C, 4D) as the pressure increases from 10.47 to 11.84 MPa, which somewhat resembles the crystallization morphological transition reflected in $P4VP_{8700}$/MWCNTs composite series with the difference in the helical wrapping patterns at higher pressures. At higher pressures, single helical wrappings of $P4VP_{8700}$ are formed on MWCNTs whereas a multi-helical $P4VP_{45000}$ structures are produced for $P4VP_{45\,000}$/MWCNTs composite.

The reasons for the multi-helical $P4VP_{45\,000}$ structures are possibly as follows. It is easy to understand that the polymer chain is longer for $P4VP_{45000}$

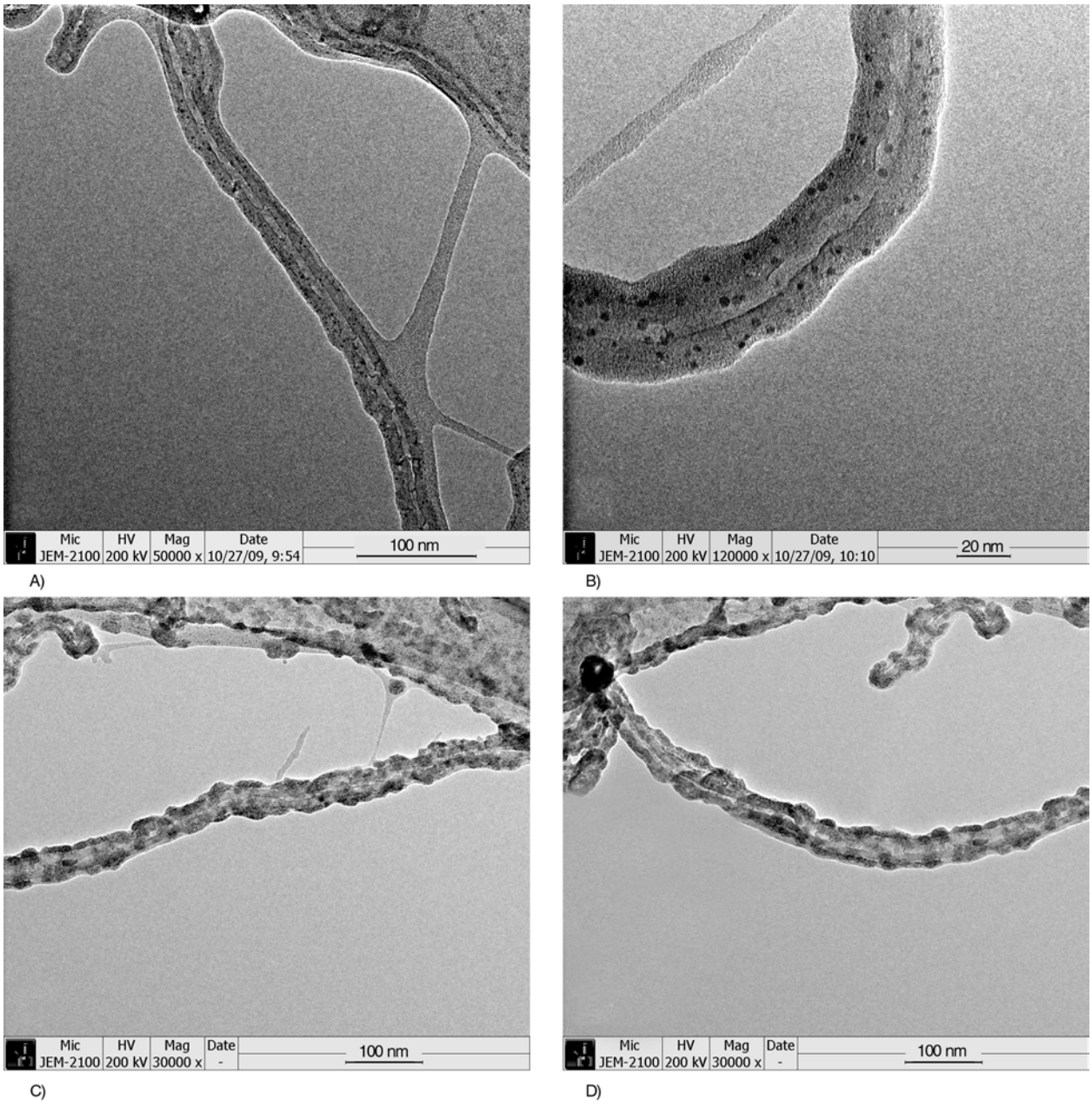

Figure 4. TEM images of $P4VP_{45000}$-decorated MWCNTs obtained in CO_2-expanded DMSO conditions (338.2 K/varied pressure for 3 h) and $P4VP_{45\,000}$ concentrations in DMSO (0.01 wt%), with MWCNTs concentrations of 0.002 wt%: (A)/(B) 10.47 MPa ($x_{CO_2} = 0.539$), (B) is the enlarged image of (A), (C)/(D) 11.84 MPa ($x_{CO_2} = 0.617$)

than that for $P4VP_{8700}$, thus both the solubility and the molecular mobility in DMSO are poorer for $P4VP_{45\,000}$ compared to $P4VP_{8700}$. It is generally believed that the amount of P4VP precipitation and the consequent number of nucleation are greatly increased with increasing pressure of CO_2 in $P4VP_{45\,000}$/MWCNTs system, so it is reasonable that multiple strands of the $P4VP_{45\,000}$ would coil around the MWCNTs and a multi-helical $P4VP_{45\,000}$ structures formed on MWCNTs rather than a simple helical crystallization for low molecular weight molecules as $P4VP_{8700}$.

3.3. Effect of P4VP Concentration on the modification of MWCNTs – polymer concentration dependence of crystal growth mechanism

From the aforementioned modification results using different MW-P4VPs under the same P4VP concentration, it seems that the wrapping morphologies for

the P4VP/MWCNTs composite with a LMW-P4VP matrix could be finely regulated in CXLs. So, in this section, the LMW-P4VP (i.e., $P4VP_{8700}$) is chosen to investigate the potential P4VP concentration dependence of MWCNTs modification.

The experimental conditions with higher P4VP concentration are that the $P4VP_{8700}$ (concentration 0.02 wt%) and MWCNTs (concentration 0.002 wt%) in DMSO were treated at 338.2 K and different pressures for 3 h, with pressures chosen to be 7.80 MPa (x_{CO_2} = 0.400), 9.31 MPa (x_{CO_2} = 0.477) and 11.58 MPa (x_{CO_2} = 0.602), respectively, along the bubble-point curve at 338.2 K in CO_2-DMSO [34]. The corresponding structures of $P4VP_{8700}$/

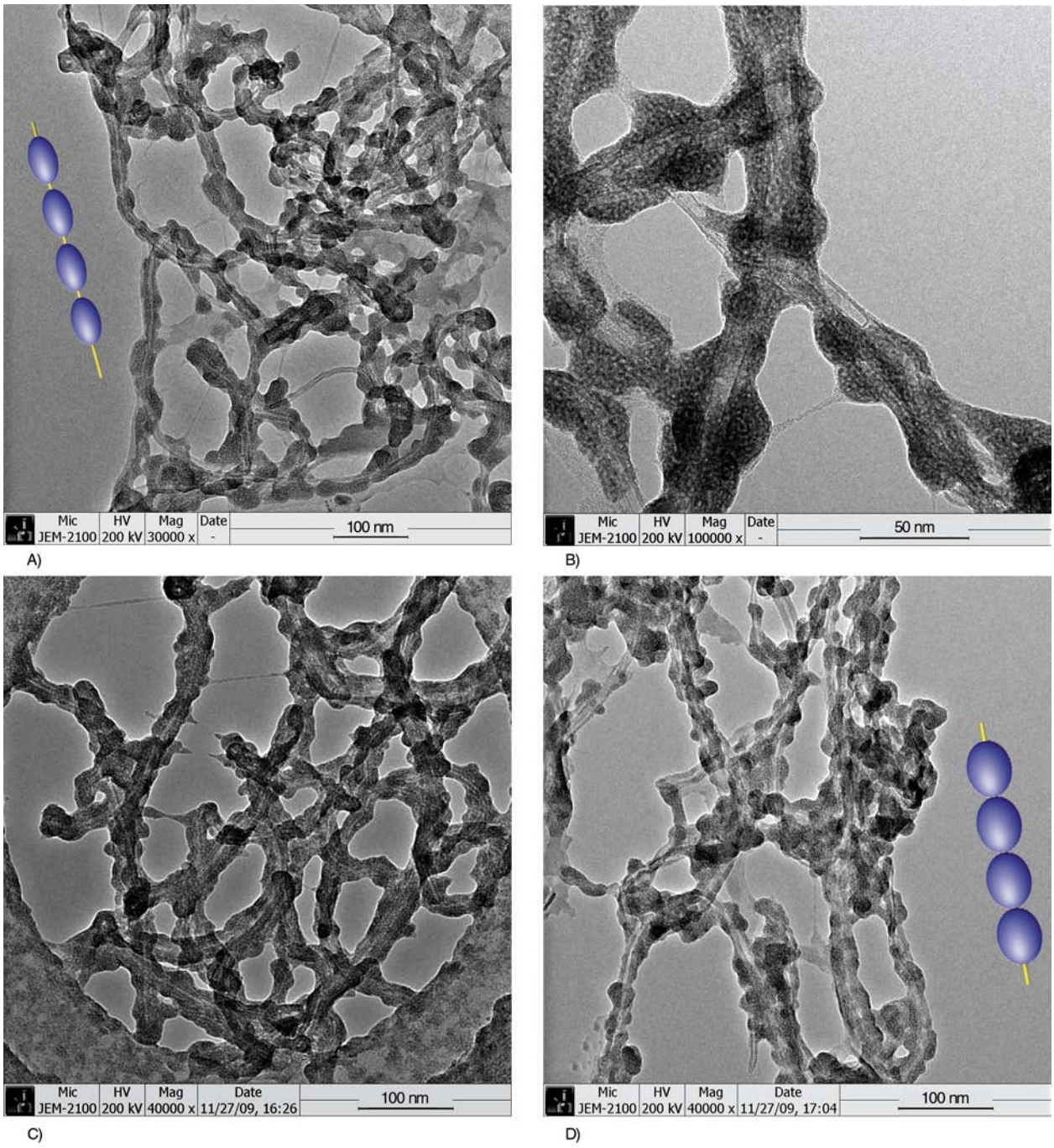

Figure 5. TEM images of $P4VP_{8700}$-decorated MWCNTs obtained in CO_2-expanded DMSO conditions (338.2 K/varied pressure for 3 h) and $P4VP_{8700}$ concentrations in DMSO (0.02 wt%), with MWCNTs concentrations of 0.002 wt%: (A) 7.80 MPa (x_{CO_2} = 0.400); (B) is the enlarged section of (A); (C) 9.31 MPa (x_{CO_2} = 0.477); (D) 11.58 MPa (x_{CO_2} = 0.602). There are schematic representations of the P4VP/MWCNTs NHSK structure on image (A) and (D), respectively, P4VP form kebab crystals on MWCNT surface with polymer chains parallel to the MWCNT axis.

MWCNTs at higher polymer concentration ($P4VP_{8700}$ 0.02 wt%) are shown in Figure 5A–5D, while the TEM images at lower polymer concentration ($P4VP_{8700}$ 0.01 wt%) are shown in Figure 3A–3D.

A nanohybrid shish-kebab (NHSK) like structure is observed from Figure 5: the central shish is MWCNTs, along the MWCNTs stems, round-shaped P4VP crystal kebabs can be regarded as periodically perpendicular to the stem axis. Typical NHSK structures have been observed in a number of labs [8, 9, 38]. The variation trend for the size of the kebab is indicated in Table 2: with the increase in pressure, it is found that while the size of the kebab increases, the periodicity of the kebab decreases. Actually, it can be seen from Table 2 that although a change in pressure can help adjust the modification of MWCNTs to some extent, the pressure effect is not so remarkable. In other words, although the P4VP wrapping degree on MWCNTs increases with increasing pressure, the pressure-dependent decoration effect is less notable at higher P4VP concentration.

The NHSK-like structure would suggest its formation mechanism. The orthogonal orientation between kebab surface and the MWCNT axis indicates that P4VP chains are parallel to the MWCNT axis. As mentioned previously, the epitaxial growth of P4VP on MWCNT and geometric confinement are two possible factors that affect NHSK growth. If the epitaxy factor dominates for all the MWCNTs, multiple orientation of the P4VP crystal lamellae should be observed, which is not supported by our results, indicating that 'soft epitaxy or geometric confinement' factor may predominate the NHSK formation, wherein strict lattice matching is not demanded while a cooperative orientation between the polymer chains and the MWCNT axes is required. Thus, when $P4VP_{8700}$ with higher polymer concentration starts to crystallize onto the surface of MWCNTs, geometric confinement is the major factor and the polymer chains are exclusively parallel to the MWCNT axis, disregarding the MWCNT chirality, and then the shish-kebab-like structures are formed herein [1].

People may wonder why the NHSK-like structures (Figure 5, $P4VP_{8700}$ concentration 0.02 wt%) instead of the helical morphology (Figure 3, $P4VP_{8700}$ 0.01 wt%) are formed in $P4VP_{8700}$/MWCNTs composite under higher P4VP concentration? It is suggested that the chain mobility (or molecular mobility) could also be vital in the formation of oriented crystal structure [39]. The P4VP concentration dependence of the formation of NHSK can be discussed on the basis of the chain mobility. Provided the same MW-P4VP and similar CXL conditions, in systems with higher P4VP concentration, the P4VP chain mobility should be weaker than that under lower P4VP concentration. It is predicted that under higher P4VP concentration with poorer polymer mobility, the P4VP chains prefer to be 'folded coiling' conformation rather than 'elongated coiling' conformation under lower concentration. That is, the 'folded coiling' P4VP chains prefer to soft-epitaxially grow into the kebabs (with kebab lamellae perpendicular to the MWCNT axis) under less mobile polymer conditions while the long coiled chains can be easily stretched to form helical wrappings with polymer chains oblique to the MWCNT-axis under lower polymer concentration. In other words, the evolution of the shish-kebab structure could be explained as the coil-stretch theory [39]. The helical wrapping forms when the polymer chains undergo a transition from a coiled conformation to a highly elongated state.

As to the variation trend for the size of the kebabs with pressure: with the pressure of CO_2 kept increasing, the amount and speed of CO_2 dissolved in DMSO increase and the solvent strength of DMSO becomes weaker; thus both the amount and the speed of P4VP precipitation can be greatly increased, and can induce the increase of the nucle-

Table 2. Size of the kebabs in the $P4VP_{8700}$/MWCNTs NHSK stucture produced with the $P4VP_{8700}$ (concentration 0.02 wt%) and MWCNTs (concentration 0.002 wt%) in CO_2-expanded DMSO at 338.2 K and different pressures: (A) and (B) 7.80 MPa (x_{CO_2} = 0.400); (C) 9.31 MPa (x_{CO_2} = 0.477); (D) 11.58 MPa (x_{CO_2} = 0.602)

Sample	Pressure [MPa]	Lateral size of the kebabs [nm]	Thickness of the kebabs [nm]	Periodicity of the kebabs [nm][a]
A and B	7.80	25–40	30–50	20–50
C	9.31	30–45	20–35	~0
D	11.58	40–50	20–30	~0

[a]Periodicity is defined as the distance between the adjacent kekab centers

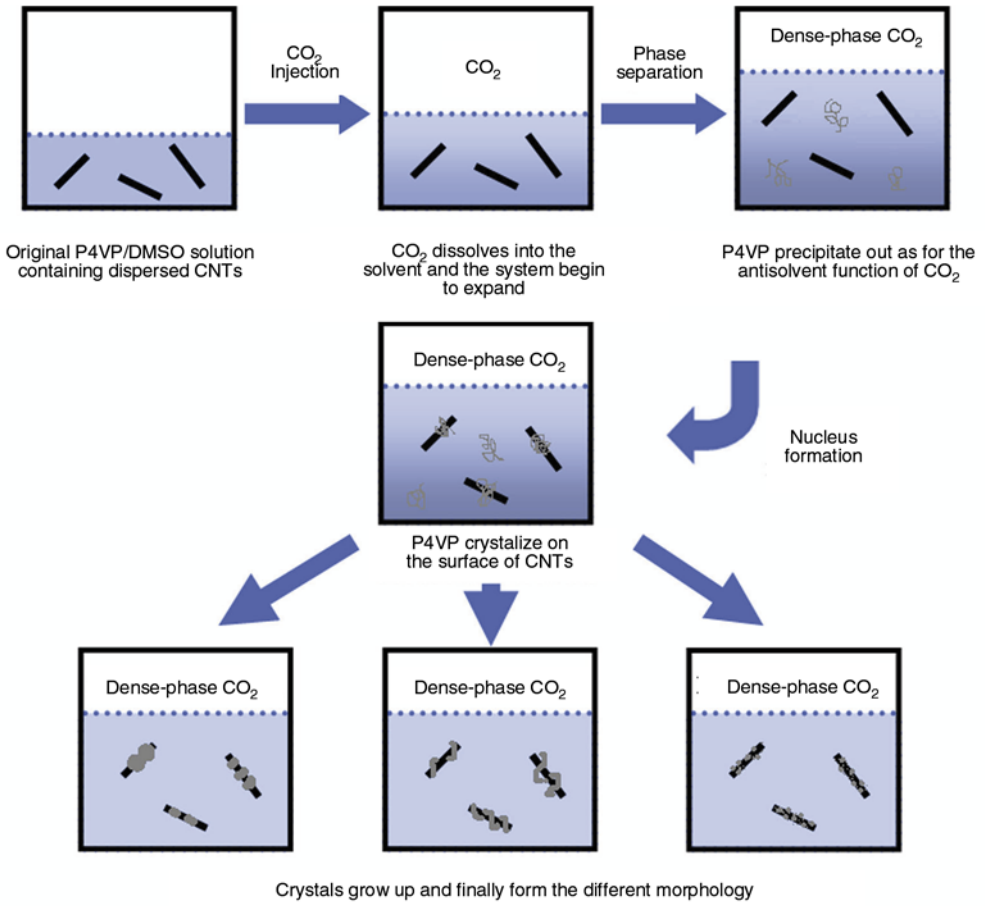

Figure 6. P4VP Crystallization on MWCNTs in CO_2-expanded liquids

ation number, which can lead to the formation of more kebabs. Therefore, both the size and the number of the kebabs would increase.

The suggested formation procedure is illustrated in Figure 6, which includes the initial nucleus and crystal growth to form helical or kebab structure in the later period.

3.4. The enhancement of MWCNTs dispersibility in DMSO

A photograph of samples dispersed in DMSO is shown in Figure 7. The three vials on the left contained MWCNTs (0.002 wt %) in DMSO, and the right three ones contained the samples of $P4VP_{8700}$ modified MWCNTs, with $P4VP_{8700}$ (0.02 wt%) and MWCNTs (0.002 wt%) in DMSO after reaction at 11.58 MPa (x_{CO_2} = 0.602) and 338.2 K for 3 h. From the images in Figure 7, we can observe that the MWCNTs precipitate easily in DMSO. The MWCNTs cannot disperse well in DMSO and start partially precipitating just 30 min after the ultrasonication (Figure 7B), whereas there is no obvious

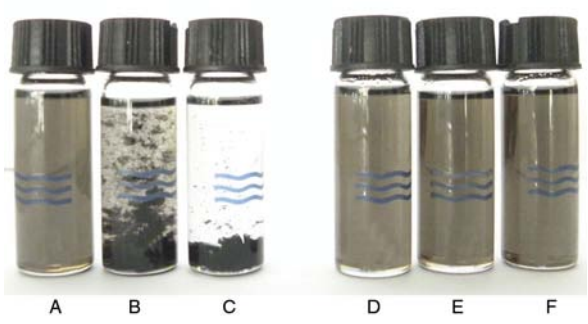

Figure 7. The three vials on the left contained MWCNTs (0.002 wt%) in DMSO. The right three ones contained $P4VP_{8700}$ modified MWCNTs in DMSO, with $P4VP_{8700}$ (0.02 wt%) and MWCNTs (0.002 wt%) in DMSO after reaction at 11.58 MPa (x_{CO_2} = 0.602) and 338.2 K for 3 h. First, all the samples were placed in the vials and ultrasonicated for 30 minutes, and the photographs were taken after the post-treatments on the samples as follows. (A) right after the ultrasonication; (B) 30 minutes after the ultrasonication; (C) 1 hour after the ultrasonication; (D) right after the ultrasonication; (E) after rotation at 4000 rpm for 5 minutes; (F) after rotation at 4000 rpm for 10 minutes.

aggregation in the P4VP modified MWCNTs under rotation at 4000 rpm for 10 minutes (Figure 7F). Obviously, the modified MWCNTs disperse well in DMSO. Here the solutions (Figures 7E, 7F) represent a good dispersion of MWCNTs/P4VP to form a stable system.

4. Conclusions

In conclusion, wrapping MWCNTs with amphiprotic polymer P4VP in CO_2 expanded DMSO was carried out. Firstly, about the pressure dependence of the MWCNTs modification: at lower polymer concentration ($P4VP_{8700}$ 0.01 wt%), the pressure of CXLs has a significant influence on the modification morphology. The morphological evolution of crystalline polymer on MWCNTs can be easily achieved by facile pressure tuning, wherein a structural evolution in $P4VP_{8700}$/MWCNTs composites was observed from dots to dotted helix, and then to dense helix; while at higher polymer concentration ($P4VP_{8700}$ 0.02 wt%), a NHSK-like structures rather than helical wrappings are obtained, the corresponding composite structure is only slightly pressure dependent; a less notable pressure dependence is also observed for $P4VP_{45000}$/MWCNTs, wherein a structural transition from dots to multi-helix was achieved with increasing pressure. Secondly, about the polymer concentration dependence of crystal growth mechanism: under higher polymer concentration ($P4VP_{8700}$ 0.02 wt%), the same MW-P4VP has different packing styles on the surface of MWCNTs and thus different crystal morphologies. The dominating crystal growth mechanism is attributed to 'soft epitaxy' at higher P4VP concentration rather than 'normal epitaxy' at lower concentration. Finally, comparative experiments of $P4VP_{8700}$ or $P4VP_{45\,000}$ decorated MWCNTs under the same experimental conditions free of CO_2 were also performed (the results are provided in Figure 2). From Figure 2, the wrapping pattern of P4VP on MWCNTs (in DMSO without CO_2) is found to be a simple coating style with film thickness about 1–2 nm and around 1–6 nm for $P4VP_{8700}$ and $P4VP_{45\,000}$, respectively. So, it is undoubtedly that the CXL method offers superior control of the P4VP crystallization patterns on MWCNTs in contrast with the conventional way.

We believe that the molecular weight, the concentration of P4VP as well as the pressure in GXLs are effective approaches to control the polymer crystallization structures on MWCNTs. The combination of desired pressure of CO_2 and MW-P4VP helps to modify the MWCNTs in a controllable way at suitable polymer concentration and temperature, which could serve as a model process to achieve ideal polymer crystals for structural and morphological study. Meanwhile, this work offers a new polymer wrapping approach in CXLs to noncovalent engineering of CNTs surfaces that leads to an enhancement of solubility or dispersibility of CNTs and enables superior control of the relative placement of functionalities on the CNT surface. The unique hybrid structure of P4VP/MWCNT nanocomposites would play a vital role in exploring and developing the potential applications of the corresponding PCNs.

Acknowledgements

This work was supported by funds from the National Natural Science Foundation of China (No.21073167 and No.J0830412), and the Scientific Research Foundation for the Returned Overseas Chinese Scholars, State Education Ministry of China (No.2008890).

References

[1] Li L.Y., Li B., Hood M. A., Li C. Y.: Carbon nanotube induced polymer crystallization: The formation of nanohybrid shish-kebabs. Polymer, **50**, 953–965 (2009).
DOI: 10.1016/j.polymer.2008.12.031

[2] Kharisov B. I., Kharissova O. V., Gutierrez H. L., Mendez U. O.: Recent advances on the soluble carbon nanotubes. Industrial and Engineering Chemistry Research, **48**, 572–590 (2009).
DOI: 10.1021/ie800694f

[3] Hirsch A.: Functionalization of single-walled carbon nanotubes. Angewandte Chemie-International Edition, **41**, 1853–1859 (2002).
DOI: 10.1002/1521-3773(20020603)41:11<1853::AID- ANIE1853>3.0.CO;2-N

[4] O' Connell M. J., Boul P., Ericson L. M., Huffman C., Wang Y. H., Haroz E., Kuper C., Tour J., Ausman K. D., Smalley R. E.: Reversible water-solubilization of single-walled carbon nanotubes by polymer wrapping. Chemical Physics Letters, **342**, 265–271 (2001).
DOI: 10.1016/S0009-2614(01)00490-0

[5] Chen J., Liu H. Y., Weimer W. A., Halls M. D., Waldeck D. H., Walker G. C.: Noncovalent engineering of carbon nanotube surfaces by rigid, functional conjugated polymers. Journal of the American Chemical Society, **124**, 9034–9035 (2002).
DOI: 10.1021/ja026104m

[6] Moniruzzaman M., Winey K. I.: Polymer nanocomposites containing carbon nanotubes. Macromolecules, **39**, 5194–5205 (2006).
DOI: 10.1021/ma060733p

[7] Winey K. I., Vaia R. A.: Polymer nanocomposites. Materials Research Society Bulletin, **32**, 314–319 (2007).

[8] Zhang Z. W., Xu Q., Chen Z. M., Yue J.: Nanohybrid shish-kebabs: Supercritical CO_2-induced PE epitaxy on carbon nanotubes. Macromolecules, **41**, 2868–2873 (2008).
DOI: 10.1021/ma702739n

[9] Zhang F., Zhang H., Zhang Z. W., Chen Z. M., Xu Q.: Modification of carbon nanotubes: Water-soluble polymers nanocrystal wrapping to periodic patterning with assistance of supercritical CO_2. Macromolecules, **41**, 4519–4523 (2008).
DOI: 10.1021/ma800514a

[10] Eckert C. A., Bush D., Brown J. S., Liotta C. L.: Tuning solvents for sustainable technology. Industrial and Engineering Chemistry Research, **39**, 4615–4621 (2000).
DOI: 10.1021/ie000396n

[11] Eckert C. A., Liotta C. L., Bush D., Brown J. S., Hallett J. P.: Sustainable reactions in tunable solvents. Journal of Physical Chemistry B, **108**, 18108–18118 (2004).
DOI: 10.1021/jp0487612

[12] Hallett J. P., Kitchens C. L., Hernandez R., Liotta C. L., Eckert C. A.: Probing the cybotactic region in gas-expanded liquids (GXLs). Accounts of Chemical Research, **39**, 531–538 (2006).
DOI: 10.1021/ar0501424

[13] Anand M., You S-S., Hurst K. M., Saunders S. R., Kitchens C. L., Ashurst W. R., Roberts C. B.: Thermodynamic analysis of nanoparticle size selective fractionation using gas-expanded liquids. Industrial and Engineering Chemistry Research, **47**, 553–559 (2008).
DOI: 10.1021/ie070981p

[14] Dehghani F., Foster N. R.: Dense gas anti-solvent processes for pharmaceutical formulation. Current Opinion in Solid State and Materials Science, **7**, 363–369 (2003).
DOI: 10.1016/j.cossms.2003.11.001

[15] Olesik S. V.: Physicochemical properties of enhanced-fluidity liquid solvents. Journal of Chromatography A, **1037**, 405–410 (2004).
DOI: 10.1016/j.chroma.2004.04.001

[16] Song I., Spuller M., Levitin G., Hess D. W.: Photoresist and residue removal using gas-expanded liquids. Journal of the Electrochemical Society, **153**, G314–G318 (2006).
DOI: 10.1149/1.2171824

[17] Wei M., Musie G. T., Busch D. H., Subramaniam B.: Autoxidation of 2,6-di-tert-butylphenol with cobalt Schiff base catalysts by oxygen in CO_2-expanded liquids. Green Chemistry, **6**, 387–393 (2004).
DOI: 10.1039/B310523G

[18] Lyon C. J., Sarsani V. R., Subramaniam B.: 1-Butene + isobutane reactions on solid acid catalysts in dense CO_2-based reaction media: Experiments and modeling. Industrial and Engineering Chemistry Research, **43**, 4809–4814 (2004).
DOI: 10.1021/ie0498145

[19] Jessop P. G., Subramaniam B.: Gas-expanded liquids. Chemical Reviews, **107**, 2666–2694 (2007).
DOI: 10.1021/cr040199o

[20] Wen F., Zhang W. Q., Wei G. W., Wang Y., Zhang J. Z., Zhang M. C., Shi L. Q.: Synthesis of noble metal nanoparticles embedded in the shell layer of core-shell poly(styrene-co-4-vinylpyridine) micospheres and their application in catalysis. Chemistry of Materials, **20**, 2144–2150 (2008).
DOI: 10.1021/cm703378c

[21] Yarapathi R. V., Kurva S., Tammishetti S.: Synthesis of 3,4-dihydropyrimidin-2(1H)ones using reusable poly(4-vinylpyridine-co-divinylbenzene)–Cu(II)complex. Catalysis Communications, **5**, 511–513 (2004).
DOI: 10.1016/j.catcom.2004.06.007

[22] Friedrich H. B., Singh N.: The very efficient oxidation of alcohols by poly(4-vinylpyridine)-supported sodium ruthenate. Tetrahedron Letters, **41**, 3971–3974 (2000).
DOI: 10.1016/S0040-4039(00)00531-1

[23] Jackson J. A., Newsham M. D., Worsham C., Nocera D. G.: Efficient singlet oxygen generation from polymers derivatized with hexanuclear molybdenum clusters. Chemistry of Materials, **8**, 558–564 (1996).
DOI: 10.1021/cm950443f

[24] Chen Y. S., Li Y., Yang M. J.: A fast response resistive thin film humidity sensor based on poly(4-vinylpyridine) and poly(glycidyl methacrylate). Journal of Applied Polymer Science, **105**, 3470–3475 (2007).
DOI: 10.1002/app.26401

[25] Rivas B. L., Quilodrán B., Quiroz E.: Trace metal ion retention properties of crosslinked poly(4-vinylpyridine) and poly(acrylic acid). Journal of Applied Polymer Science, **92**, 2908–2916 (2004).
DOI: 10.1002/app.20245

[26] El-Hamshary H., El-Garawany M., Assubaie F. N., Al-Eed M.: Synthesis of poly(acrylamide-co-4-vinylpyridine) hydrogels and their application in heavy metal removal. Journal of Applied Polymer Science, **89**, 2522–2526 (2003).
DOI: 10.1002/app.12305

[27] Caruso U., Centore R., Panunzi B., Roviello A., Tuzi A.: Grafting poly(4-vinylpyridine) with a second-order nonlinear optically active nickel(II) chromophore. European Journal of Inorganic Chemistry, **2005**, 2747–2753 (2005).
DOI: 10.1002/ejic.200400903

[28] Caruso U., De Maria A., Panunzi B., Roviello A.: Poly (4-vinylpyridine) as the host ligand of metal-containing chromophores for second-order nonlinear optical active materials. Journal of Polymer Science Part A: Polymer Chemistry, **40**, 2987–2993 (2002).
DOI: 10.1002/pola.10386

[29] Minko S., Kiriy A., Gorodyska G., Stamm M.: Single flexible hydrophobic polyelectrolyte molecules adsorbed on solid substrate: Transition between a stretched chain, necklace-like conformation and a globule. Journal of the American Chemical Society, **124**, 3218–3219 (2002).
DOI: 10.1021/ja017767r

[30] Kiriy A., Gorodyska A., Minko S., Jaeger W., Štěpánek P., Stamm M.: Cascade of coil-globule conformational transitions of single flexible polyelectrolyte molecules in poor solvent. Journal of the American Chemical Society, **124**, 13454–13462 (2002).
DOI: 10.1021/ja0261168

[31] Li Y., Yang M. J., She Y.: Humidity sensitive properties of crosslinked and quaternized poly(4-vinylpyridine-co-butyl methacrylate). Sensors and Actuators B: Chemical, **107**, 252–257 (2005).
DOI: 10.1016/j.snb.2004.10.008

[32] Aydogdu Y., Erol I., Yakuphanoğlu F., Aydogdu A., Ahmedzade M.: Electrical conductivity and optical properties of copolymers based on 4-vinylpyridine and tetralincyclobutylhydroxyethylmethacrylate. Synthetic Metals, **139**, 327–334 (2003).
DOI: 10.1016/S0379-6779(03)00183-8

[33] Tiller J. C., Lee S. B., Lewis K., Klibanov A. M.: Polymer surfaces derivatized with poly(vinyl-N-hexylpyridinium) kill airborne and waterborne bacteria. Biotechnology and Bioengineering, **79**, 465–471 (2002).
DOI: 10.1002/bit.10299

[34] Chiu H-Y., Jung R-F., Lee M-J., Lin H-M.: Vapor-liquid phase equilibrium behavior of mixtures containing supercritical carbon dioxide near critical region. Journal of Supercritical Fluids, **44**, 273–278 (2008).
DOI: 10.1016/j.supflu.2007.09.026

[35] Chalari I., Pispas S., Hadjichristidis N.: Controlled free-radical polymerization of 2-vinylpyridine in the presence of nitroxides. Journal of Polymer Science Part A: Polymer Chemistry, **39**, 2889–2895 (2001).
DOI: 10.1002/pola.1268

[36] Fischer A., Brembilla A., Lochon P.: Nitroxide-mediated radical polymerization of 4-vinylpyridine: Study of the pseudo-living character of the reaction and influence of temperature and nitroxide concentration. Macromolecules, **32**, 6069–6072 (1999).
DOI: 10.1021/ma990116j

[37] De Gennes P. G.: Coil-stretch transition of dilute flexible polymers under ultrahigh velocity gradients. Journal of Chemical Physics, **60**, 5030–5042 (1970).
DOI: 10.1063/1.1681018

[38] Zhang L., Tao T., Li C. Z.: Formation of polymer/carbon nanotubes nano-hybrid shish–kebab via non-isothermal crystallization. Polymer, **50**, 3835–3840 (2009).
DOI: 10.1016/j.polymer.2009.05.051

[39] Ning N. Y., Luo F., Wang K., Zhang Q., Chen F., Du R. N., An C. Y., Pan B. F., Fu Q.: Molecular weight dependence of hybrid shish kebab structure in injection molded bar of polyethylene/inorganic whisker composites. Journal of Physical Chemistry B, **112**, 14140–14148 (2008).
DOI: 10.1021/jp8056515

eXPRESS Polymer Letters Vol.5, No.1 (2011) 73–81
Available online at www.expresspolymlett.com
DOI: 10.3144/expresspolymlett.2011.8

Transflective multiplexing of holographic polymer dispersed liquid crystal using Si additives

K. R. Sun[1], *Y. S. Kang*[2], *B. K. Kim*[1*]

[1]Department of Polymer Science and Engineering, Pusan National University, Busan 609-735, Korea
[2]Department of Chemistry, Sogang University, Seoul 121-741, Korea

Received 29 June 2010; accepted in revised form 18 September 2010

Abstract. Morphology, grating formation dynamics and electro-optical performance of transflective multiplexing with holographic polymer dispersed liquid crystal (HPDLC) were investigated in the presence of silica nanoparticles (Aerosil R812 (RS) and modified Aerosil 200 (MS)) and silicon monomer (vinyltrimethoxy silane (VTMS)) by using three coherent laser beams. The addition of Si additive significantly augmented the diffraction efficiencies of transmission and reflection gratings due to the enhanced phase separation with large LC channels. The film was driven only with Si additives which are enriched at the polymer-LC interfaces. As the additive content increased, driving voltage decreased to a minimum of 30 V at 2.0 wt% VTMS. It was found that the interface modification and large droplet size are crucial to operate the film. Among the three types of Si additive, VTMS showed the highest electro-optical performance due to its low viscosity and high reactivity.

Keywords: *nanocomposites, multiplexing, HPDLC, transflective grating, silica*

1. Introduction

The development of an optimum recording material remains one of the principal challenges in the area of holographic data storage [1–3]. Holographic photopolymers, first reported in the late 1960s by Close *et al*. [4], are attractive candidates for applications in data storage [5–7] though they have limited memory capacity at this moment.

Holographic storage has long been the promise for large digital storage capacity because the information packing densities can be considerably increased by using three-dimensional storage techniques [8, 9]. Various kinds of recording configurations have been proposed for this purpose [10, 11]. In general, these methods require an independent specific reference beam to interfere with the object beam to perform the recording.

Holographic storage also enables fast data transfer because it permits reading and writing of data simultaneously. There are a number of multiplexing schemes to store many holograms in the same volume such as angular [12–15], peristrophic [16, 17], shift multiplexing [18, 19] or by more than one of these techniques in combination [20–22], which are used to store multiple holograms at the same location. In these methods, angular multiplexing is probably the most common in which the reference beam is incident upon the sample at difference angle to record each hologram. However, earlier studies showed relatively low and non-uniform diffraction efficiency of each multiplexed hologram.

In this paper, we propose a high and uniform efficiency holographic storage system with three coherent laser beams for transflective multiplexed

*Corresponding author, e-mail: bkkim@pnu.edu

HPDLC using angular multiplexing method. To obtain high and uniform diffraction efficiency, we incorporated various amounts of silica nanoparticles, virgin and chemically modified ones, and silicon monomer which have high refractive index and low free energy into the polymer matrix. These HPDLC films are also expected to lower the driving voltage and the response time in addition to the enhanced diffraction efficiency.

2. Experimental

2.1. Materials

The typical recipe for writing HPDLC gratings consists of multi-functional monomer (oligomers), reactive diluents, additives, and LC in the presence of suitable photoinitiator dye and coinitiator.

To synthesize urethane oligomers, a molar excess of hexane diisocyanate (HDI, Aldrich, St. Louis, America) (molecular weight = 168.20 g·mol^{-1}) was reacted with bifunctional polypropylene glycol (PPG, Korea Polyols, Korea) (M_n = 400 g·mol^{-1}) for over 1 h at 80°C to obtain NCO-termination. Then the reaction mixture was cooled down to 40°C and 2-hydroxylethyl acrylate (HEA, Aldrich, St. Louis, America) (molecular weight = 116.12 g·mol^{-1}) was added to obtain HEA-capped urethane acrylate oligomer (called oligomer) having a molecular weight of 968.64 g·mol^{-1}.

The oligomers are highly viscous and immiscible with LCs, which necessitates the use of reactive diluents. Two types of reactive diluents, viz. N-vinylpyrrollidinone (NVP, Aldrich, St. Louis, America) and dipentaerythritol penta-/hexa-acrylate (DPHPA, Aldrich, St. Louis, America) were used and the composition of oligomer/monofunctional/multifunctional diluents was 4:3:3 by weight.

In addition, silica nanoparticles (Aerosil R812 (RS), Degussa, Canada, diameter = 7 nm), vinyl modified Aerosil 200 (MS, Degussa, Canada, diameter = 12 nm), and silicon monomer (vinyltrimethoxy silane (VTMS), Aldrich, St. Louis, America) (hereafter called Si additive) have been added to the mixture. VTMS is a liquid at ambient conditions and it reduces the mixture viscosity significantly. Silica nanoparticles and VTMS were obtained from Degussa and Aldrich respectively. The LC used in our experiment was E7 (BL001, Merck, Germany), an eutectic mixture of four cyanobiphenyl and cyanoterphenyl mixture with T_{NI} = 50.5°C, ε = 19.0, and $\varepsilon_{\perp}$ = 4.2. Rose Bengal was used as photo-initiator for holographic recording with Ar-ion laser (λ = 514 nm), where N-phenylgycine was added as co-initiator. The prepolymer/LC composition was 65/35. Basic formulations are shown in Table 1.

2.2. Modification of silica particles

Aerosil 200 were first dispersed in DMF, followed by mixing and reaction with allyl isocyanate for 24 h at 80°C to obtain the vinyl modified silica particles (Figure 1). Then the sample was filtered and washed with acetone.

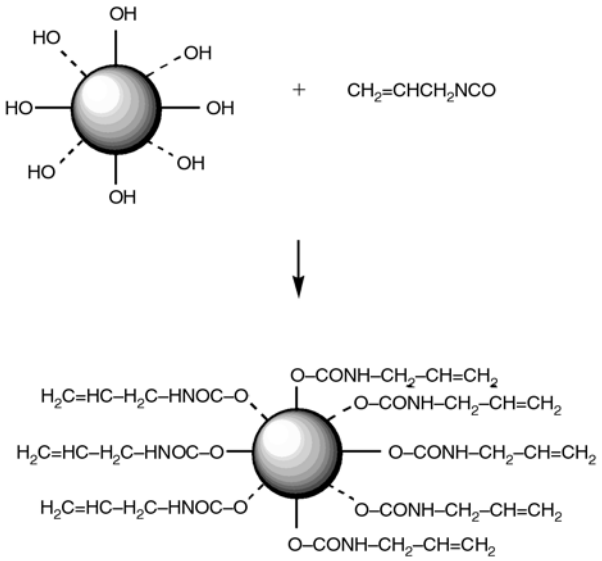

Figure 1. Reaction scheme to modify the Aerosil 200 with allyl isocyanate

Table 1. Formulations to fabricate HPDLC films

Composition[wt%]								
Oligomer	Diluents		Initiator		Additive			LC
PPG400 HDI HEA	DPHPA	NVP	RB	NPG	RS	MS	VTMS	E7
63.63			0.20	1.17	None	None	None	35
63.37					0.26	0.26	0.26	
63.11					0.52	0.52	0.52	
62.85					0.78	0.78	0.78	
62.59					1.04	1.04	1.04	
62.33					1.30	1.30	1.30	
65.00								35

2.3. Grating preparation and measurements

Figure 2 shows the multiplexed holographic recording system. An Ar-ion laser (514 nm) with a total power of 150 mW/cm^2 was used as light source. Relative intensities of the three beams were 10 (B2)/5 (B1, reference beam)/5 (B3). These three beams were reflected from the mirrors and then impinged on the cell from the same and the different side of the cell. The cell was constructed by sandwiching the oligomer/LC mixture between the two indium tin oxide (ITO) coated glass cells, with a gap of 10 μm, adjusted by a bead spacer. The interference of the three beams established the periodic interference pattern according to Bragg's law. The two intersections between the reference (B1) and object beams (B2, B3) were respectively set at 22° and at 180°. Powder samples for infrared (PerkinElmer, New York, America) and H-NMR (Varian, New York, America) measurements were prepared after evaporating the solvent used for modification of silica particles.

The diffraction efficiencies of the holographic gratings were measured with a photo-diode using Ar-ion laser. The transmitted beams and reflected beams were detected with a photodiode detector. Diffraction efficiency is defined as the ratio of diffraction intensity after plate divided by the transmitted beam intensity before plate. Real time grating formation was monitored using He-Ne laser probe (633 nm) since the material is not sensitive to red light. UV-visible spectra of unfilled (virgin) and additive filled resins were determined using a UV-visible spectrophotometer (Mecasys Optizen, Korea) at ambient temperature. The baseline was drawn with blank cell of glass substrate.

For electrooptic measurements, a square wave voltage (60 Hz sine wave pulse of 50 ms) operating from 0 to 50 V was applied across the HPDLC cell. The drive signal and the response of the photodiode were monitored with a digital storage oscilloscope (Hitachi VC-6023, Japan). The response time is defined as the time taken to relax from 90 to 10% of the maximum switching difference under an electric field.

LC was extracted in methanol for 24 h before the morphology was examined under the scanning electron microscopy (SEM, Hitachi S430, Japan). Samples were fractured in liquid nitrogen and the fractured structures were scanned. The contact angle with an LC drop was measured on the surface of polymer cured with UV radiation for about 10 min with 0.1 wt% 1-hydroxy-2-methyl-1-phenylpropan-1-one (Darocur1173, Ciba Specialty Chemicals, Switzerland) as an initiator using a contact angle meter (G-1, Erma).

3. Results and discussion

3.1. FT-IR and ^{1}H-NMR

The structure of vinyl modified silica (Figure 1) was confirmed by FT-IR and ^{1}H-NMR measurements in Figure 3. The IR spectra of modified one show the characteristic peaks of the NH group (3338 cm^{-1}), C=C group (1628 cm^{-1}) and CNH group (1580 cm^{-1}) which are formed by the urethane forming reactions (Figure 3a). In the ^{1}H-NMR spectra (Figure 3b), signals from 5.89 to 5.83 ppm are assigned to the protons of CH and CH_2 (vinyl group), and those at 5.28 and 3.99 ppm are assigned to the protons of CH_2 and NH. These

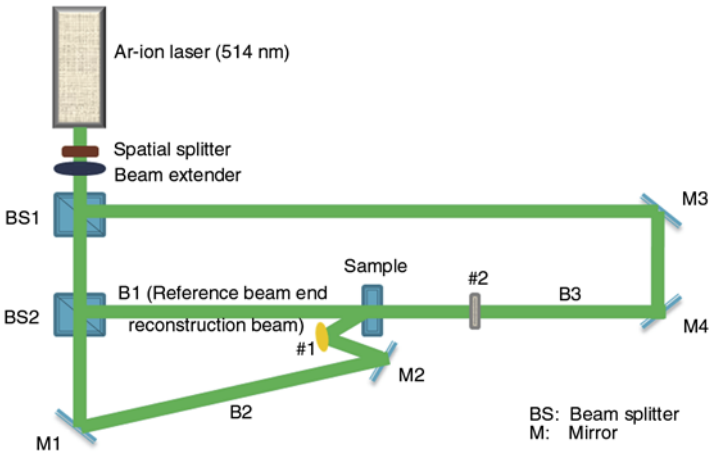

Figure 2. Optical set up for fabrication of transflective HPDLC films

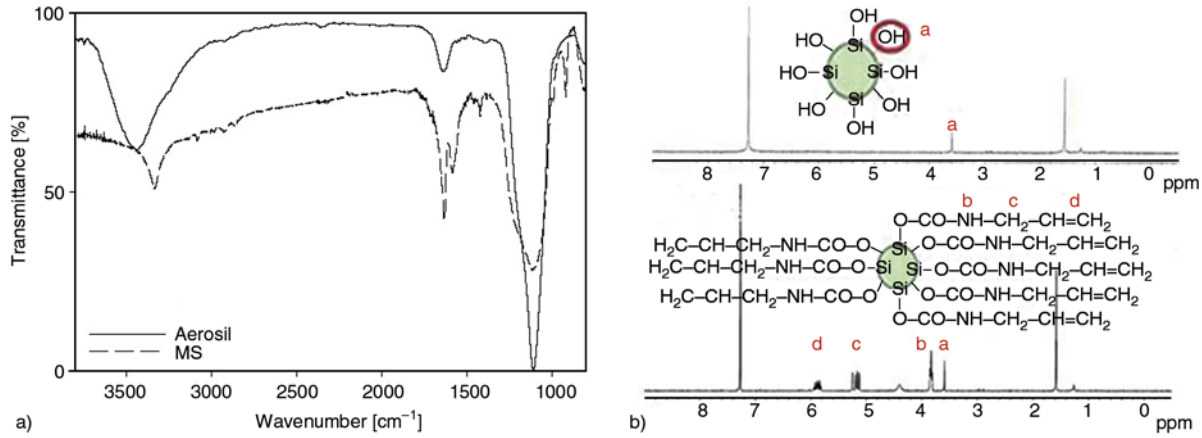

Figure 3. (a) FT-IR spectra and (b) ^{1}H-NMR Spectrum of virgin Aerosil 200 particles and after reaction with allyl isocyanate

results confirm the incorporation of allyl isocyanate onto the silica surfaces.

3.2. Contact angle

The contact angle of the film with an LC drop increased monotonically with the addition and increasing amount of Si additive (Figure 4). This implies that the additives are preferentially migrated toward the surface due to the immiscibility and lower free energy of silicon atom. Notably, the effect was increasing along RS<MS<VTMS, where migration of VTMS was favored by its high diffusivity as liquid. An implication of the results is that silicon atoms are effectively exposed to the polymer-LC interfaces and reduce the anchoring energies of LC molecule on polymer surface along with reduced driving voltage as well [5].

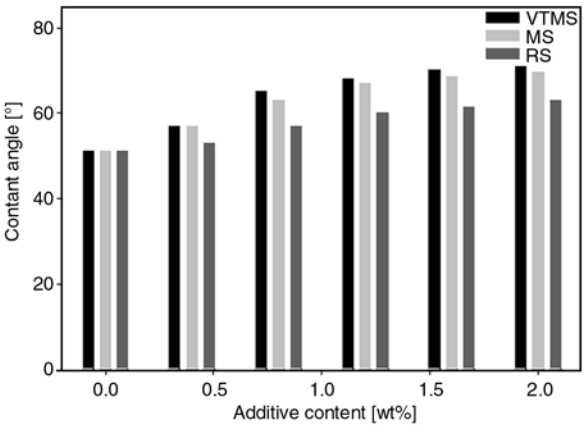

Figure 4. Contact angle of polyurethane acrylate film with an LC drop

3.3. SEM morphology

Typical multiplexed gratings at 3K expansion are shown with 0.4 wt% MS in Figure 5. One reference beam (B1) and two object beams (B2, B3) generated three gratings. Vertical transmission grating (G12) formed by B1 and B2, and slanted reflection grating (G13) formed by B1 and B3 are seen from the top view. A third reflection grating (G23) formed by B2 and B3 is also seen from the edge view, where the edge is parallel to B1.

Figure 6, 7 and 8 respectively show the grating morphology at much high expansion (40K) for various contents of RS, MS and VTMS. Regardless of additive type, the width of LC channel increased with the addition and increasing amount of additive. The increase is presumably due to the increased resin phase elasticity which effectively squeezes the LC out of the resin phase to form a large LC chan-

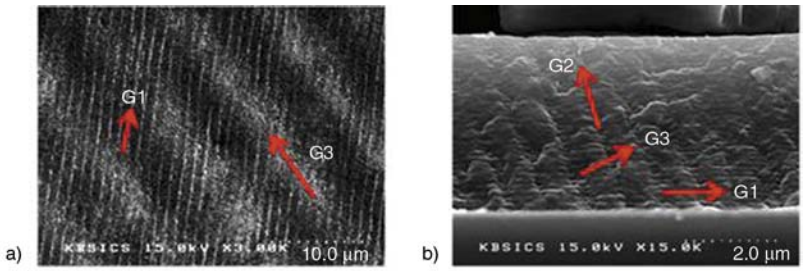

Figure 5. SEM micrographs of multiplexed gratings: (a) top view and (b) edge view

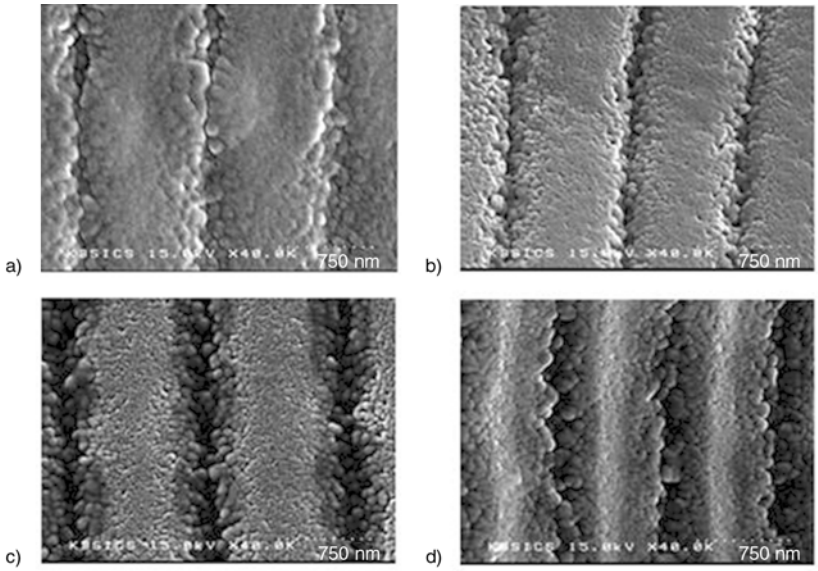

Figure 6. SEM micrographs of HPDLC films prepared (a) without, (b) with 0.4, (c) 1.2 and (d) 2.0 wt% RS

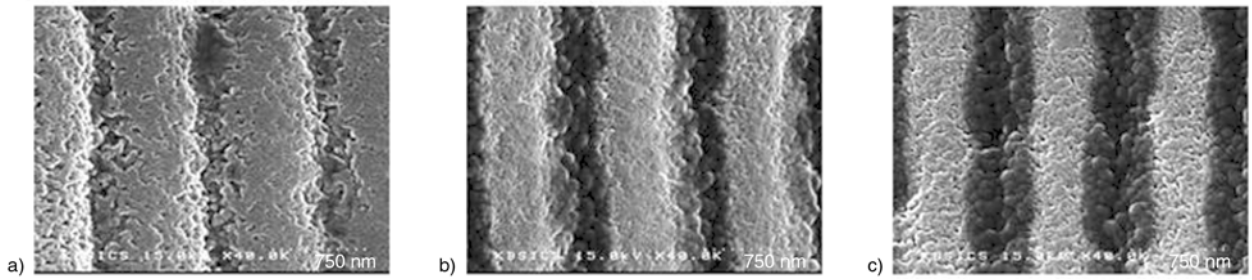

Figure 7. SEM micrographs of HPDLC films prepared (a) with 0.4, (b) 1.2 and (c) 2.0 wt% MS

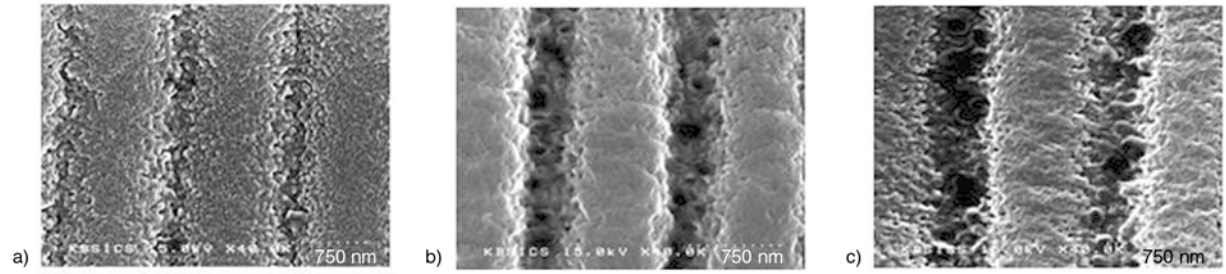

Figure 8. SEM micrographs of HPDLC films prepared (a) with 0.4, (b) 1.2 and (c) 2.0 wt% VTMS

nel [7]. However, the effect is less pronounced with smaller particle (RS) since viscosity hinders diffusion. Increased phase separation should give high diffraction efficiency to follow. LC droplets which are not squeezed out of and remaining on the resin phase are larger for RS and smaller for MS. Resin surfaces are much smooth with VTMS due both to the homogeneous nature of resin phase and enhanced phase separation.

3.4. Diffraction efficiency

3.4.1. Real-time diffraction efficiency

With the addition and increasing amount of silica particles (RS, MS) nucleation and growth of periodic modulation are delayed followed by delayed saturation, more with RS and less with MS (Figure 9). This is due to the increased viscosity of the resin phase, which is greater with smaller particle (RS) [7]. Diffraction maximum is observed when the particle content is high. At this composition, elasticity driven phase separation is seemingly balanced with viscosity increase.

In contrast, VTMS induces nucleation faster than the virgin resin and gives much greater maximum and saturation diffraction than the RS and MS as well as virgin resin. It seems that the lower viscosity of VTMS inclusion drives fast diffusion, fast reaction, fast grating formation and phase separa-

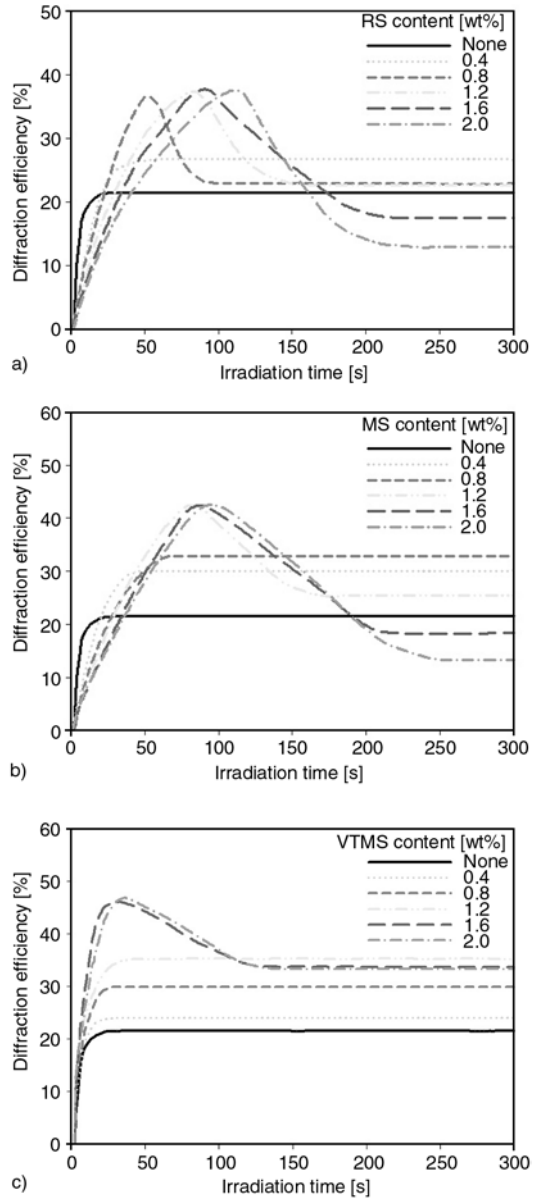

Figure 9. Real-time diffraction efficiency at various silica contents of HPDLC films prepared using (a) RS, (b) MS and (c) VTMS

tion. Greater phase separation with VTMS was seen from the clean surface of resin phase (Figure 8 as compared with those of RS and MS (Figures 5 and 6).

3.4.2. Diffraction efficiency

Figure 10 shows diffraction efficiency of preferred gratings (G12, G13). As expected, diffraction efficiency of the multiplexed gratings is smaller than the conventional HPDLC system. This indicates that two different gratings which are simultaneously formed with three beams disturb the formation of the other [23]. However, it is mentioned that the two gratings give similar diffraction efficiencies of about 35 (G12) and 22% (G13) though no exposure time scheduling has been used [20, 22].

Diffraction efficiency shows a maximum at 0.8 (RS, MS) or 1.2 wt% (VTMS) due to the enhanced phase separation [24]. For RS and MS the decrease after the maximum is due to the particle agglomeration [3]. The agglomeration is less with MS than with RS due to the chemical modification and incorporation of MS into the polymer matrix. For VTMS, extensive coalescence of LC droplets through less viscous matrix at higher silica contents led to high scattering loss giving small diffraction efficiency.

3.5. Image recording and reconstruction

Figure 11 show the original object patterns and their corresponding images as retrieved by reference beam. It is seen that the three retrieved images are fairly clear. The coin image (#1 in Figure 2) was recorded by transmission grating using B1 and B2, whereas mosaic pattern (#2 in Figure 2) by reflection grating using B1 and B3.

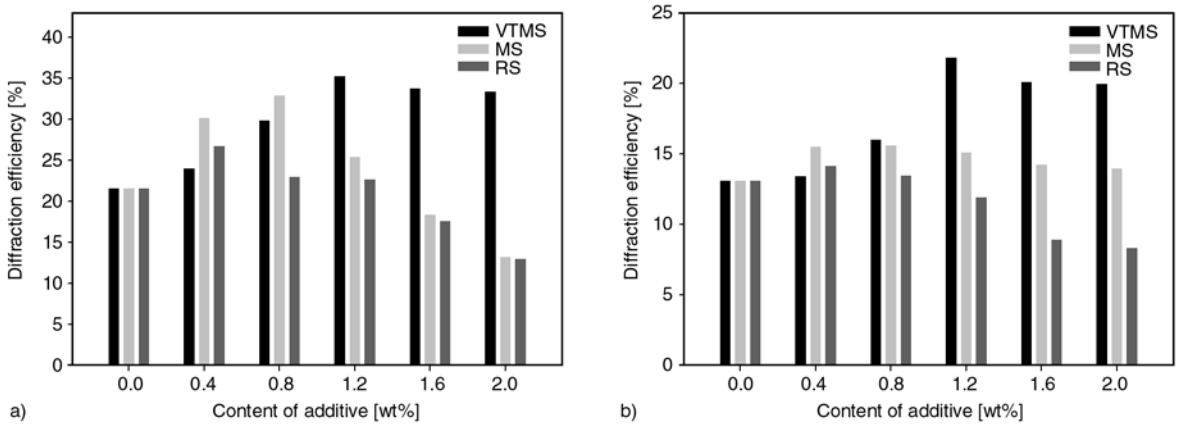

Figure 10. (a) Diffraction efficiency (R1) and (b) reflection efficiency (R2) vs. additive type and content of the holographic gratings

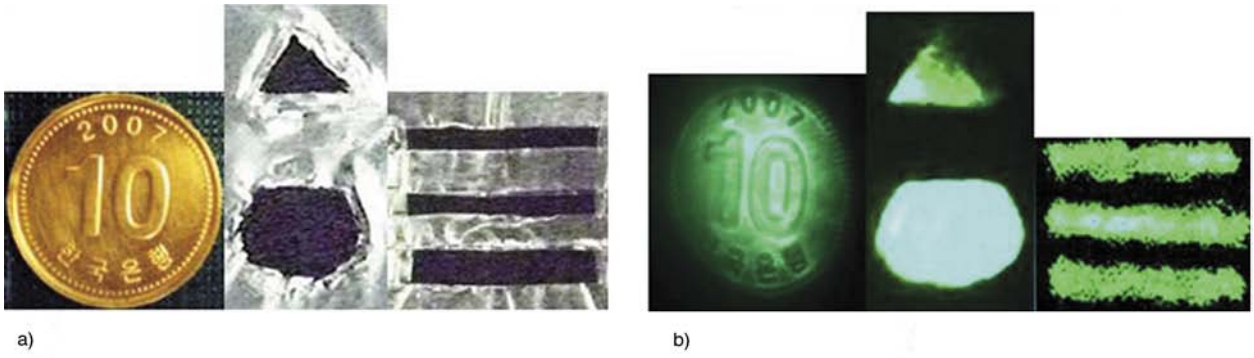

Figure 11. Original object patterns (the top row) multiplexed in different angles, and their corresponding retrieved images (the bottom row)

3.6. Electrical properties

3.6.1. Driving voltage

Figure 12 shows the driving voltage of HPDLC films. The virgin HPDLC film with no silica was not driven due to the strong anchoring strength between the polymer and LC [5]. It is seen that the film was driven only with silica particles and the switching voltage decreased with increasing amount of silica, where the lowest driving voltage of about 30 V was obtained at 2.0 wt% VTMS.

The presence of silicon atoms at the polymer-LC interfaces decreased interface energy to lower the surface anchoring and influenced the orientation of LC droplet directors. Regarding the effect of additive type, driving voltage decreased along the order of RS>MS>VTMS.

Due to the photo-reactivity of VTMS and MS, these groups are incorporated into the chain end of polymer, and are preferentially exposed to the polymer-LC interfaces. Among the two, VTMS having high reactivity and low viscosity is expected to be enriched more at the interfaces to give a dramatically decreased driving voltage.

3.6.2. Response time

Typical temporal response of a HPDLC film was measured at a particular composition of 0.8 wt% (Figure 13). Rise time was small (0.28–0.34 ms) while the decay time decreased along RS (1.92)> MS (1.82)>VTMS (1.28 ms). The additives which are interposed at the polymer-LC interfaces not only decrease the surface anchoring but also influence the orientation of LC droplet directions [25]. It seems that VTMS is a preferred interface modifier among the three.

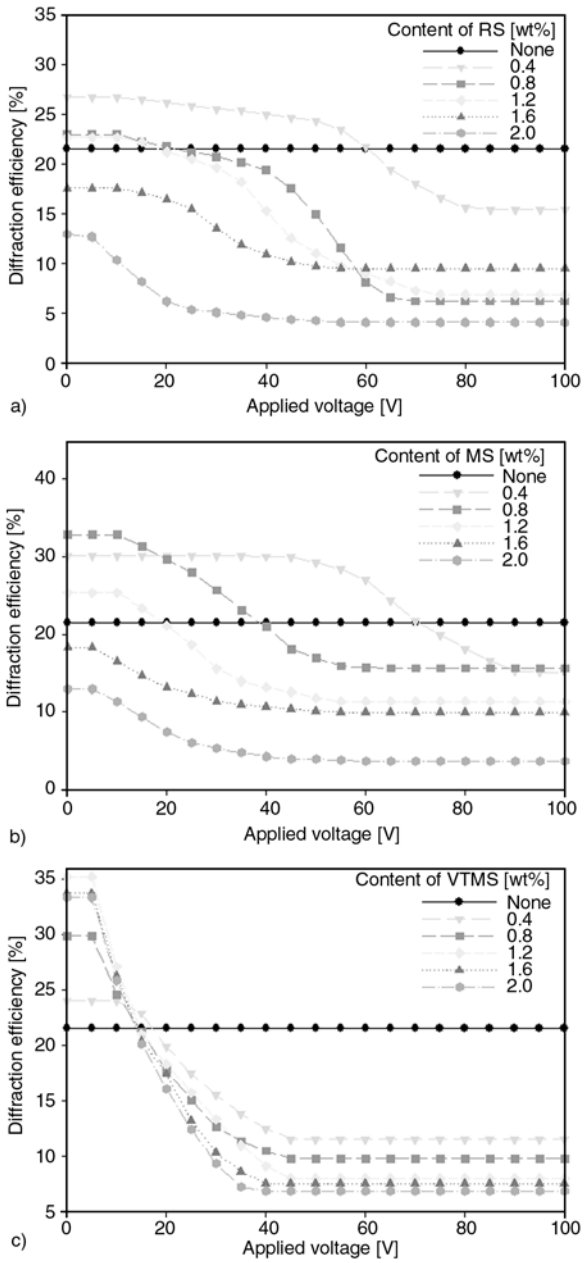

Figure 12. Diffraction efficiency versus applied voltage at various silica contents of HPDLC films prepared using (a) RS, (b) MS and (c) VTMS

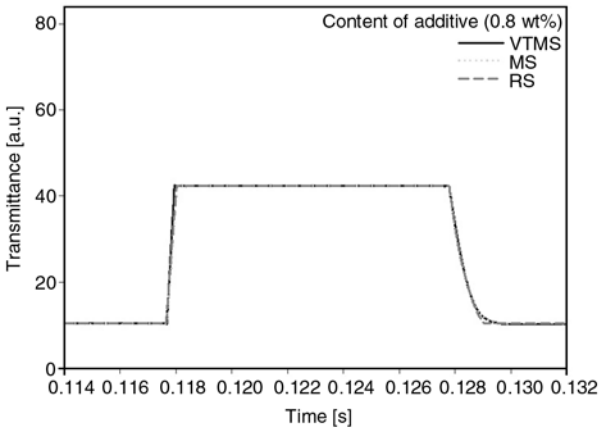

Figure 13. Temporal response of the films as a function of the silica types (at 0.8 wt% additive)

4. Conclusions

Silica nanoparticles and silicon monomer have been introduced into the conventional formulation to fabricate angular multiplexed holographic polymer dispersed liquid crystal (HPDLC) and the effects have been studied in terms of grating formulation dynamics, morphology, diffraction efficiency, and electro-optical properties of the films.

The addition of Si additives significantly augmented the diffraction efficiencies of transmission and reflection gratings of the HPDLC. This was attributed to the enhanced phase separation with a large LC channel.

The film was driven only with Si additives which are enriched at the polymer-LC interfaces by the low free energy of silicon containing compounds to decrease the anchoring strength of LC molecule on polymer wall. As the additive content increased, driving voltage decreased to a minimum of 30 V at 2.0 wt% VTMS. It was concluded that the polymer-LC interface modification and large droplet size are crucial to operate the film.

Regarding the effect of additive type, the highest electro-optical performances such as diffraction efficiency, driving voltage and response time were obtained with VTMS due to its low viscosity and high reactivity with the polymer matrix.

Acknowledgements

The research has been supported by the NCRC and PNU-IFAM JRC Programs both organized at PNU.

References

[1] Haw M.: Holographic data storage: The light fantastic. Nature, **422**, 556–558 (2003). DOI: 10.1038/422556a

[2] Zilker S. J.: Holographic data storage – The materials challenge. ChemPhysChem, **3**, 333–334 (2002). DOI: 10.1002/1439-7641(20020415)3:4<333::AID-CPHC333>3.0.CO;2-W

[3] Del Monte F., Martínez O., Rodrigo J. A., Calvo M. L., Cheben P.: A volume holographic sol-gel material with large enhancement of dynamic range by incorporation of high refractive index species. Advanced Materials, **18**, 2014–2017 (2006). DOI: 10.1002/adma.200502675

[4] Close D. H., Jacobson A. D., Margerum J. D., Brault R. G., McClung F. J.: Hologram recording on photopolymer materials. Applied Physics Letters, **14**, 159/1–159/2 (1969). DOI: 10.1063/1.1652756

[5] Woo J. Y., Kim E. H., Kim B. K.: Transmission holographic polymer dispersed liquid crystals based on a siloxane polymer. ChemPhysChem, **9**, 141–146 (2008). DOI: 10.1002/cphc.200700521

[6] Poque R. T., Natarajan L. V., Siwecki S. A., Tondiglia V. P., Sutherland R. L., Bunning T. J.: Monomer functionality effects in the anisotropic phase separation of liquid crystals. Polymer, **41**, 733–741 (2000). DOI: 10.1016/S0032-3861(99)00196-2

[7] Kim E. H., Woo J. Y., Kim B. K.: Nanosized-silica-reinforced holographic polymer-dispersed liquid crystals. Macromolecular Rapid Communications, **27**, 553–557 (2006). DOI: 10.1002/marc.200500784

[8] Das B., Joseph J., Singh K.: Phase modulated gray-scale data pages for digital holographic data storage. Optics Communications, **282**, 2147–2154 (2009). DOI: 10.1016/j.optcom.2009.02.048

[9] Gu C., Xu Y., Liu Y., Pan J. J., Zhou F., He H.: Applications of photorefractive materials in information storage, processing and communication. Optical Materials, **23**, 219–227 (2003). DOI: 10.1016/S0925-3467(02)00293-8

[10] Shahar R., Weiner S.: Insights into whole bone and tooth function using optical metrology. Journal of Materials Science, **42**, 8919–8933 (2007). DOI: 10.1007/s10853-007-1693-8

[11] Jeong E. H., Sun K. R., Kang M. C., Jeong H. M., Kim B. K.: Memory effect of polymer dispersed liquid crystal by hybridization with nanoclay. Express Polymer Letters, **4**, 39–46 (2010). DOI: 10.3144/expresspolymlett.2010.7

[12] Yau H-F., Liu J-P.: Angle multiplexed storage with object beam alone. Applied Physics Letters, **90**, 181916/1–181916/3 (2007). DOI: 10.1063/1.2733629

[13] Ortuño M., Gallego S., García C., Neipp C., Beléndez A., Pascual I.: Optimization of a 1 mm thick PVA/acrylamide recording material to obtain holographic memories: Method of preparation and holographic properties. Applied Physics B, **76**, 851–857 (2003). DOI: 10.1007/s00340-003-1229-0

[14] Sherif H., Naydenova I., Martin S., McGinn C.: Characterization of an acrylamide-based photopolymer for data storage utilizing holographic angular multiplexing. Journal of Optics B, **7**, 255–260 (2005). DOI: 10.1088/1464-4258/7/5/007

[15] El Hafidi I., Grzymala R., Kiefer R., Elouad L., Meyrueis P.: Optical data storage on protein using angular multiplexing. Optics and Laser Technology, **37**, 503–508 (2005). DOI: 10.1016/j.optlastec.2004.06.008

[16] Mok F. H., Tackitt M. C., Stoll H. M.: Storage of 500 high-resolution holograms in a $LiNbO_3$ crystal. Optics Letters, **16**, 605–607 (1991). DOI: 10.1364/OL.16.000605

[17] Curtis K., Pu A., Psaltis D.: Method for holographic storage using peristrophic multiplexing. Optics Letters, **19**, 993–994 (1994). DOI: 10.1364/OL.19.000993

[18] Pu A., Curtis K., Psaltis D.: Exposure schedule for multiplexing holograms in photopolymer films. Optical Engineering, **35**, 2824–2829 (1996). DOI: 10.1117/1.600967

[19] Steckman G. J., Pu A., Psaltis D.: Storage density of shift-multiplexed holographic memory. Applied Optics, **40**, 3387–3394 (2001). DOI: 10.1364/AO.40.003387

[20] Rakuljic G. A., Levya V., Yariv A.: Optical data storage by using orthogonal wavelength-multiplexed volume holograms. Optics Letters, **17**, 1471–1473 (1992). DOI: 10.1364/OL.17.001471

[21] Fernández E., García C., Pascual I., Ortuño M., Gallego S., Beléndez A.: Optimization of a thick polyvinyl alcohol-acrylamide photopolymer for data storage using a combination of angular and peristrophic holographic multiplexing. Applied Optics, **45**, 7661–7666 (2006). DOI: 10.1364/AO.45.007661

[22] Sheridan J. T., O'Neill F. T., Kelly J. V.: Holographic data storage: Optimized scheduling using the nonlocal polymerization-driven diffusion model. Journal of the Optical Society of America B, **21**, 1443–1451 (2004). DOI: 10.1364/JOSAB.21.001443

[23] Gallego S., Neipp C., Ortuño M., Fernández E., Beléndez A., Pascual I.: Analysis of multiplexed holograms stored in a thick PVA/AA photopolymer. Optics Communications, **281**, 1480–1485 (2008). DOI: 10.1016/j.optcom.2007.11.068

[24] Bowely C. C., Fontecchio A. K., Crawford G. P.: Multiple gratings simultaneously formed in holographic polymer-dispersed liquid-crystal displays. Applied Physics Letters, **76**, 523/1–523/3 (2000). DOI: 10.1063/1.125836

[25] Fernández E., Ortuño M., Gallego S., García C., Beléndez A., Pascual I.: Comparison of peristrophic multiplexing and a combination of angular and peristrophic holographic multiplexing in a thick PVA/acrylamide photopolymer for data storage. Applied Optics, **46**, 5368–5373 (2007). DOI: 10.1364/AO.46.005368

eXPRESS Polymer Letters Vol.5, No.1 (2011) 82–91
Available online at www.expresspolymlett.com
DOI: 10.3144/expresspolymlett.2011.9

Fracture behavior of quenched poly(lactic acid)

J. Gámez-Pérez[*1], *J. C. Velazquez-Infante*[1], *E. Franco-Urquiza*[1], *P. Pages*[2], *F. Carrasco*[3], *O. O. Santana*[1], *M. Ll. Maspoch*[1]

[1]Centre Català del Plàstic (CCP), Universitat Politècnica de Catalunya C/Colon 114, 08222 Terrassa, Spain
[2]Materials Science Departament – ETSEIAT, Universitat Politecnica de Catalunya C/Colon 11, 08222 Terrassa, Spain
[3]Department of Chemical Engineering, Universitat de Girona, Campus de Montilivi, s/n. 17071 Girona, Spain

Received 1 July 2010; accepted in revised form 29 September 2010

Abstract. The effect of a quenching treatment applied on heated cast sheet extruded films of two poly(lactic acid) (PLA) commercial grades, with different optical purities, was studied. The thermal and mechanical properties of the films, as well as their fracture behavior, were assessed by differential scanning calorimetry (DSC), tensile tests, and the essential work of fracture (EWF) approach. The heating-quenching treatment causes a de-aging effect with an increase in the free volume of polymer chains evidenced by a decrease in the glass transition temperature (T_g) and a decrease in the tensile stiffness and yield stress. As a result, there is an abrupt increase in ductility, finding a dramatic change in the fracture behavior, from brittle to ductile. The use of digital image correlation (DIC) of the strain field analysis during fracture testing has allowed relating the decrease on the yield stress promoted by quenching with the crack propagation kinetics. The use of the EWF method to characterize the fracture toughness of PLA has allowed to measure this enhancement on toughness, finding that the specific essential work of fracture (w_e) and the plastic term (βw_p) parameters increased 120% and 1200%, respectively, after the quenching process.

Keywords: *mechanical properties, poly(lactic acid) PLA, essential work of fracture (EWF), physical aging*

1. Introduction

Poly(lactic acid) (PLA) is a semi-crystalline biodegradable polymer that has been used for several years in medical and biocompatible applications [1]. The commercial PLA is synthesized from lactic acid, which comes from renewable sources and at the present is the biopolymer with the fastest consumption growth rate [2], finding an increasing interest in the development of novel applications for other industrial sectors, such as houseware, packaging, etc. The lactic acid used to produce commercial PLA is in fact a stereo isomer, where the L-lactic acid monomer is the main component and the D-lactic acid stereoisomer is present as impurity, affecting the ability to crystallize and the final properties of PLA [3].

The glass transition (T_g) and melting (T_m) temperatures of PLA are around 60 and 155°C, respectively. However, its rate of crystallization from the melt is quite slow if compared with the cooling rates found in typical industrial transformation processes [4, 5]. As a consequence, commercial PLA products are mainly found in the glassy state, and thus can experience physical aging [6]. With aging, a molecular reorganization process, which originates the presence of ordered domains or more organized zones, is produced. This reordering is known also as densification and causes a considerable decrease in the free volume (v_f). The molecular mobility and the entanglement density are determined by the v_f, which in turn limits the ability of the material to store and dissipate energy when it is

*Corresponding author, e-mail: jose.gamez@upc.edu

mechanically stressed. This aging phenomenon occurs in a broad temperature range between T_g and the first (highest) secondary transition, T_β [7] and can induce a decrease in ductility and increase in stiffness.

The effects originated by the physical aging of the PLA have been the object of study during the last few years [8–11]. The mechanical behavior is one of the research areas studied, and it was found that the mechanical properties varied with aging time. The modulus and yield stress presented a similar step growing trend until they reached a plateau after 1000 h of aging. Strain at break, meanwhile, presented a rapid decrease from 300 to 6% at room temperature in 24 h, remaining practically constant thereafter [11]. Therefore, the brittleness of PLA at room temperature can be viewed as a consequence of the physical aging process. Nevertheless, in spite of these advances, studies describing the effect of aging on the structure-properties relationship of the fracture behavior of PLA are not yet known.

As physical aging does not involve permanent changes in the material structure, it can be regarded as a reversible process. The inverse process, hereafter called de-aging, can be caused by a thermal treatment at T_g (or a slightly higher temperature) followed by quenching. Heating at that temperature increases the molecular mobility of the polymeric chains and eliminates the pseudo-ordered or more organized domains generated during aging. Accordingly, such treatment also generates an increase in the v_f, resulting in a looser packing structure, similar to that above T_g. The sudden cooling freezes this less ordered structural state and hampers a chain reorganization such as the one caused by aging during slow cooling. Even though physical aging on toughness behaviour of polymers has been little investigated using fracture mechanics approaches, the essential work of fracture method (EWF) has been reported as a successful technique to follow the effect of physical aging on polymer films [12–16].

The aim of this work consists in the application of a de-aging thermal treatment to two commercial grades of PLA with different D-lactic monomer fractions and studying their fracture behavior applying the EWF method.

2. Experimental part

2.1. Materials and processing

In this study, two commercial grades of PLA from NatureWorks® (2002D and 4032D) were used. These grades have different D-lactic monomer contents, 4.25 and 2% respectively [17–20], and weight average molecular weights, 212 and 207 kDa respectively, assessed by Gel Permeation Chromatography (GPC) [21]. Sheets with both materials were obtained by cast sheet extrusion in a single-screw COLLIN Teach-Line® E16T extruder (T = 145–200°C, 50 rpm). Before processing, the materials were dried in a PIOVAN dehumidifier (T = 80°C, t = 3 h) to prevent hydrolysis. The chill rolls temperature was set to 50°C.

All test specimens were cut along the film production (MD) direction. De-aging of the sheets was performed in an oven at 60°C for 20 min., followed by quenching in an iced water bath. In order to maintain the form of the sheets, they were placed between two steel plates during heating and quenching. All tests were carried out immediately after the de-aging treatment. For comparison purposes, samples that had not been thermally treated were also tested. The nomenclature employed was PLA-X and PLA-XT for extruded and thermally treated films respectively, where X is set as 96 for PLA with 95.75% L-lactic monomer and 98 for PLA with 98% L-lactic monomer, and T represents the thermal treatment of de-aging followed by quenching.

2.2. Thermal characterization

Differential scanning calorimetry (DSC) data from samples were obtained in a Perkin Elmer calorimeter, model Pyris 1 (with 2P intracooler). Temperature and enthalpy calibration was performed using indium and lead. Samples of approximately 10 mg taken from the central sections of test specimens were sealed in aluminium pans and subjected to heating from 30 to 200°C at 10°C/min. under a dry nitrogen atmosphere. From thermograms, the midpoint glass transition temperature (T_g), melting temperature (T_m), cold crystallization enthalpies (ΔH_{cc}), and melting enthalpy (ΔH_m) were recorded following ISO 11357-3:1999 and ISO 11357-2:1999 standards.

2.3. Mechanical and fracture characterization

The mechanical characterization was performed by means of tensile tests according to the ASTM D-638 standard. Tests were carried out in a universal testing machine Galdabini Sun 2500 (Italy), equipped with a 5 kN load cell. A standard specimen's geometry type IV was used. Deformations were followed with a video extensometer, a Mintron OS-65D CCD (Taipei, Taiwan) video camera in conjunction with Messphysik (Fürstenfeld, Austria) Windows based software. Yield stress (σ_y), Young's modulus (E), and strain at break (ε_b) were assessed. Each value is the average of five valid tests.

The fracture behavior of materials that present high plastic deformation can be described by post-yielding fracture mechanics (PYFM). The Essential Work of Fracture method (EWF) provides a technique for obtaining toughness parameters for the ductile fracture process in either tensile [22–24] or tearing [25] configurations. Deeply Double Edge Notched Tensile (DDENT) specimens are the most used geometry in EWF determinations in tensile mode. However, for the correct application of the EWF method, some experimental constraints must be taken into account. The ligament length should be in a range that guarantees: (1) pure plane stress conditions, (2) no border effect, (3) full yielding of the ligament length prior to crack propagation, and (4) a geometrical similarity between the load vs. displacement (*F-d*) curves of specimens with different ligament lengths [22].

The EWF concept states that the energy involved during a ductile fracture (W_f) can be partitioned into two components. One component, the essential work (W_e) is associated with the energy spent in the inner fracture process zones (FPZ) and is therefore proportional to the fracture area ($\ell \cdot t$), where ℓ is the ligament length and t is the specimen width. The second component is the non-essential work of fracture or plastic work (W_p), which is related to the energy of the process that takes place in the outer plastic deformation zone, called also the plastic zone (OPZ). As it is related to plastic deformation and other dissipative processes, W_p is proportional to the volume of the deformed region ($\ell^2 \cdot t$) surrounding the crack process zone. The relation between W_f, W_e, and W_p can be expressed by Equation (1):

$$W_f = W_e + W_p = w_e \ell t + w_p \beta \ell^2 t \quad (1)$$

where β is a shape factor for the plastic zone. Expressing both members of Equation (1) in their specific terms results in a direct relationship between the specific fracture energy (w_f) and ℓ (Equation (2)):

$$w_f = w_e + \beta w_p \ell \quad (2)$$

According to Equation (2) the essential work of fracture (w_e) and the plastic term (βw_p) can be obtained from linear regression of a set of values represented in a diagram of specific fracture energy versus ligament length (w_f vs. ℓ). More information about the testing procedure and applicability of the EWF technique can be found in two recent reviews of the EWF method [26, 27].

The specimens used in this work are rectangular DDENT with nominal dimensions of 60×30×0.30 mm^3. Five ligament lengths between 5 and 25 mm with a step of 5 mm were tested. For each ligament length, three specimens were investigated. Deformation was followed with a video-extensometer following the procedure described in a previous work [28]. The crosshead speed for mechanical and fracture characterization was 1 mm/min and tests were conducted at room temperature (22±1°C).

2.4. Strain field analysis

In order to validate the applicability of the EWF method to the four materials studied, DDENT samples with three different ligament lengths were tested. A commercially available optical strain measurement system (ARAMIS®, which is a trade name of the equipment from GOM GmbH, Braunschweig, Germany) that utilizes two digital cameras and the digital image correlation (DIC) methodology was used to asses the strain distribution with respect to both time and space in the three axes. Therefore, point to point sample thickness variation during testing can be recorded and analyzed.

3. Results and discussion

3.1. Thermal characterization

DSC first heating curves for PLA samples are shown in Figure 1. In the curves corresponding to samples without thermal treatment, it can be observed an endothermic peak around 63°C, right after the mid-point glass transition temperature, shown in Table 1. This is a typical signal shown by physically aged glassy polymers. The area under

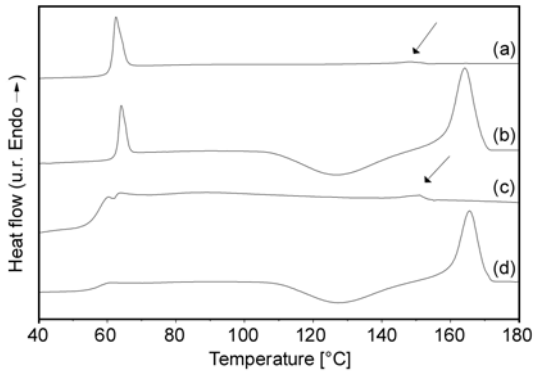

Figure 1. First heating DSC curves of PLA-96 (a), PLA-98 (b), PLA-96T (c), and PLA-98T (d)

Table 1. Effect of the de-aging treatment on the thermal properties of PLA-96 and PLA-98

Thermal properties	PLA-96	PLA-96T	PLA-98	PLA-98T
T_g [°C]	60.1±0.1	56.0±0.1	61.3±0.5	57.1±0.4
T_m [°C]	148.0±0.5	148.4±0.6	164.1±0.1	165.2±0.5
ΔH_{cc} [J/g]	–	–	29.2±1.4	30.7±0.4
ΔH_m [J/g]	0.80±0.01	1.3±0.3	31.2±0.4	33.5±0.2
X_c [%]	0.86±0.02	1.4±0.3	2.2±1.1	3.0±0.7

the endothermic peak at T_g corresponds to the excess enthalpy of relaxation (ΔH_{rel}) [29] and can be used as an indicator of aging [30, 31]. When glassy polymers are fast cooled, they are in a metastable state with an excess of enthalpy, entropy, and volume, which is far from the thermodynamic equilibrium. This excess in thermodynamic properties acts as driving force for a slow and gradual approach toward the thermodynamic equilibrium, originating a decrease in the free volume of the polymer. The change in v_f is accompanied by a simultaneous decrease in the segmental mobility. As a result, the aged PLA has less enthalpy and potential energy than the just cooled one. Therefore, when the material is reheated, more energy (ΔH_{rel}) is needed for the glass transition to take place. De-aged samples did not show the ΔH_{rel} endothermic peaks (Figures 1c and 1d), indicating that the state of aging was completely erased. Besides, an exothermic peak (cold crystallization) can only be appreciated in the PLA-98 samples (Figures 1b and 1d). PLA cold crystallization is affected by the rate of heating, the optical purity (L-lactic isomer content present in the material), and the previous thermal history experienced by the material [32–34]. In this case, the lower L-lactic content of both PLA-96 samples reduces its crystallization rate. Consequently, PLA-96 samples need a greater time for cold crystallization than that used in the experimental conditions.

In Figure 1, endothermic peaks corresponding to the fusion of PLA crystallites can be identified at around 148°C in the case of PLA-96 samples and at around 165°C for PLA-98 ones. PLA-98 samples showed a stronger fusion signal than the PLA-96 ones did (identified with an arrow in Figure 1) due to a greater crystal population, originated by cold crystallization during heating.

Crystallinity (X_c) was determined from the measured ΔH_{cc} and ΔH_m based on the Equation (3) [4]:

$$X_c = \frac{\Delta H_m - \Delta H_{cc}}{\Delta H_0} \cdot 100 \quad (3)$$

where ΔH_0 corresponds to the enthalpy of fusion of the theoretical 100% crystalline PLA. In this study ΔH_0 was take as 93 J/g [35]. All calculations were made based on data obtained from the first heating. Table 1 summarizes the values of X_c, T_g, and T_m determined from first heating thermograms of all materials.

It was found that samples without thermal treatment of both PLAs showed the glass transition at higher temperature values. Aging reduces segmental mobility, making it necessary to heat the samples up to higher temperature values to allow the glass transition to occur, resulting in the higher T_g values observed. Besides, it was also found that PLA-98 samples had higher values of T_m. The melting point of a semicrystalline polymer is determined by the size and perfection of its crystals (i.e. by the lamellar thickness). Higher optical purity gives more structural regularity to PLA-98 samples, and therefore it can form crystals of higher lamellar thickness during the cold crystallization that takes place at the first heating scan. The low X_c values indicate that in all cases the sheets are essentially amorphous. Moreover, there is no evidence that the crystallinity or the cold crystallization ability were affected by the de-aging thermal treatment.

3.2. Mechanical characterization

Stress-strain curves for samples with and without de-aging thermal treatment are shown in Figure 2. The original sheets which had not been de-aged are stiffer, with higher yield stress and lower elongation at break, than the de-aged ones. Post-mortem test samples of PLA-98 and PLA-98T, shown in

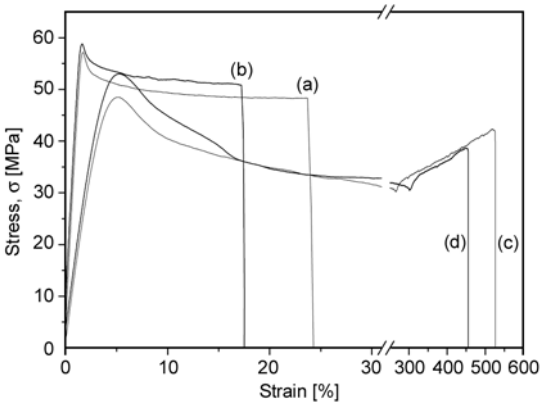

Figure 2. Stress-strain diagrams of (a) PLA-96, (b) PLA-98, (c) PLA-96T, and (d) PLA-98T

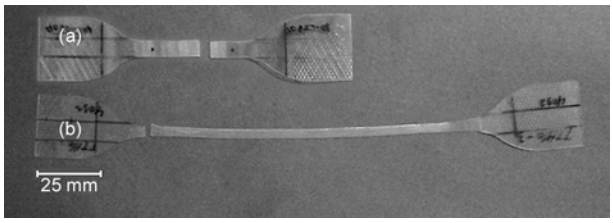

Figure 3. Post-mortem tensile test samples: (a) not thermally treated (PLA-98), and (b) with thermal treatment (PLA-98T)

Figure 3, clearly evidence the differences seen in the strain–stress curves. Samples without thermal treatment showed yielding without necking and presence of crazes (Figure 3a), while a more ductile behavior, characterized by localized shear yielding and neck formation, was shown by the de-aged ones (Figure 3b). PLA-96 and PLA-96T showed behaviors similar to those seen for PLA-98 and PLA-98T respectively. As explained, aging causes a molecular reorganization with reduction of free volume, resulting in a more packed structure with lower potential energy. Since molecules attract one to another, the decrease of free volume is accompanied by decrease in potential energy of the polymer. Consequently, the stress required for establishing yielding during tensile testing, which is related to the variation of potential energy, will be greater in samples with lower potential energy in the ground state or vice versa. On the other hand, the increase in the free volume of the polymer chains caused by the de-aging treatment and the displacement of the glass transition to lower values of temperatures result in a greater mobility of the polymer chains, permitting more local strain to be achieved. These observations are in agreement with results obtained by Pan *et al*. [11].

Table 2. Tensile parameters of PLA-96 and PLA-98 before and after the quenching treatment

Mechanical properties	PLA-96	PLA-96T	PLA-98	PLA-98T
σ_y [MPa]	56.2±0.7	47.3±1.1	58.4±0.5	53.4±0.6
E [GPa]	4.0±0.2	3.3±0.2	4.3±0.1	3.5±0.3
ε_b [%]	24±5	456±100	17±4	422±50

Table 2 summarizes the average values obtained from the mechanical test assessed for all materials under study. From that data, it can be said that, on the whole, samples of PLA-98 have slightly higher values of modulus and yield stress but lower elongation at break than their PLA-96 counterpart samples. When comparing the mechanical properties of both PLA grades in depth, it can be found that only in the case of the thermally treated specimens, differences in E and σ_y are pronounced. It is well known that the deformation mechanisms involved in amorphous polymer systems below their T_g are controlled by the molecular entanglements density and the chain stiffness or characteristic ratio (C_∞). Joziasse *et al*. [36] found in a previous work that there is an inverse relationship between C_∞ and the D-lactic isomer content present in PLA copolymers. Therefore, the chain stiffness increases with stereoregularity. In the case of de-aged specimens, the polymer chains present higher mobility, free volume and a less packed structure than the non thermally treated ones. The higher D-lactic isomer content of PLA-96T makes the polymer chains to be more flexible than those of PLA-98T, resulting in lower elastic modulus and yield stress. Regarding the influence of de-aging and quenching, it can be pointed out that PLA-96 and PLA-98 are influenced by the intermolecular interactions resulting from the densification produced during aging, which result in higher stiffness and yield stress. Such increase in the mechanical properties caused by aging hinders the effect of the chain stiffness when comparing both PLA grades, attributing the slightly higher values of modulus and yield stress of the PLA-98 to the small variations in crystallinity [37].

3.3. Fracture behavior

3.3.1. Strain field analysis

As pointed out in the experimental section, in order to validate the applicability of the EWF method, the strain distributions in the OPZ and FPZ from samples with different ligament lengths were deter-

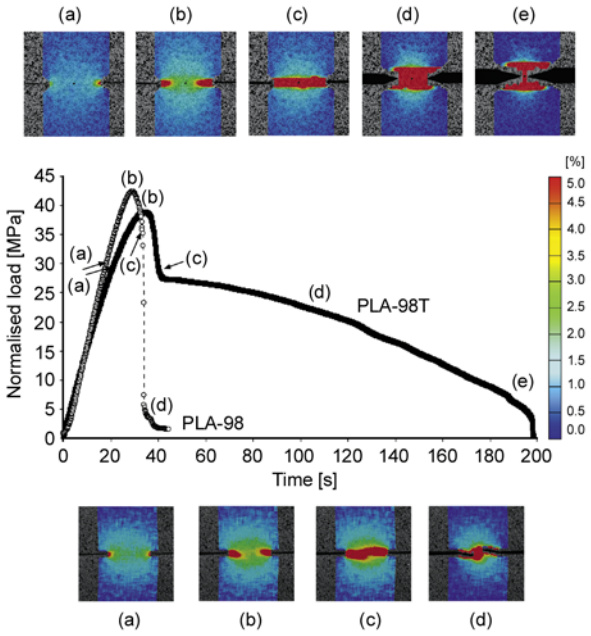

Figure 4. Time-resolved strain field analysis showing the crack growth and thickness variation for DDENT samples of PLA-98 and PLA-98T with ℓ = 10 mm. The normalised load reported on the *y*-axis has been calculated as the testing load divided by the initial ligament section.

mined using digital image correlation (DIC) methodology. As an example, load-time curves of PLA-98 and PLA-98T samples with ℓ~10 mm are shown in Figure 4. In this figure, the plastic and elastic deformations near the crack tip are evidenced, showing the evolution of the thickness reduction of the specimens during the crack growth. Similar load-time curves for PLA-96 and PLA-96T, respectively, were also found.

By observing the deformation map surrounding the notch ligament in time, the onset of crack propagation can be established with DIC data. As an example, point (c) of Figure 4 was determined as the onset of crack propagation. Following such analysis, it can be proved that the ligament yielded before the onset of crack initiation for de-aged materials (PLA-96T and PLA 98-T), demonstrating the applicability of the EWF concept to these films. Furthermore, the curves in Figure 4 show the development of a yielding area ahead of the crack tips simultaneously in both sides of the DDENT specimen, thus validating the uniformity of the notch sharpening procedure.

When comparing both curves in Figure 4, the differences in the crack propagation kinetics after point (c) can be appreciated, leading to a change

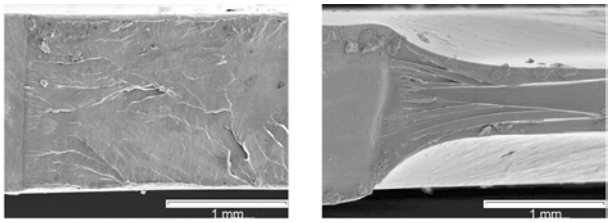

Figure 5. SEM microphotographs corresponding to notch zones of PLA-98 (a) and PLA-98T (b) of post-mortem DDENT specimens (ℓ = 10 mm)

form brittle to tough fracture behavior promoted only by the de-aging treatment. Similar results were found in the cases of PLA-96 and PLA-96T.

As seen in Figure 4, the maximum normalized load reached in the case of PLA-98 is higher than in the case of PLA-98T, along with a decrease in the time at which this point is reached. At this point (b), a deformation halo that corresponds to elastic deformations (lower than 3%) can be observed. As PLA-98T has more free volume, it can undergo the yield phenomenon at a lower stress level than PLA-98, partially absorbing the elastic energy as plastic deformation and stable crack growth. In PLA-98 samples, on the other hand, the fast elastic energy recovering process results in unstable crack growth, resulting in a premature brittle failure.

The thickness variations assessed by DIC data were corroborated with scanning electron microscopy (SEM) of post-mortem specimens. In Figure 5 are shown, as an example, SEM microphotographs from PLA-98 and PLA-98-T, where a thickness reduction around 5% and 60% respectively can be observed.

3.3.2. Essential work of fracture

The EWF methodology was applied to all samples under study. Figure 6 shows an example of load-displacement (*F*-*d*) curves obtained for PLA-96 and PLA-96T. From these curves, the criterion of self-similarity can be corroborated, as in case of the thermally treated materials (Figure 6b). In the case of then non thermally treated specimens, curves show a common behavior in the 10–25 mm range of ligament lengths (Figure 6a). Such likenesses are reflected in a similar initial slope of the curves, up to the maximum load, and parallel tails after the onset of crack propagation. Due to the fast crack growth of these specimens, some tearing at the end of the specimen fracture can introduce some remark-

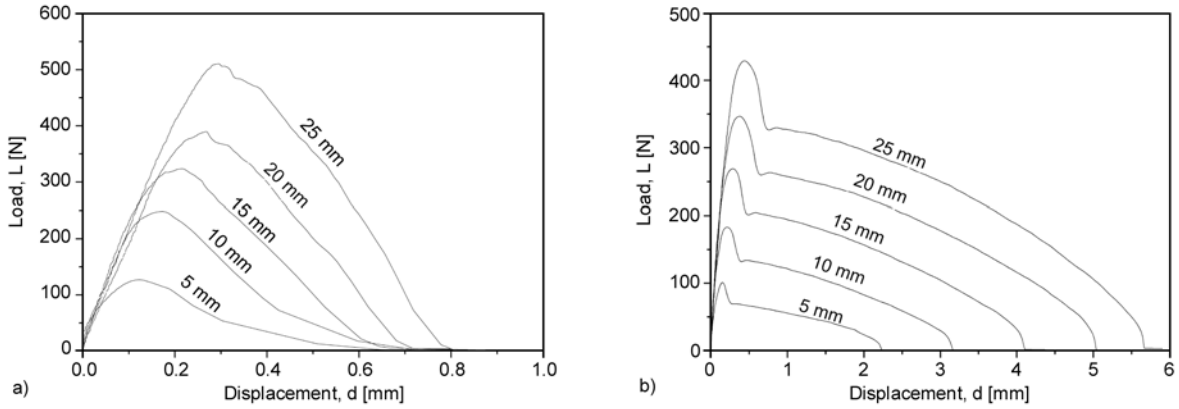

Figure 6. Load-displacement diagrams as a function of the ligament length (ℓ) of PLA-96 (a) and PLA-96T (b)

able discontinuities in the *L-d* curves, especially visible in the lower ligament lengths, as a gentle load drop in the final stages of the specimen rupture.

From tests it was determined that requisites for applying the EWF method were only clearly fulfilled in de-aged materials. Materials without thermal treatment (PLA-96 and PLA-98), did not fully satisfy the EWF requisites of stable crack growth, even though showing a similar fracture geometry. Nevertheless, as observed in the diagrams of w_f versus ℓ. Shown in Figure 7, the non thermally treated PLA exhibited a linear relationship between w_f and ℓ, permitting the determination of the fracture parameters. These parameters, since the specimens did not fulfill all the prerequisites considered in the EWF theory, can not be used for performing exact quantitative comparisons, but qualitative ones. The regression coefficients, in the range of 0.7 and 0.8, confirm a good linear relationship between w_f and ℓ, allowing the use of the calculated w_e and βw_p parameters, to reasonably analyze the influence of the thermal treatment on the fracture behavior of the PLA films.

From comparison of these data with the fracture parameters calculated for thermally treated materials, changes caused by the de-aging treatment in the toughness of PLA can be determined. Table 3 summarizes the fracture data for all samples.

It is evident from data summarized in Table 3 that the thermal treatment caused a drastic change in the fracture parameters of the two PLA used, evidenced by the noticeable increment in w_e of 120% and in βw_p of 1200–1300%. When comparing the different PLA grades, it can be seen that samples without thermal treatment (PLA-96 and PLA-98) have similar w_e values, which are higher than the G_{IC} value estimated by the application of the linear elastic

Table 3. Assessment of the specific essential work of fracture (w_e) and plastic term (βw_p) of all materials

Fracture parameters	PLA-96	PLA-96T	PLA-98	PLA-98T
w_e [kJ/m^2]	15.9±0.8	34.1±1.7	16.4±0.8	37.9±1.5
βw_p [MJ/m^3]	0.29±0.04	4.4±0.1	0.28±0.04	3.7±0.1

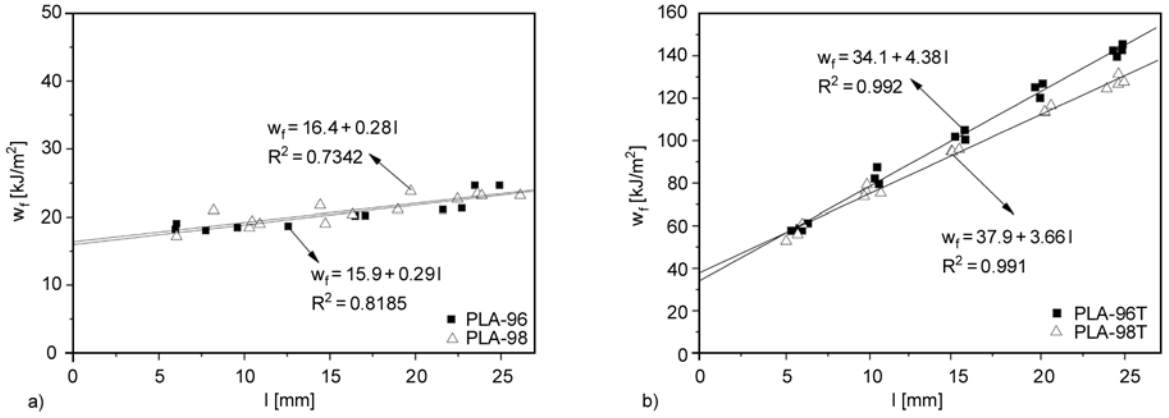

Figure 7. Specific work of fracture as a function of the ligament length for non-treated materials (a) and de-aged materials (b)

fracture mechanics (LEFM). In the case of 6.3 mm thick injection molded samples of PLA-96, G_{IC} was estimated by our group to be 2.4 kJ/m^2 [38] and 6.5 kJ/m^2 by Park *et al*. on 5 mm thick hot-press plates, using a PLA with 98% L-lactic isomer content [39]. The differences observed between those values can be attributed to the different state of tension (plane stress in the case of the films and plain strain for the thicker specimens), which entails a reduction on the fracture toughness [40].

In the case of de-aged materials, it was found that PLA-98T presents a slightly greater w_e value than PLA-96T. According to Mai and colleagues [41], since w_e involves the plastic deformation processes of necking the ligament section (FPZ) and the work needed for the cracks to start growing, consequently, w_e will be greater the higher the σ_y and the higher the strain at necking (ε_y), as was the case for PLA-98T compared to PLA-96T in tensile testing (Table 2). Following the same reasoning, the stress versus strain curves in Figure 2 show that the areas under the σ-ε curves, limited by the yielding point, for the de-aged materials are greater than those for their corresponding non-treated samples, justifying the greater values observed for w_e.

With respect to βw_p, the values obtained for de-aged materials are much higher than corresponding ones for the non-treated ones (Table 3). Such differences can be related to the plastic deformation developed around the ligament net section, which can be observed in post-mortem DDENT specimens (Figure 5).

When both de-aged grades are compared, it can be seen that the highest βw_p values corresponded to PLA-96T. Arkhireyeva and colleagues found that βw_p increases with increasing ductility and decreases with increasing σ_y [42]. The mechanical tests performed are consistent with Arkhireyeva's work, since PLA-96T presented higher ε_b but lower σ_y (Table 2).

From these results it can be foreseen that a thermal treatment applied to PLA could favor its toughness resistance for a certain period of time. This treatment could be used prior to some machining operations, such as punching or drilling, to avoid a premature brittle failure.

4. Conclusions

The heating at temperatures close to T_g and subsequent quenching treatment produces a de-aging effect, with an increase of the free volume of polymeric chains, evidenced by the displacement of the glass transition to lower temperatures and the increase in the system potential energy (disappearance of the endothermic peak at T_g).

As a consequence, quenching promotes a brittle-to-ductile change in the fracture behavior of PLA, regardless of the D-lactic isomer content, with a decrease on the tensile strength, appearance of shear yielding and a localized and neck formation. The fracture parameters, assessed by the EWF method, show a great enhancement of the toughness after the de-aging and quenching treatment.

Regarding the influence of the D-lactic isomer content in PLA films, when they are in a glassy aged state there are no remarkable differences in the mechanical properties and fracture behavior. Only when the films are in a de-aged form, the differences in the chain stiffness of both PLA grades are revealed: the higher the optical purity, the higher the elastic modulus and tensile strength but lower deformation at break. Also, w_e increases with increasing optical purity, but the plastic term (βw_p) decreases.

Acknowledgements

The authors wish to thank the Spanish Science and Education Ministry for financial support through the projects MAT 2007-62450 and MAT 2010-19721. J. Velazquez is grateful to AECID for the concession of a pre-doctoral grant.

References

[1] Griffith L. G.: Polymeric biomaterials. Acta Materialia, **48**, 263–277 (2000). DOI: 10.1016/S1359-6454(99)00299-2

[2] Lim L-T., Auras R., Rubino M.: Processing technologies for poly(lactic acid). Progress in Polymer Science, **33**, 820–852 (2008). DOI: 10.1016/j.progpolymsci.2008.05.004

[3] Sarasua J. R., Arraiza A. L., Balerdi P., Maiza I.: Crystallinity and mechanical properties of optically pure polylactides and their blends. Polymer Engineering and Science, **45**, 745–753 (2005). DOI: 10.1002/pen.20331

[4] Auras R., Harte B., Selke S.: An overview of polylactides as packaging materials. Macromolecular Bioscience, **4**, 835–864 (2004).
DOI: 10.1002/mabi.200400043

[5] Miyata T., Masuko T.: Crystallization behaviour of poly(L-lactide). Polymer, **39**, 5515–5521 (1998).
DOI: 10.1016/S0032-3861(97)10203-8

[6] Hutchinson J. M.: Physical aging of polymers. Progress in Polymer Science, **20**, 703–760 (1995).
DOI: 10.1016/0079-6700(94)00001-I

[7] Strum L. C. E.: Physical aging in plastics and other glassy materials. Polymer Engineering and Science, **17**, 165–173 (1977).
DOI: 10.1002/pen.760170305

[8] Pluta M., Murariu M., Alexandre M., Galeski A., Dubois P.: Polylactide compositions. The influence of ageing on the structure, thermal and viscoelastic properties of PLA/calcium sulfate composites. Polymer Degradation and Stability, **93**, 925–931 (2008).
DOI: 10.1016/j.polymdegradstab.2008.02.001

[9] Acioli-Moura R., Sun X. S.: Thermal degradation and physical aging of poly(lactic acid) and its blends with starch. Polymer Engineering and Science, **48**, 829–836 (2008).
DOI: 10.1002/pen.21019

[10] Aou K., Hsu S. L., Kleiner L. W., Tang F-W.: Roles of conformational and configurational defects on the physical aging of amorphous poly(lactic acid). Journal of Physical Chemistry B, **111**, 12322–12327 (2007).
DOI: 10.1021/jp074509t

[11] Pan P. J., Zhu B., Inoue Y.: Enthalpy relaxation and embrittlement of poly(L-lactide) during physical aging. Macromolecules, **40**, 9664–9671 (2007).
DOI: 10.1021/ma071737c

[12] Liu C-H., Nairn J. A.: Using the essential work of fracture method for studying physical aging in thin, ductile, polymeric films. Polymer Engineering and Science, **38**, 186–193 (1998).
DOI: 10.1002/pen.10179

[13] Karger-Kocsis J., Bárány T., Moskala E. J.: Plane stress fracture toughness of physically aged plasticized PETG as assessed by the essential work of fracture (EWF) method. Polymer, **44**, 5691–5699 (2003).
DOI: 10.1016/S0032-3861(03)00590-1

[14] Ho C. H., Vu-Khanh T.: Physical aging and time–temperature behavior concerning fracture performance of polycarbonate. Theoretical and Applied Fracture Mechanics, **41**, 103–114 (2004).
DOI: 10.1016/j.tafmec.2003.11.008

[15] Bárány T., Ronkay F., Karger-Kocsis J., Czigány T.: In-plane and out-of-plane fracture toughness of physically aged polyesters as assessed by the essential work of fracture (EWF) method. International Journal of Fracture, **135**, 251–265 (2005).
DOI: 10.1007/s10704-005-3947-2

[16] Bárány T., Földes E., Czigány T.: Effect of thermal and hygrothermal aging on the plane stress fracture toughness of poly(ethylene terephthalate) sheets. Express Polymer Letters, **1**, 180–187 (2007).
DOI: 10.3144/expresspolymlett.2007.28

[17] NatureWorks® PLA Polymer 2002D – Data Sheet (2005).

[18] NatureWorks® PLA Polymer 4032D – Data Sheet (2006).

[19] Li H., Huneault M. A.: Effect of nucleation and plasticization on the crystallization of poly(lactic acid). Polymer, **48**, 6855–6866 (2007).
DOI: 10.1016/j.polymer.2007.09.020

[20] Xiao H. W., Lu W., Yeh J-T.: Effect of plasticizer on the crystallization behavior of poly(lactic acid). Journal of Applied Polymer Science, **113**, 112–121 (2009).
DOI: 10.1002/app.29955

[21] Carrasco F., Pagès P., Gámez-Pérez J., Santana O. O., Maspoch M. L.: Processing of poly(lactic acid): Characterization of chemical structure, thermal stability and mechanical properties. Polymer Degradation and Stability, **95**, 116–125 (2010).
DOI: 10.1016/j.polymdegradstab.2009.11.045

[22] Clutton E.: Essential work of fracture. in 'Fracture mechanics testing methods for polymers, adhesives and composites' (eds.: Moore D. R., Williams J. G., Pavan A.) Vol 28, 177–195 (2001).
DOI: 10.1016/S1566-1369(01)80033-9

[23] Ganß M., Satapathy B. K., Thunga M., Weidisch R., Pötschke P., Jehnichen D.: Structural interpretations of deformation and fracture behavior of polypropylene/multi-walled carbon nanotube composites. Acta Materialia, **56**, 2247–2261 (2008).
DOI: 10.1016/j.actamat.2008.01.010

[24] Gámez-Pérez J., Muñoz P., Velasco J. I., Martínez A. B., Maspoch M. L.: Determination of essential work of fracture in EPBC sheets obtained by different transformation processes. Journal of Material Science, **40**, 1967–1974 (2005).
DOI: 10.1007/s10853-005-1218-2

[25] Wong J. S. S., Ferrer-Balas D., Li R. K. Y., Mai Y-W., Maspoch M. L., Sue H-J.: On tearing of ductile polymer films using the essential work of fracture (EWF) method. Acta Materialia, **51**, 4929–4938 (2003).
DOI: 10.1016/S1359-6454(03)00335-5

[26] Martínez A. B., Gámez-Pérez J., Sanchez-Soto M., Velasco J. I., Santana O. O., Maspoch M. L.: The essential work of fracture (EWF) method – Analyzing the post-yielding fracture mechanics of polymers. Engineering Failure Analysis, **16**, 2604–2617 (2009).
DOI: 10.1016/j.engfailanal.2009.04.027

[27] Bárány T., Czigány T., Karger-Kocsis J.: Application of the essential work of fracture (EWF) concept for polymers, related blends and composites: A review. Progress in Polymer Science, **35**, 1257–1287 (2010).
DOI: 10.1016/j.progpolymsci.2010.07.001

[28] Gámez-Pérez J., Santana O., Martinez A. B., Maspoch M. L.: Use of extensometers on essential work of fracture (EWF) tests. Polymer Testing, **27**, 491–497 (2008). DOI: 10.1016/j.polymertesting.2008.02.002

[29] Mo X. Q., Sun X. Z.: Effects of storage time on properties of soybean protein-based plastics. Journal of Polymers and the Environment, **11**, 15–22 (2003). DOI: 10.1023/A:1023831411521

[30] Aref-Azar A., Hay J. N.: Physical ageing in glassy polymers. An i.r. spectroscopic investigation of poly (ethylene terephthalate). Polymer, **23**, 1129–1132 (1982). DOI: 10.1016/0032-3861(82)90366-4

[31] Cowie J. M. G., Harris S., McEwen I. J.: Physical aging in poly(vinyl acetate). 2. Relative rates of volume and enthalpy relaxation. Macromolecules, **31**, 2611–2615 (1998). DOI: 10.1021/ma970287t

[32] Kolstad J. J.: Crystallization kinetics of poly(L-lactide-*co*-*meso*-lactide). Journal of Applied Polymer Science, **62**, 1079–1091 (1996). DOI: 10.1002/(SICI)1097-4628(19961114)62:7<1079::AID-APP14>3.0.CO;2-1

[33] Hernández Sánchez F., Molina Mateo J., Romero Colomer F. J., Salmerón Sánchez M., Gómez Ribelles J. L., Mano J. F.: Influence of low-temperature nucleation on the crystallization process of poly(L-lactide). Biomacromolecules, **6**, 3283–3290 (2005). DOI: 10.1021/bm050323t

[34] Salmerón Sánchez M., Gómez Ribelles J. L., Hernández Sánchez F., Mano J. F.: On the kinetics of melting and crystallization of poly(L-lactic acid) by TMDSC. Thermochimica Acta, **430**, 201–210 (2005). DOI: 10.1016/j.tca.2005.01.066

[35] Fischer E. W., Sterzel H. J., Wegner G.: Investigation of structure of solution grown crystals of lactide copolymers by means of chemical-reactions. Colloid and Polymer Science, **251**, 980–990 (1973). DOI: 10.1007/BF01498927

[36] Joziasse C. A. P., Veenstra H., Grijpma D. W., Pennings A. J.: On the chain stiffness of poly(lactide)s. Macromolecular Chemistry and Physics, **197**, 2219–2229 (1996). DOI: 10.1002/macp.1996.021970713

[37] Perego G., Cella G. D., Bastioli C.: Effect of molecular weight and crystallinity on poly(lactic acid) mechanical properties. Journal of Applied Polymer Science, **59**, 37–43 (1996). DOI: 10.1002/(SICI)1097-4628(19960103)59:1<37::AID-APP6>3.0.CO;2-N

[38] Nascimento L., Gámez-Pérez J., Santana O. O., Velasco J. I., Maspoch M. L.: Effect of the recycling and annealing on the mechanical and fracture properties of poly(lactic acid). Journal of Polymers and the Environment, **18**, 654–660 (2010). DOI: 10.1007/s10924-010-0229-5

[39] Park S-D., Todo M., Arakawa K.: Effect of annealing on the fracture toughness of poly(lactic acid). Journal of Materials Science, **39**, 1113–1116 (2004). DOI: 10.1023/B:JMSC.0000012957.02434.1e

[40] Kinloch A. J., Young R. J.: Fracture behaviour of polymers. Applied Science, London (1983).

[41] Mai Y-W., Cotterell B., Horlyck R., Vigna G.: The essential work of plane-stress ductile fracture of linear polyethylenes. Polymer Engineering and Science, **27**, 804–809 (1987). DOI: 10.1002/pen.760271106

[42] Arkhireyeva A., Hashemi S.: Fracture behaviour of polyethylene naphthalate (PEN). Polymer, **43**, 289–300 (2002). DOI: 10.1016/S0032-3861(01)00623-1